Thesis_Plag 1.pdf

Delhi Technological University

Document Details

Submission ID

trn:oid:::27535:120900077

Submission Date

Nov 11, 2025, 12:09 PM GMT+5:30

Download Date

Nov 11, 2025, 12:15 PM GMT+5:30

File Name

Thesis_Plag 1.pdf

File Size

4.7 MB

92 Pages

24,919 Words

143,539 Characters

6%   Overall Similarity

The combined total of all matches, including overlapping sources, for each database.

Filtered from the Report

▸ Bibliography

▸ Quoted Text

▸ Cited Text

▸ Small Matches (less than 14 words)

Exclusions

▸ 4 Excluded Sources

Match Groups

🔴 **55** Not Cited or Quoted 6%
Matches with neither in-text citation nor quotation marks

🟠 **0**   Missing Quotations   0%
Matches that are still very similar to source material

🟡 **0**   Missing Citation   0%
Matches that have quotation marks, but no in-text citation

🟢 **0**   Cited and Quoted   0%
Matches with in-text citation present, but no quotation marks

Top Sources

3%   🌐 Internet sources

3%   📖 Publications

3%   👤 Submitted works (Student Papers)

Integrity Flags

0 Integrity Flags for Review

No suspicious text manipulations found.

Our system's algorithms look deeply at a document for any inconsistencies that would set it apart from a normal submission. If we notice something strange, we flag it for you to review.

A Flag is not necessarily an indicator of a problem. However, we'd recommend you focus your attention there for further review.

Match Groups

55 Not Cited or Quoted **6%**
Matches with neither in-text citation nor quotation marks

0 Missing Quotations **0%**
Matches that are still very similar to source material

0 Missing Citation **0%**
Matches that have quotation marks, but no in-text citation

0 Cited and Quoted **0%**
Matches with in-text citation present, but no quotation marks

Top Sources

3% 🌐 Internet sources

3% 📖 Publications

3% 👤 Submitted works (Student Papers)

Top Sources

The sources with the highest number of matches within the submission. Overlapping sources will not be displayed.

1	Submitted works	
Shri Jagdishprasad Jhabarmal Tibrewala University on 2014-03-22		**1%**

2	Publication	
Nikita Jain, Nitin K Puri. " A proposed device based on MoSe -ZnO heterojunction...		**<1%**

3	Internet	
www.webtoons.com		**<1%**

4	Internet	
dspace.dtu.ac.in:8080		**<1%**

5	Publication	
Nikita Jain, Nitin K. Puri. "Zinc oxide incorporated molybdenum diselenide nanos...		**<1%**

6	Publication	
Hemant Kumar Arora, Nikita Jain, Sunil Kumar, Nitin Puri. "Vertically aligned 2D ti...		**<1%**

7	Internet	
pubs.rsc.org		**<1%**

8	Internet	
ouci.dntb.gov.ua		**<1%**

9	Internet	
www.mdpi.com		**<1%**

10	Publication	
Hemant K. Arora, Jyoti Shah, R.K. Kotnala, A.S. Rao, Nitin K. Puri. "Strategically en...		**<1%**

11	Internet	
advancedmanufacturing.us		<1%

12	Internet	
mdpi-res.com		<1%

13	Publication	
Tongwei Yuan, Zhijun Li, Wenshuang Zhang, Zhenggang Xue, Xiaoqian Wang, Zhi...		<1%

14	Submitted works	
University College London on 2018-12-17		<1%

15	Submitted works	
University of Malaya on 2025-01-17		<1%

16	Submitted works	
Malaviya National Institute of Technology on 2014-01-27		<1%

17	Submitted works	
Birla Institute Of Technology & Science - Pilani on 2025-10-10		<1%

18	Publication	
Shuai Zhang, Peng Song, Yukun Zheng, Yongling Ding, Qi Wang. "MoO2/MoO3/M...		<1%

19	Submitted works	
University of South Africa on 2025-06-01		<1%

20	Internet	
discovery.ucl.ac.uk		<1%

21	Internet	
www.nature.com		<1%

22	Publication	
Ming Yang, Xianfa Zhang, Xiaoli Cheng, Yingming Xu, Shan Gao, Hui Zhao, Lihua ...		<1%

23	Internet	
mapyourtech.com		<1%

24	Internet	
www.researchgate.net		<1%

25	Publication

Tzong-Ming Wu, Shih-Hsiang Lin. "Characterization and electrical properties of po...   **<1%**

26	Internet

link.springer.com   **<1%**

27	Internet

theses.hal.science   **<1%**

28	Submitted works

CSU, San Jose State University on 2025-05-19   **<1%**

29	Submitted works

Higher Education Commission Pakistan on 2025-09-25   **<1%**

30	Submitted works

Phenikaa University on 2024-06-04   **<1%**

31	Submitted works

Universiti Sains Malaysia on 2017-01-31   **<1%**

32	Publication

Younan, Sabrina M.. "Transition Metal Confinement Effects on Catalysis in Two-Di...   **<1%**

33	Publication

Youngmin Byoun, Suyoung Park, Changhyun Jin, Young-Jun Song, Sun-Woo Choi. ...   **<1%**

34	Publication

Zhimin Yang, Dongzhi Zhang, Dongyue Wang. "Carbon monoxide gas sensing pro...   **<1%**

35	Internet

oicr-e4.org   **<1%**

CHAPTER 1

Introduction and Scientific Motivation

Chapter 1 gives an overview of the growing research interest in creating ethanol gas sensors that are capable of operating efficiently at room temperature and low power consumption. The chapter commences by emphasizing the necessity for ethanol sensors having high sensitivity, stability, and selectivity, coupled with the potential to sense ethanol at a wide range of concentrations under ambient conditions. It then goes through the various types of ethanol sensing technologies, with a special focus on chemiresistive sensors on account of their simplicity and potential performance. The study also highlights how advancements in nanotechnology and material science can significantly enhance sensor performance, highlighting the benefits of nanocomposites derived from two-dimensional (2D) materials and heterojunction architectures. Through the examination of recent trends and extant limitations in the discipline, the chapter outlines key gaps in research and delineates the aims of the current work, thus laying the groundwork for the remaining chapters of the thesis.

1.1   Need for Volatile Organic Compounds (VOCs) Sensing

Environmental pollution has become a significant worldwide problem, primarily contributed by fast industrialization and urban growth [1,2]. With ongoing economic and industrial development, the release of volatile organic compounds (VOCs) into the environment has also increased tremendously [3]. VOCs are low-boiling-point, high-vapor-pressure organic chemicals which can evaporate and disperse in the air with ease even at room temperature (RT) [4]. They are omnipresent and found in outdoor as well as indoor environments [5].

Each day, human processes like driving cars, use of paints, combustion of fuels, and even breathing emit VOCs into the air [6]. Moreover, a significant amount of VOC emissions comes from personal care products, cleaning products, and many consumer goods [6]. So, practically all everyday activities cause some amount of VOC emission. The indoor concentration of VOCs has been shown to be as much as ten times higher than that outdoors [7]. An estimated 50 to 300 different VOCs have also been reported to be found in indoor air in domestic, commercial, and institutional buildings like homes, offices, schools, and shopping centers [5].
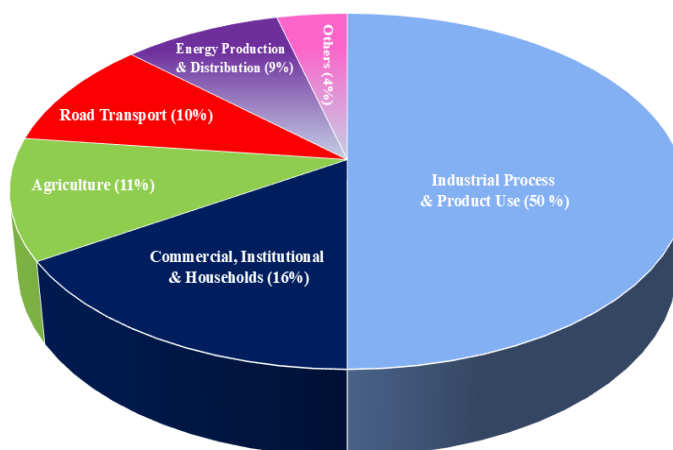
Fig. 1.1: Shows the major sources of VOCs and their percentage contribution to environmental pollution.

The most common volatile organic compounds (VOCs) are ethanol (C_2H_5OH), methanol (CH_3OH), acetone (CH_3COCH_3), formaldehyde (HCHO), benzene (C_6H_6), toluene (C_7H_8), acetylene (C_2H_2), and cyclohexane (C_6H_{10}), to mention but a few. Their

exposure is highly risky not just to human health and other forms of life but also to the environment in general [8, 9]. Some selected VOCs and their harmful effects and allowable exposure limits on human health are presented in Table 1.1 [10].

Table 1.1: lists the names, chemical formulas, health effects, and threshold values of VOCs.

VOC Name	Chemical Formula	Effect on Human Health	Threshold Value
Ethanol	C_2H_5OH	headaches, nausea, vomiting, kidney failure, inflammation of the nose and throat, harm to the central nervous system, and even cancer.	1000 ppm
Formaldehyde	HCHO	Chest tightness or pain, shortness of breath, or irritation of the eyes	0.75 ppm
Acetone	CH_3COCH_3	headache, exhaustion, dry mouth, nausea, and lightheadedness	750 ppm
Methanol	CH_3OH	Vertigo, headache, bronchial tightness, nausea, and narrowing of the airways	200 ppm
Benzene	C_6H_6	respiratory failure, convulsions, and narcotic effects	1 ppm
Toluene	C_7H_8	severe harm to the kidneys, liver, skin, and central nervous system	100 ppm
Cyclohexane	C_6H_{10}	irritation of the respiratory system, throat, and eyes	300 ppm
Acetylene	C_2H_2	headache, tachycardia, nausea, vomiting, dizziness, and exhaustion	N/A

Ethanol is one of the most used volatile organic compounds (VOCs), with widespread applications in the paint, cosmetic, agricultural, food, chemical, and pharmaceutical industries, as well as in alcoholic beverage production [11, 12]. But exposure to high levels of ethanol can significantly affect human health, causing symptoms of respiratory tract irritation, nausea, vomiting, headaches, renal impairment, and damage to the central nervous system; Chronic exposure can even result in carcinogenic effects [13, 14]. The World Health Organization (WHO) estimates that over three million deaths

per year are caused by excessive ethanol consumption and related health consequences [15].

Ethanol is also a very combustible chemical with an explosion range of 3.3% to 19%, which also poses severe safety hazards such as fire risk and road traffic accidents [16]. Additionally, vapors of ethanol can readily mix with other gases to create explosive mixtures and are considered one of the most dangerous and flammable VOCs [12]. Thus, preventing the potential health and environmental hazards posed by ethanol exposure is of the highest priority.

As ethanol leak cannot be efficiently sensed by human senses in a timely and precise way [1], it is important to create sensitive and reliable detection systems. Among them, ethanol gas sensors with high performance at room temperature (RT) are particularly desirable. These sensors possess various merits such as low power expenditure, easy preparation, potential miniaturization, durability over long periods, and reproducible sensing responses [17].

The increasing need for effective gas monitoring in the fields of air quality assessment, industrial safety, and environmental protection places an ever-increasing demand for reliable, low-power gas sensors [18,19]. Sensors targeted for widespread deployment need to be compact, highly selective, fast responding, and operable at room temperature with low energy consumption. Traditional gas sensors often require external power supplies or high operating temperatures, contributing to increased energy consumption, maintenance costs, and lowered operational stability, especially under hostile conditions [19]. Therefore, recent research has focused on developing room temperature gas sensors with improved sensitivity, selectivity, and long-term stability energy-efficient and practical solution for real-world monitoring applications [20-21].

1.2   Classification of Sensors

The contact between the ethanol molecules and the sensing layer of an ethanol sensor can cause measurable changes in its physical or electrical properties-such as resistance, capacitance, temperature, mass, or pressure. These changes are then transduced into quantifiable electrical signals. Depending upon the transduction mechanism involved,

sensors are broadly classified as electrical, optical, gravimetric, and thermal sensors [22–24]. A schematic diagram of different types of sensors and their subdivisions is illustrated in Fig. 1.2.
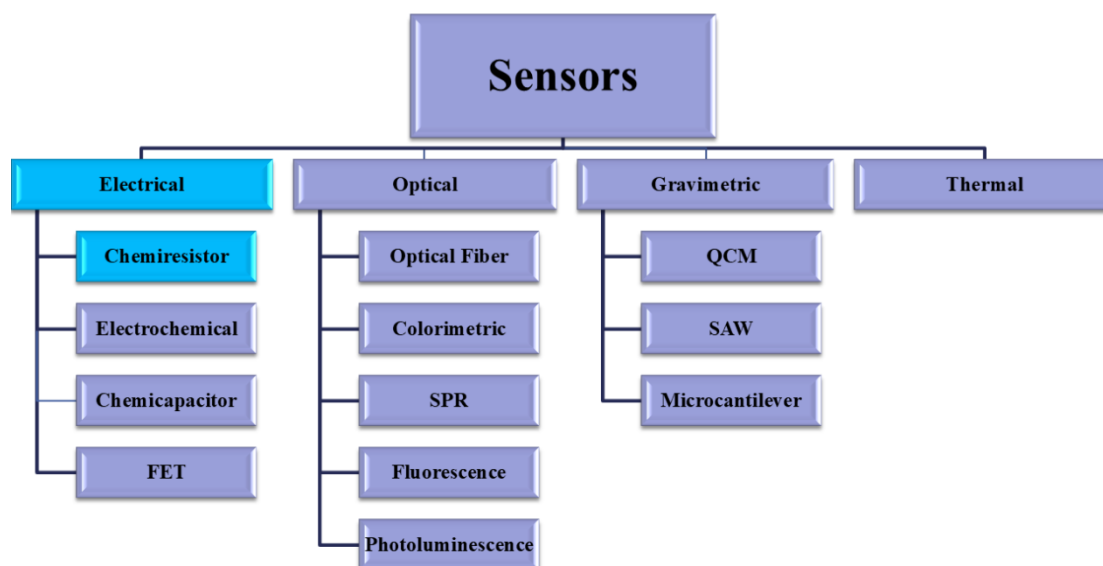
Fig. 1.2: Various types of sensors and sub-categories

In the electric category, sensors are subdivided further into chemiresistors, chemicapacitors, and field-effect transistor (FET)-based sensors. Optical sensors are subclasses that include optical fiber, colorimetric, fluorescence, photoluminescence, and surface plasmon resonance (SPR) sensors. Gravimetric sensors include quartz crystal microbalance (QCM), surface acoustic wave (SAW), and microcantilever-based devices. The current research mainly deals with the fabrication of chemiresistive sensors based on nanocomposites of two-dimensional (2D) materials and metal oxides for volatile organic compound (VOC) and gas detection purposes. Chemiresistive sensors are a type of chemical sensors that show measurable resistance changes in response to gaseous analytes, especially VOCs [25, 26]. The degree of resistance variation is directly proportional to the target gas concentration, making detection and quantification possible. Since their development in the 1960s, chemiresistive sensors have attracted very high interest as a result of their ease of fabrication, low operational expense, easy integration with electronic circuitry, high sensitivity, and chemical and thermal stability [16, 27]. These properties have allowed them to be utilized in a wide

range of applications such as environmental monitoring, industrial process monitoring, food quality determination, automotive exhaust gas detection, defense systems, and medical diagnosis [28–36].

A common chemiresistive gas sensor is an active sensing layer that has been deposited over a proper substrate like glass, indium tin oxide (ITO)-coated glass, or fluorine tin oxide (FTO)-coated glass. Metal electrodes such as Al, Ag, or Au are deposited over the sensing film to create electrical contacts. Sensor resistance is determined through a multimeter or an electrical measurement unit attached via these electrodes. A schematic diagram indicating the structure of a chemiresistive sensor is given in Fig. 1.3. During the last decades, numerous nanomaterials-such as 2D materials, metal oxides, metal nanoparticles, conducting polymers, and nanocomposites-have been studied for VOC sensing in chemiresistive setups [8, 12, 37-39].
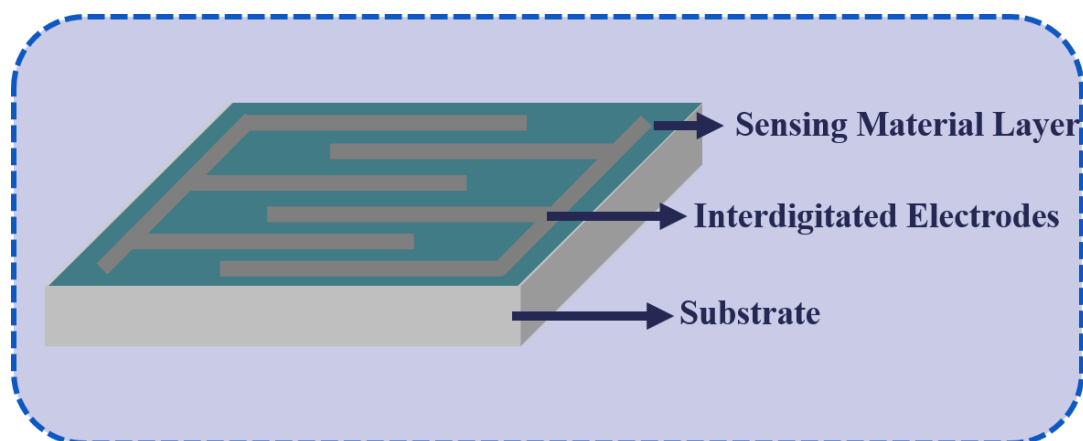

Fig. 1.3: Schematic diagram of a simple chemiresistor sensor

1.2.1 Key Gas Sensing Performance Parameters

The operation of a gas sensor is typically evaluated with some basic parameters as explained below:

1. **Response:** The sensor response indicates the change in resistance or current when exposed to target gas molecules. The response may be described differently based on the type of gas:

$$\text{Response} = \frac{R_g}{R_a} \text{ (for reducing gases)}$$

$$\text{Response} = \frac{R_a}{R_g} \text{ (for oxidizing gases)}$$

where R_g and R_a represent the sensor resistance in the presence of gas and in air, respectively.

The relative response (%) can be calculated as:

$$\text{Relative response (\%)} = \frac{R_g - R_a}{R_a} \times 100 \text{ (for reducing gases)}$$

$$\text{Relative response (\%)} = \frac{R_a - R_g}{R_g} \times 100 \text{ (for oxidizing gases)}$$

The sensitivity is defined as the change in response per unit concentration of the analyte:

$$\text{Sensitivity} = \frac{\text{Response}}{\text{Gas concentration}}$$

2. **Response Time:** The response time is the time taken by the sensor to reach 90% of its maximum response when it is exposed to the target gas. A shorter response time is desirable in practical sensing.

3. **Recovery Time:** Recovery time is the time taken by the sensor to come back to 10% of the original value when the gas is removed. Rapid recovery guarantees enhanced sensor reusability and reliability.

4. **Selectivity:** Selectivity describes the ability of the sensor to detect a particular gas preferentially over other interfering gases under the same conditions.

5. **Reproducibility:** Reproducibility describes the capacity of a sensor to produce uniform responses under the same operating conditions in repeated measurement cycles.

6. **Stability:** Stability is the sensor's consistency in terms of its performance over a long time under stable experimental conditions.

1.3   Choice of Gas Sensing Materials

Nanomaterials have overhauled the technology of gas sensing in recent years because of their remarkable physicochemical and electronic behavior. Scientists across the globe have prepared and studied various nanostructures for numerous sensing tasks.

Nanomaterials are most often described by dimensionality as zero-dimensional (0D), one-dimensional (1D), two-dimensional (2D), and three-dimensional (3D) structures. 0D nanomaterials (such as quantum dots, nanodots) have confinement in every spatial dimension. 1D nanomaterials, including nanowires, nanorods, and nanotubes, possess a single extended dimension, resulting in effective charge transport. 2D nanomaterials exhibit atomic or few-layer thickness and normally exist as nanosheets, nanoflakes, or nanoplates. 3D nanomaterials (e.g., foams, polycrystals) comprise networked nanoscale building blocks. A dimensional generalization of sensing nanomaterials is depicted in Fig. 1.4.
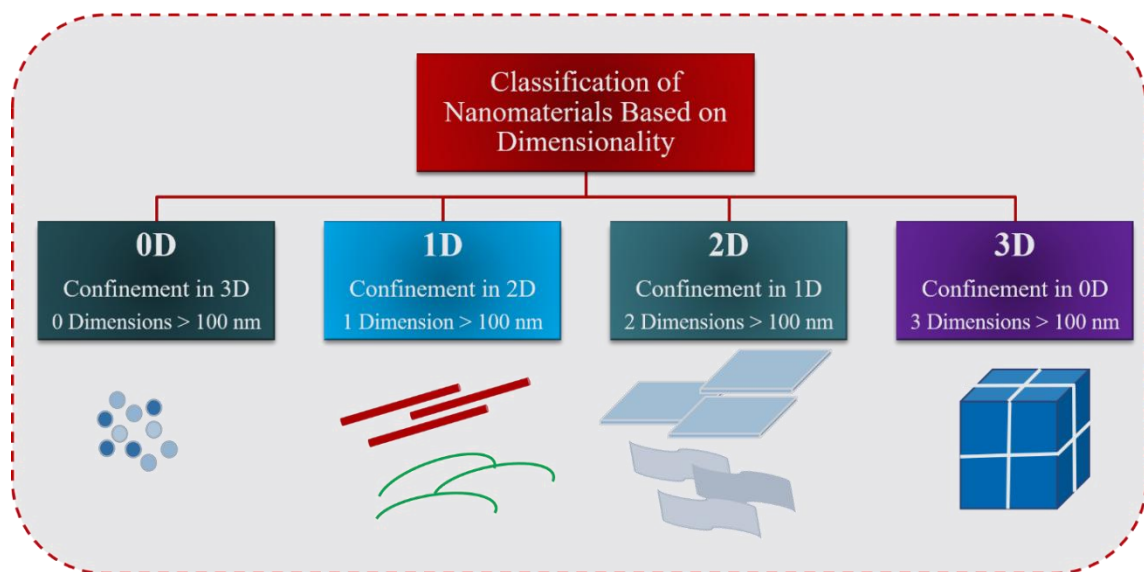
Fig. 1.4: Classification of sensing nanomaterials based on dimensionality

Interest in 2D nanomaterials accelerated after the discovery of graphene in 2004 [40]. Their remarkable electrical, optical, and chemical properties, which are a result of electron confinement in atomically thin sheets, qualify them as exceptional potential candidates for gas sensing. The elevated surface-to-volume ratio and van der Waals gaps facilitate gas adsorption and charge transfer on the surface [41]. These features make 2D materials very versatile—both for gas sensing and other applications such as

energy storage, catalysis, electronics, optoelectronics, and biosensing [4245]. 2D materials are generally categorized as elemental 2D allotropes and covalently bonded compounds. Some of the notable ones are graphene, transition metal chalcogenides (TMCs), graphitic carbon nitride (g-C_3N_4), and MXenes [46].

Transition metal chalcogenides (TMCs) are an important group of 2D materials with tunable optical, electrical, and catalytic properties. From a structural point of view, they may be divided into three subclasses [47]:

1. Transition Metal Dichalcogenides (TMDs) – Semiconductors with the formula MX_2, where M is a transition metal (groups 4-10) and X is a chalcogen (S, Se, or Te).

2. Metal Monochalcogenides (MCs) – Compounds of the formula MX, where M comprises Al, Ga, In, Tl, Ge, Sn, Pb, or Sb, and X is S, Se, or Te.

3. Transition Metal Trichalcogenides (TMTs) – MX_3 compounds in which M can be Ti, Zr, Hf, V, Nb, Cr, etc., and X represents S, Se, or Te.

These TMCs provide versatile opportunities for surface modification and the construction of heterostructures, thus making them highly promising substrates for next-generation gas sensing devices.

1.3.1   Transition Metal Dichalcogenides (TMDs)

Alongside graphene and its derivatives, transition metal dichalcogenides (TMDs) represent one of the most widely explored families of two-dimensional (2D) nanomaterials [46]. These materials exhibit tunable electronic structures, rich chemical versatility, and semiconducting properties highly favorable for gas sensing. The ability of TMD-based sensors to detect target analytes even at room temperature (RT) has positioned them as promising candidates for next-generation gas sensing devices [48].

Despite these advantages, TMD-based sensors still face several challenges that limit their large-scale industrial application. Common issues include slow response and recovery kinetics, poor selectivity due to cross-sensitivity, and signal instability under continuous operation [31]. To overcome these limitations, researchers have explored

various surface modification strategies-such as noble metal functionalization, chemical doping, surface functionalization, heterostructure formation, and hybridization with metal oxides-to enhance their sensing performance [41-43].

Over the last few years, extensive efforts have been focused on transition monochalcogenide-transition dichalcogenide (TMC-TMD) nanocomposites and heterojunctions, where the complementary benefits of each material class are combined. These heterojunction hybrid structures can be prepared in various morphologies-nanoparticles, nanorods, nanosheets, and hierarchical architectures-by inexpensive physical or chemical methods. The fact that these structures can be deposited on a broad variety of substrates, ranging from metallic and semiconducting to crystalline, amorphous, and flexible polymeric supports, renders them extremely versatile for the fabrication of practical sensors.

The construction of TMC-TMD nanocomposites possesses a number of unique benefits for gas sensor applications [41, 49]:

1. TMDs provide excellent platforms for the regulated nucleation and development of monochalcogenides, allowing for uniform size distribution and customized morphology.

2. The inclusion of TMCs avoids aggregation and restacking of TMD layers, enhancing structural stability and ensuring high surface accessibility.

3. The high surface area and rich active sites of TMDs promote uniform dispersion and robust interfacial coupling with monochalcogenide domains.

4. The synergistic heterojunction between the TMC and TMD components promotes efficient charge transfer, band alignment modulation, and enhanced electrical, optical, and electrochemical properties.

Among the family of transition metal dichalcogenides, molybdenum diselenide ($MoSe_2$) has attracted increasing attention for gas-sensing applications due to its excellent physical and chemical properties. These include high charge carrier mobility, strong adsorption affinity toward gas molecules, ease of surface functionalization, large specific surface area, good air stability, and the ability to form stable dispersions in various solvents [38,

50-52]. In addition, MoSe$_2$ can be prepared via multiple scalable routes with a high yield, and its intrinsic surface defects further enhance chemical reactivity and improve suitability for sensor fabrication. So far, a number of studies have demonstrated that pristine MoSe$_2$ exhibits excellent sensitivity toward a wide range of target gases, including ethanol, H$_2$S, NH$_3$, and NO$_2$, and thus is proven to be a promising, sensitive gas-sensing material [53-56]. However, intrinsic MoSe$_2$ mostly suffers from poor response and recovery characteristics, limiting its real-time sensing capability. To date, a significant amount of research efforts have focused on how to hybridize MoSe$_2$ with metal oxides or other functional materials that can help improve the surface reactivity, charge transfer dynamics, and overall sensing performance of MoSe$_2$, paving the way toward practical and efficient gas sensors.

Tin disulfide (SnS$_2$) with n-type semiconductor behavior from the family of IV-VI metal chalcogenides has gained extensive interest due to its unique structural, electronic, and chemical properties for gas-sensing applications [57-58]. It crystallizes in a hexagonal (CdI$_2$-type) layered crystal structure in which tin atoms are sandwiched between two sulfur atom layers, and the weak van der Waals force holds the adjacent sulfur atom layers together. This layered configuration allows easy exfoliation into ultrathin nanosheets, possessing a high surface-to-volume ratio and rich active sites for gas adsorption [59]. SnS$_2$ has a relatively wide bandgap of 2.2 eV, excellent chemical stability, and strong optical absorption in the visible region, suitable for optoelectronic and sensing applications. Moreover, SnS$_2$ can be prepared through simple, cost-effective, and scalable routes, such as hydrothermal, solvothermal, and CVD methods [60-62]. The gas-sensing ability of SnS$_2$ primarily arises from its high surface reactivity, efficient charge transfer, and modulation of electrical conductivity upon interaction with gas molecules. Besides that, tunable morphology from nanoparticles, nanosheets, to nanoflowers will allow optimization of surface properties with an ultimate aim to improve sensing performances [63]. Owing to these attributes, SnS is considered an excellent electron acceptor material and a suitable counterpart for constructing heterostructures with p-type semiconductors like SnS, leading to improved charge separation and enhanced sensitivity toward reducing gases like ethanol.

1.3.2   Metal Monochalcogenides (MCs)

Metal monochalcogenides (MCs) have just become a major family of two-dimensional (2D) layered materials for gas sensing due to their earth-abundant nature, environmental friendliness, and tunable electronic structure, as well as high surface reactivity toward adsorbates [41, 64-66]. Crystallographically, MCs are made up of layers that consist of covalently bonded metal and chalcogen atoms within the plane and weakly coupled adjacent layers with van der Waals interactions [67, 68]. This anisotropic bonding supports easy mechanical or chemical exfoliation into few-layer or monolayer sheets, thus exposing a high density of surface-active sites for gas adsorption and charge exchange.

MCs can be prepared through various physical and chemical pathways, such as chemical vapor deposition, solvothermal synthesis, and mechanical exfoliation, allowing for accurate control over stoichiometry, crystallinity, and morphological characteristics. They possess highly layer-dependent electrical, optical, and mechanical characteristics that can further be tuned through defect engineering, doping, or surface functionalization techniques [69-71].

In gas sensing, MC-based nanostructures usually function by a surface charge-transfer mechanism similar to that of transition metal dichalcogenides (TMDs). The sensing signal originates from modulation of the carrier density upon target gas molecule adsorption or desorption, which changes the overall material resistance. The efficacy of the process is greatly controlled by the type of the gas–surface interaction, the density of surface defects, and the local electronic environment. While adsorption on the clean basal plane typically yields weak physisorption and a restricted charge transfer, the presence of sulfur vacancies, edge defects, or dopants with heteroatoms drastically increases chemisorption as well as rapid and reversible charge transfer, thus enhancing overall sensor performance.

Tin sulfide (SnS) is one of the most widely investigated p-type metal chalcogenides for gas-sensing applications. It belongs to the IV-VI semiconductor family and crystallizes in an orthorhombic structure with a narrow bandgap of approximately 1.3 eV [72]. Owing to its high optical absorption in the visible range, environmental benignity, and

chemical stability, SnS has emerged as a promising material for various optoelectronic and sensing applications [73-74]. Furthermore, it can be synthesized through simple, cost-effective, and scalable methods, making it suitable for large-scale fabrication. The attractive electronic characteristics, structural flexibility, and abundance of active surface sites contribute to its ability to detect a wide spectrum of reducing and oxidizing gases. Among different morphologies, one-dimensional (1D) SnS nanostructures, such as nanorods, nanowires, and nanosheets, exhibit superior sensing performance owing to their high aspect ratio, enhanced charge transport along the axial direction, and large surface-to-volume ratio [75-76]. Studies have demonstrated that 1D SnS nanostructures possess improved electrical conductivity and gas adsorption capability compared to their bulk or spherical counterparts [77]. These attributes make 1D SnS nanorods particularly attractive for constructing SnS/SnS_2 heterostructured nanocomposites aimed at achieving efficient ethanol gas sensing. The superior sensing characteristics of SnS also stem from its inherent defect chemistry. As a p-type semiconductor, SnS exhibits moderate bandgap energy, high intrinsic carrier concentration, and notable Hall mobility. The native p-type behavior primarily originates from the presence of tin vacancies and sulfur interstitials, which act as acceptor-type defects. Conversely, the formation of sulfur vacancies can introduce donor levels near the conduction band, leading to partial n-type conductivity under specific synthesis or operational conditions. This defect-driven tunability provides an additional degree of control over the electronic and sensing properties of SnS-based materials.

Experimental works and theoretical modeling have both shown that the SnS gas-sensing response is significantly controlled by its defect topography, i.e., the type and density of cationic (V^+_{Sn}) and anionic (V^+_S) vacancies [78]. These defects play a key role in controlling surface adsorption energetics, charge transfer kinetics, and carrier modulation during gas-solid reactions. Therefore, defect engineering-by way of controlled synthesis conditions, post-annealing processing, or heteroatom doping-is a vital method for adjusting the electronic structure and improving low-temperature gas-sensing properties of SnS-based devices.

Heterojunction engineering is a potent way to optimize the gas-sensing performance of materials by modulating interfacial charge transfer and adjusting electronic properties
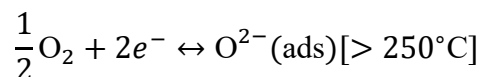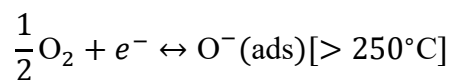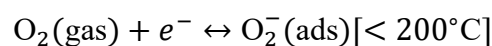
[79]. In this respect, the fabrication of SnS/MoSe$_2$ (p-p) and SnS/SnS$_2$ (p-n) heterojunctions has its specific advantages. For one thing, the matched band alignment in the SnS/MoSe$_2$ p-p heterojunction allows efficient hole transfer, with consequently reduced charge recombination, thus greatly improving sensitivity and accelerating the response. On the other hand, a SnS/SnS$_2$ p-n heterojunction can establish a built-in electric field at the interface, which significantly enhances the rapid separation of charge carriers and makes the depletion layer strongly modulated during gas adsorption [80-81]. This interfacial effect indeed enhances the response, selectivity, and recovery characteristics of the sensor [82]. In all, the combination of SnS with MoSe$_2$ and SnS$_2$ through heterojunction engineering adequately utilizes their respective properties for synergistically improved performances toward gas sensing.

1.4   Gas Sensing Mechanism

The gas-sensing process in two-dimensional (2D) materials is largely controlled by surface-mediated charge transfer reactions that happen as a result of interaction between adsorbed gas molecules and active sites of the sensing layer. Upon exposure to target analytes, there occurs gas adsorption via physisorption or chemisorption, resulting in electron transfer between the adsorbate and the 2D material. This charge transfer across interfaces controls the concentration of the majority carrier in the material, leading to observable changes in electrical resistance or conductance of the material.

In the case of p-type 2D semiconductors, like some transition metal dichalcogenides (TMDs) and monochalcogenides, exposure to reducing gases (e.g., NH$_3$, H$_2$S, or ethanol) donate electrons to the material, thus lowering hole concentration and enhancing electrical resistance. Conversely, oxidizing gases (such as NO$_2$ or O$_3$) strip electrons from the surface, resulting in an increase in hole concentration and a corresponding decrease in resistance [41, 83]. Re-exposure to ambient air causes the desorption of the gas species to reverse the original carrier equilibrium, enabling the sensor to regain its baseline resistance. Kinetics and reversibility of this process of adsorption-desorption are important parameters controlling the response and recovery behavior of the sensor device.

In 2D nanomaterials, the gas-sensing behavior is predominantly governed by surface oxygen adsorption and the subsequent ionization processes. When exposed to air, oxygen molecules get chemisorbed on the semiconductor surface and trap electrons from its conduction band, resulting in the generation of negatively charged oxygen species. This electron removal forms a surface depletion layer and band bending close to the surface, and has a considerable effect on the electrical conductivity of the material. The chemistry of the adsorbed oxygen species is highly dependent on temperature, represented by the following equilibria:

$$O_2(\text{gas}) + e^- \leftrightarrow O_2^-(\text{ads})[< 200°C]$$

$$\frac{1}{2}O_2 + e^- \leftrightarrow O^-(\text{ads})[> 250°C]$$

$$\frac{1}{2}O_2 + 2e^- \leftrightarrow O^{2-}(\text{ads})[> 250°C]$$

For n-type metal oxide semiconductors, oxygen species adsorption and ionization cause the removal of electrons from the conduction band, and an electron-depletion layer forms close to the surface. Upward band bending and an accompanying rise in the electrical resistance of the material result from this depletion region. When exposed to reducing gases like H_2, CO, or NH_3, the gas molecules adsorbed on the surface react with the ionized oxygen species (O_2^-, O^-, or O^{2-}) and release the electrons back into the conduction band. This process of electron reinjection decreases the depletion region width, thus lowering the total resistance of the sensor. On the other hand, in p-type metal oxides, oxygen adsorption removes electrons from the valence band, creating hole accumulation at the surface and reducing resistance, whereas interaction with reducing gases results in an increase in resistance because of hole compensation. As these surface redox reactions are temperature-activated, effective charge transfer and quantifiable sensing responses are generally realized at high operating temperatures [41].

1.5   Primary Challenges and Strategies

In spite of advances of significant magnitude in material science and sensor structure, the development of highly sensitive, selective, and long-term operational stability gas sensors for large-scale or industrial usage is a challenge still to be overcome. The main

restriction is related to low selectivity to single analytes, signal drift upon extended operation, and slow response and recovery kinetics. Breaking these bottlenecks demands a full grasp of the physicochemical mechanisms underlying gas–solid interactions, such as adsorption thermodynamics, charge transfer kinetics, and surface defect chemistry.

Improved nanotechnology has opened new avenues to tailor and optimize these parameters through controlled structure and composition at the nanoscale. Introducing nanostructured architecture allows for a significant enhancement of the effective surface-to-volume ratio, which consequently offers an elevated density of active adsorption sites. In parallel, surface chemistry and electronic structure control through modification contribute to enhanced adsorption kinetics and charge carrier transfer between the sensing layer and target gas molecules. All of these nanoscale phenomena combined contribute toward increased sensitivity, shorter response and recovery times, and higher reliability of future-generation gas-sensing devices.

The unique structural and electronic properties of two-dimensional (2D) nanomaterials, most notably their extremely high surface-to-volume ratio, high density of surface-exposed active sites, and feeble interlayer van der Waals interaction, make them exceptionally well-suited platforms for gas sensing. These properties allow for effective adsorption and desorption of gas molecules while promoting robust interfacial charge transfer between the adsorbate and sensing layer. In addition, the incorporation of 2D materials in nanocomposite or heterojunction architectures invokes synergistic properties resulting from the interaction of disparate electronic structures and complementary chemistries at the surface. These heterostructured devices merge the high electrical conductivity, band-alignment tunability, and fast transport of carriers of 2D semiconductors with the high adsorption capacity and chemical reactivity of their composite counterparts. Such synergism produces more efficient charge transfer, higher selectivity toward target analytes, and faster response and recovery kinetics. Therefore, 2D nanocomposites and heterojunctions hold promise as a next-generation gas sensor based on high sensitivity, stability, and low power consumption under ambient or near-room-temperature conditions.

1.6 Thesis Problem

The current research is committed to the systematic design and synthesis of ethanol gas sensors with the ability to operate efficiently under room-temperature (RT) conditions. The motivation for this research stems from the increasing need for low-power, highly sensitive, and long-lasting sensing devices that can easily be integrated into portable, flexible, or miniaturized electronic platforms. While remarkable progress has been reported in terms of gas-sensing materials and device architectures, the realization of rapid response and recovery behavior, long-term operational stability, and reproducible performance under ambient conditions remains an extremely challenging task.

This thesis primarily addresses the following research objectives:

1. **Room Temperature (RT) Operation:** To design ethanol gas sensors that exhibit stable and efficient operation at room temperature, thereby reducing power consumption and ensuring compatibility with complementary integrated circuit technologies.

2. **Enhanced Performance:** To improve the sensitivity, selectivity, and dynamic response characteristics (response and recovery times) of ethanol sensors using the strategic application of two-dimensional (2D) nanomaterials and their heterostructured or composite configurations.

To achieve the above goals, SnS-doped $MoSe_2$ nanosheets were prepared through a simple and low-cost hydrothermal method for the construction of ethanol gas sensors at room temperature (RT), as explained in **Chapter 3**. The strategy of synthesis allows for uniform distribution of SnS nanoparticles in the $MoSe_2$ matrix to promote effective interfacial charge transfer and improve surface reactivity toward ethanol molecules. In addition, to present enhanced sensing performance, a binary SnS/SnS_2 nanocomposite was then developed, as outlined in **Chapter 4**. The development of the SnS/SnS_2 heterostructure takes advantage of the synergistic coupling between the p-type SnS and n-type SnS_2 phases to enhance carrier transport, perfect band alignment, and overall sensitivity, selectivity, and response dynamics of the ethanol gas sensor..

1.7 Objectives of the Thesis

The overall aim of this thesis is to design, synthesize, and develop sophisticated nanocomposite systems made of 2D nanomaterials and metal oxides for multifunctional applications with special emphasis on chemiresistive ethanol gas sensing. The research framework is specifically planned to create a direct correspondence between material-level design and device-level functionality. The focus is on clarifying the structure–property–function relationships that control sensing behavior so as to optimize operational efficiency, selectivity, and long-term stability under ambient conditions rationally. The specific objectives of the thesis are as follows:

1. Extensive literature survey on 2D nanomaterials and their nanocomposites for gas sensing applications.

2. Synthesis of 2D nanomaterials and their nanocomposites using different synthesis routes.

3. To characterize the structural, morphological, optical, and surface properties of the synthesized materials using advanced analytical techniques such as XRD, FESEM, HRTEM, Raman spectroscopy, FTIR, and BET.

4. To fabricate thin films of nanocomposites via methods such as spin coating, electrophoretic deposition, or drop casting for chemiresistive gas sensor construction.

5. Gas sensing applications of 2D nanomaterials and their nanocomposites for detection of environmental hazards.

Through optimized control of synthesis conditions, accurate microstructural engineering, and thorough functional analysis, the results of this work are structured and reported within five chapters, each outlining the pivotal experimental observations, tests, and accompanying interpretations.

1.8 Organization of the Thesis

The present thesis is systematically organized into five chapters, each dedicated to a distinct aspect of the research, as summarized below:

Chapter 1: Introduction and Scientific Motivation

This chapter introduces the growing need for high-performance gas sensors in general, but with a specific focus on room-temperature (RT) ethanol detection for low-power and portable applications. The chapter presents the basic concepts of chemiresistive gas sensing and critically examines recent developments in ethanol sensing technologies. Particular emphasis is laid on the function of two-dimensional (2D) nanomaterials and their nanocomposites, especially those constituting heterojunction architectures, to amplify sensitivity, selectivity, and operational stability. The chapter also ends with a concise statement of the research problem, motivation, and precise objectives of the current work.

Chapter 2: Experimental Methodologies — Synthesis, Characterization, Sensor Fabrication, and Gas Sensing Measurements

This chapter provides a comprehensive description of the experimental techniques involved in the synthesis of two-dimensional (2D) nanomaterial and their nanocomposites, device fabrication of chemiresistive sensing devices, and gas-sensing performance testing of the same. A hydrothermal route is largely followed to obtain controlled morphology, crystallinity, and phase purity of the resulting nanocomposites. Detailed structural, morphological, and surface analyses are carried out by X-ray diffraction (XRD), field-emission scanning electron microscopy (FESEM), high-resolution transmission electron microscopy (HRTEM), Raman spectroscopy, Fourier-transform infrared (FTIR) spectroscopy, and Brunauer–Emmett–Teller (BET) surface area examination. The gas-sensing properties are thoroughly examined with a specially developed chemiresistive measurement platform in which metal electrodes are deposited by thermal evaporation to provide stable electrical contacts and reproducible sensing performance.

Chapter 3: Highly Selective Sustainable Ethanol Gas Sensor based on p-p heterojunction of SnS/MoSe₂ nanocomposite at room temperature

This chapter outlines the fabrication of a room-temperature (RT) ethanol gas sensor using SnS-doped $MoSe_2$ nanosheets obtained by a hydrothermal route. The introduction of SnS nanoplates into the $MoSe_2$ matrix creates a synergistic interfacial interaction that significantly improves the gas-sensing properties. The maximized

sensor shows an excellent response ($R_g/R_a = 26.8$) to 400 ppm ethanol under dry air conditions, with short response and recovery times of 9.1 s and 15.7 s, respectively. The improved sensing performance is explained in terms of p-p heterojunction formation and potential barrier modulation at the $SnS/MoSe_2$ junction, which enables efficient charge transfer and enhanced surface reactivity toward ethanol molecules.

Chapter 4: SnS/SnS_2 p-n heterojunctions: accumulation layer-driven rapid and highly sensitive ethanol detection at room temperature

Chapter 4 is a continuation of the findings discussed in chapter 3 and is dedicated to the synthesis of a binary SnS/SnS_2 nanocomposite towards realizing superior ethanol-sensing performance under room-temperature (RT) conditions. The sensor optimized shows excellent response ($R_g/R_a = 35.7$) towards 500 ppm ethanol, superfast response, and recovery times of 6.1 s and 18.3 s, respectively, and gives a low detection limit of 10 ppm. The enhanced sensing performance is largely due to the synergistic intercoupling between the p-type SnS and n-type SnS_2 phases, resulting in the establishment of numerous p-n heterojunctions that facilitate effective charge separation, improved carrier transport, and facilitated surface reaction kinetics.

Chapter 5: Conclusions, Future Scope, and Social Impact

This Chapter provides a complete overview and integration of the major conclusions drawn from the research work, with stress on the remarkable benefits of 2D nanomaterial and their nanocomposites in room-temperature ethanol gas sensing. Chapter 5 integrates the general conclusions, underlining the pivotal importance of interfacial engineering, heterojunction formation, and nanoscale structural optimization for enhancing high sensitivity, selectivity, and operational stability. In addition, it presents potential future research directions, such as the architectural optimization of nanocomposite systems, expansion of sensing investigations to other gases, and the integration of developed materials into wearable, self-powered, and flexible sensing platforms for the next-generation practical applications. This work contributes to societal safety and sustainability by enabling low-cost, energy-efficient ethanol sensors operable at room temperature. Such sensors can be applied in breath analyzers, workplace safety monitoring, and environmental surveillance. The use of non-toxic,

earth-abundant materials further supports eco-friendly and sustainable technological advancement.

A schematic representation of the overall thesis organization and research workflow is presented in Figure 1.5 to facilitate a clearer visualization of the sequential progression of the study.
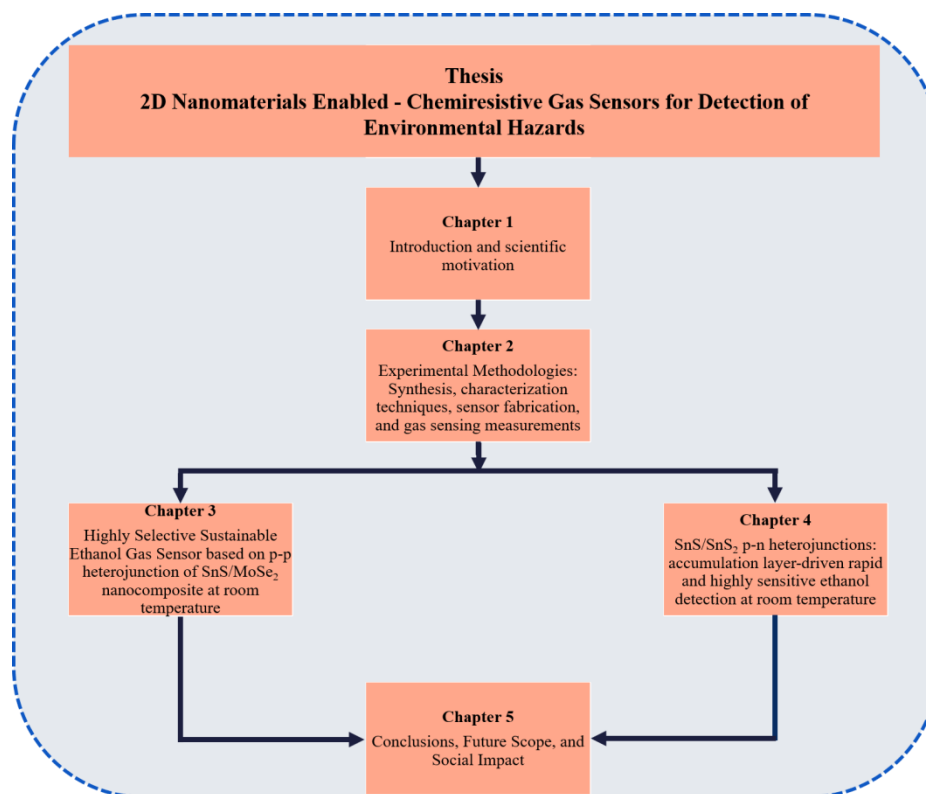
Fig. 1.5: Flowchart for the organisation of the thesis.

CHAPTER 2

Experimental Methodologies: Synthesis, Characterization Techniques, Sensor Fabrication, and Gas Sensing Measurements

This chapter describes in detail the methodologies followed in synthesizing nanocomposites based on 2D nanomaterials, fabricating their film-based gas sensors, and the characterization techniques used in this study. The nanocomposites were synthesized using the hydrothermal method mainly. The structural properties were analyzed by XRD, whereas surface morphology was examined by FESEM and HRTEM. The vibrational modes have been investigated by using Raman spectroscopy and the BET technique for measuring the specific surface area of the nanocomposites. The fabrication of thin films was done by using the EPD technique, followed by the thermal evaporation method to deposit metal electrodes on the synthesized films. A customized chemiresistive gas sensing setup was used for testing the gas sensing performance of the fabricated sensors. A brief summary of all the above experimental procedures is given in this chapter.

2.1 Synthesis of nanocomposites of 2D nanomaterials

Various synthesis techniques have been developed for producing nanocomposites based on 2D nanomaterials possessing tailored structural/functional properties for a variety of technological applications. The synthesis methodologies fall into two basic approaches: (i) top-down and (ii) bottom-up. In the top-down strategy, nanostructures are produced from bulk materials through the processes of solid-solid or gas-solid transformation; this usually involves physical techniques, such as grinding, crushing, or decomposition, to achieve nanoscale features. In contrast, the bottom-up methodology involves the controlled assembly of atoms and/or molecules into nanostructures through chemical reactions and nucleation processes. The selection of an appropriate synthesis route is crucial before the study of material properties and optimization related to intended applications. In addition, a key factor for successful large-scale production and industrial usage of nanomaterials is the production of high-quality material in large quantities with good reproducibility.

In the current study, simple, inexpensive, and eco-friendly hydrothermal approaches were adopted to prepare nanocomposites based on 2D nanomaterials. Accordingly, nanocomposites of SnS, SnS_2, and $MoSe_2$ were prepared. The adopted synthesis methodologies are briefly described in the sections that follow, while detailed experimental procedures are presented in Chapters 3 and 4.

2.1.1 Hydrothermal synthesis route

The hydrothermal synthesis technique was first reported in 1845 by Karl Emil von Schafhäutl, a German geologist, who described the crystal formation under hydrothermal conditions. Since then, continuous research and technological developments have remarkably refined the method to establish it as one of the versatile and effective methods for synthesizing a wide range of nanomaterials. The hydrothermal synthesis usually involves chemical reactions that take place in a sealed Teflon-lined stainless-steel autoclave, where precursor materials dissolved in water will undergo controlled temperature and pressure conditions. With the intent of obtaining nanomaterials with desired morphology and structural characteristics, a specific volume of aqueous precursor solution is cautiously loaded into the Teflon liner for appropriate

internal pressure inside during the reaction, while avoiding overfilling that would lead to spilling. Precise optimization of synthesis parameters such as temperature, pressure, and reaction duration in the high-temperature oven yielded a high amount of well-crystallized nanomaterials [2]. Figure 2.1 illustrates the schematic setup of hydrothermal autoclave used in the synthesis. The main constituents that are involved in the hydrothermal reaction are described below.

1. **Reactant precursors:** These are the main chemical compounds, which serve as the initial raw materials for the hydrothermal reaction. Dissolution in appropriate solvents under specified conditions yields a chemical transformation into the desired nanomaterial.

2. **Mineralizing agents and supplementary additives:** Quite often, acids or bases are added during synthesis to adjust the pH of the reaction medium. These compounds, called mineralizers, have a decisive influence on the dissolution and recrystallization processes. In this respect, many additives are also used, among which one can mention different types of reducing agents, complexing agents, capping agents, and stabilizers, which enable control over the growth, morphology, and stability of the synthesized nanomaterials.
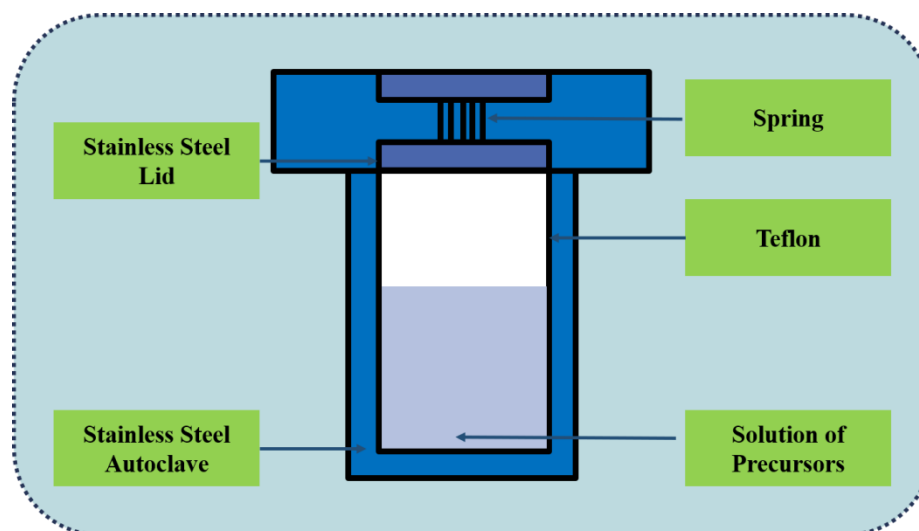
Fig. 2.1: Set-up of the hydrothermal autoclave used in the hydrothermal synthesis.

The hydrothermal technique presents several striking advantages that make it a desirable procedure for the synthesis of nanomaterials:

1. **Cost-effectiveness and scalability:** the process is economically viable and suitable for large-scale production, making it ideal both in laboratory and industrial applications.

2. **Morphology and size control:** This method allows critical control of particle size, shape, and morphology to synthesize nanomaterials with controlled structural and functional properties.

3. **Integration with other synthesis techniques:** The hydrothermal approach can be coupled well with other techniques, such as sonochemical, electrochemical, and microwave-assisted techniques, which extends its applicability to new nanomaterials development.

4. **Convenient experimental setup:** The apparatus is quite simple in its nature, has operational ease, and can be reused for every synthesis process, which enhances its practicality and efficiency.

2.2   Characterization techniques

Various characterization techniques have been employed to verify the successful formation of nanocomposites of 2D nanomaterials and metal oxides. The structural study begins with X-ray diffraction (XRD), followed by morphological analysis using field-emission scanning electron microscopy (FESEM) and high-resolution transmission electron microscopy (HRTEM). Raman spectroscopy has been utilised for the analysis of vibrational modes. Fourier transform infrared spectroscopy (FTIR) has been employed for examining the functional groups. This section provides a concise overview of the operating principles of each characterization approach used in our research.

2.2.1   X-ray diffraction (XRD)

XRD is one of the most versatile and powerful analytical techniques that has been applied widely for a range of purposes: crystallographic studies, phase identification, strain and crystallite size determination, calculation of thermal expansion coefficients and densities, crystal texture analysis, sample crystallinity assessment, estimation of dislocation density, etc. [4]. The source of powder X-ray diffraction dates back to the

early years of the 20th century, with Debye, Scherrer, and Hull laying the foundation between 1916 and 1917 for what is presently described as modern powder diffraction research [5,6].

The technique, however, has undergone immense developments over the succeeding decades, especially with the development of computational methods in the latter half of the 20th century. The big leap came when, in a breakthrough, Hugo Rietveld introduced a novel approach involving the computer-assisted refinement of entire powder diffraction patterns, a technique now known as Rietveld refinement. This method revolutionized crystallographic analysis by making it possible to model complex diffraction data with unprecedented accuracy, made feasible by the increase in computational power at that period.

In modern applications, XRD analysis depends on advanced algorithms that are able to solve complex crystal structures in powder form. The transition from early transmission experiments, which dealt with simple cubic crystals, toward the contemporary analyses capable of refining complex structures containing thousands of atoms per unit cell, highlights the progress achieved in X-ray diffraction over the past hundred years.
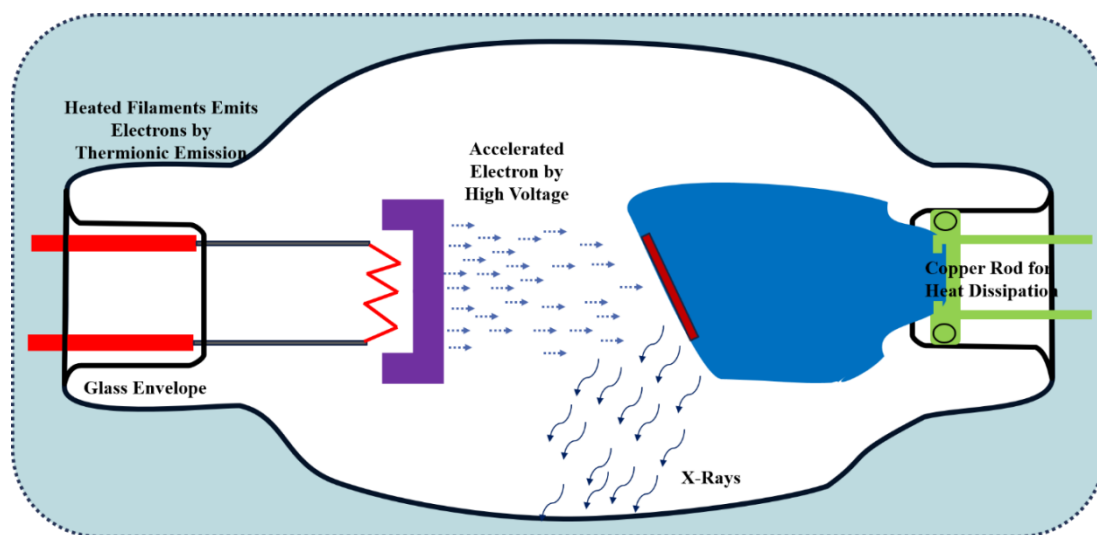
Fig. 2.2: Schematic showing the generation of X-rays in an X-ray tube.

X-rays are produced by a vacuum tube that is specially designed to generate electromagnetic radiation over a wide range of wavelengths, typically from 0.1 Å to 100 Å. However, for diffraction studies, X-rays in the range from 0.5 Å to 2.5 Å have

traditionally been selected since they closely match the interatomic spacings in crystalline materials so that effective diffraction analysis may be carried out. Given below is a schematic of the system used for generating X-rays. The apparatus essentially consists of an X-ray tube enclosed in a vacuum chamber equipped with a cathode and an anode assembly.

The cathode, in this arrangement, is usually made up of a tungsten filament, while the anode target is made of copper. If the tungsten filament is heated, it emits high-energy electrons which, under an applied potential difference (usually in the range of 30-60 kV), are accelerated to the copper anode. At such impact, these high-energy electrons remove inner-shell (K-shell) electrons from copper atoms. The electrons at higher energy levels (L and M shells) jump to fill these vacancies, emitting characteristic X-rays—identified as CuK_α and CuK_β—with wavelengths of approximately 1.54 Å and 1.39 Å, respectively. A nickel filter is used in order to obtain monochromatic X-radiation for accurate diffraction measurements; this absorbs the CuK_β radiation, allowing only the CuK_α line [λ = 1.54 Å] to go through for analysis [7].

In 1913, William Henry Bragg and William Lawrence Bragg published a milestone in the knowledge about crystalline materials: X-rays are reflected characteristically when they impinge on crystal lattices. They realized that the X-rays scattered from a crystal are of intensity maximum at certain angles and wavelengths. In fact, these angles depend on the regular arrangement of atoms inside the crystal. W. L. Bragg suggested that one might consider any crystal structure as parallel atomic planes with an interplanar spacing-a certain distance d-separating them. Sharp diffraction peaks occur as a result of constructive interference by incident X-rays that are reflected from the atoms lying in these planes.

Constructive interference occurs when X-rays reflected from successive parallel planes have a path difference of an integral multiple of the wavelength. This is the condition, now commonly called Bragg's Law, which relates the angle of incidence to interplanar spacing in the crystal. A schematic representation of this concept is shown in Fig. 2.3. The mathematical form of Bragg's condition for constructive interference can be written as follows:

$$2dsin\theta = n\lambda \tag{2.1}$$

Here, the integer "n" denotes the order of diffraction.

Bragg reflection occurs for those wavelengths of the incident X-rays, λ, which satisfy the condition λ ≤ 2d and embraces the range in which diffraction from crystalline structures can be observed. The resulting diffraction peaks occur at specific angular positions dependent on various crystallographic parameters, which include the unit cell dimensions, space group symmetry, and overall symmetry of the crystal lattice. These structural attributes collectively influence both the position and intensity of the diffraction peaks. The relationship governing the intensity distribution of the diffracted X-rays can be expressed mathematically as follows:

$$F_{hkl} = \Sigma f_n e^{2\pi(hu_n + kv_n + lw_n)} \tag{2.2}$$

The atomic coordinates within the crystal lattice are given by (uvw), the Miller indices of the crystal planes are represented by hkl, and f_n is the electron scattering factor of each atom. Such an analytical expression is particularly applicable for powdered samples where there are several crystallites oriented in all directions within the sample, enabling the incident X-ray beam to encounter all the possible lattice planes which satisfy Bragg's condition. This leads to a diffraction pattern comprising peaks corresponding to specific sets of parallel planes, whose angular positions are determined by constructive interference [8]. By X-ray diffraction, it is also possible to estimate the average crystallite size of the material using the relation:

$$D = k\lambda \, \beta cos\theta \tag{2.3}$$

XRD patterns in the present work were recorded on a D8 Advance Bruker diffractometer (Germany) hosted at AIC, Department of Applied Physics, Delhi Technological University, Delhi, India. The data was collected at RT by using CuKα radiation with a wavelength of 1.5406 Å. Acquisition of data was done by step scanning with a step size of 0.02° and a scan rate of 2° per minute. The diffraction patterns obtained were matched with standard reference data from the Joint Committee on Powder Diffraction Standards (JCPDS) database and with the results reported in the literature.
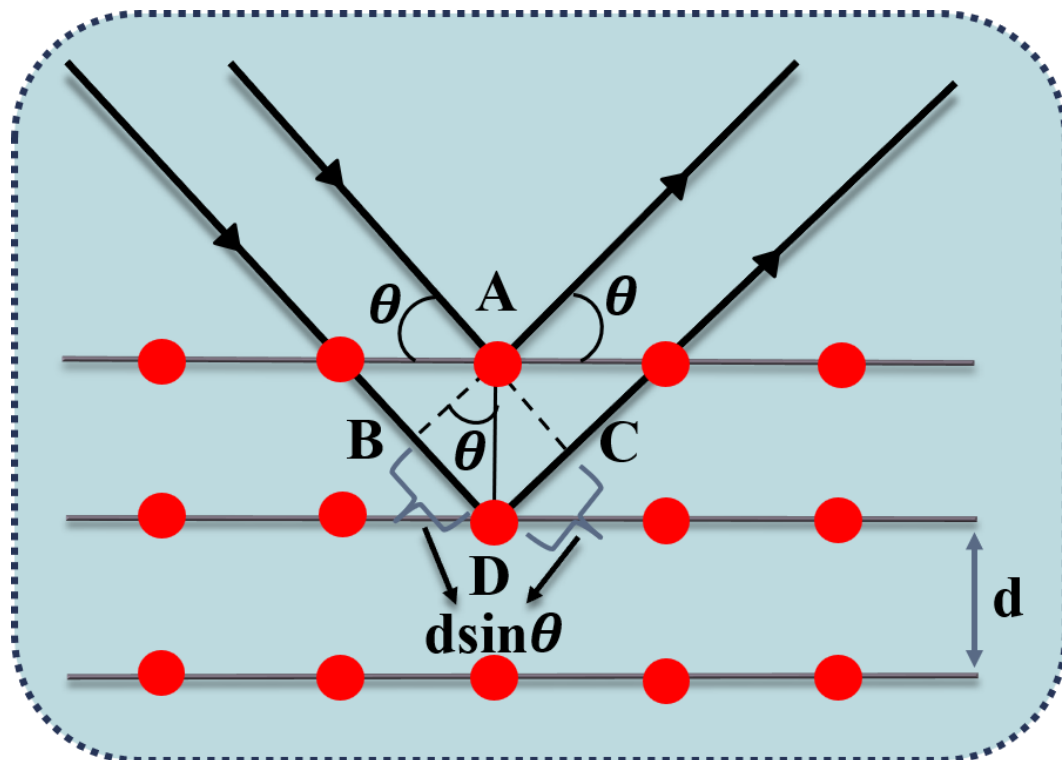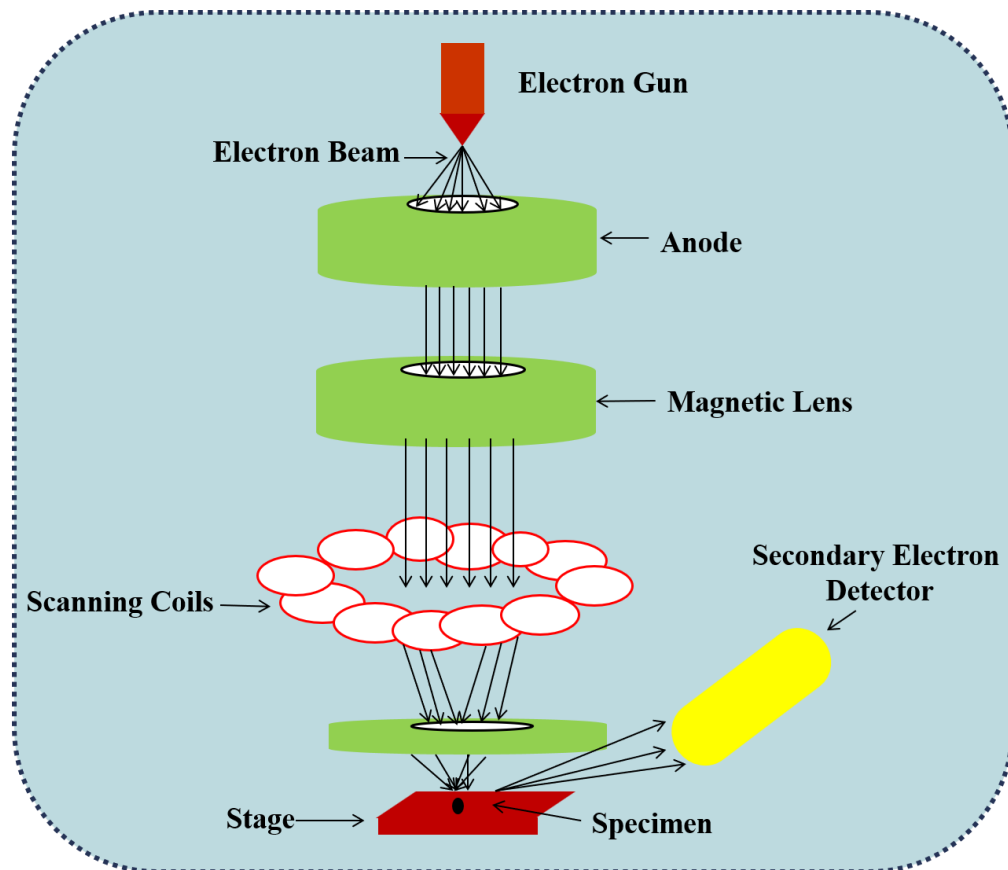
Fig. 2.3: Schematic showing the diffraction of X-rays obeying Bragg's law.

2.2.2   Field-emission scanning electron microscopy (FESEM)

FESEM is a high-resolution imaging technique using a field emission source to produce a finely focused electron beam, which scans the specimen surface in a raster pattern. Compared to SEM, which usually relies on a tungsten filament, a field emission gun in FESEM offers an electron emission intensity higher by as much as three orders of magnitude, thus providing higher resolution and higher quality images [9]. Similar to SEM, FESEM detects secondary electrons emitted from the specimen surface using a scintillator–photomultiplier detector system, which converts the electron signals into photons for image formation. FESEM operates under ultra-high vacuum conditions for stable electron emission and improved precision in imaging. Non-conductive samples are usually coated with an ultrathin conductive layer of gold (Au) or palladium (Pd), while the gold/palladium coating is done to avoid charging effects and improve conductivity before imaging. After emission, the electrons are accelerated and focused into a narrow monochromatic beam using metallic apertures and electromagnetic lenses. A schematic of essential components of the FESEM system is presented in Fig. 2.4.

Fig. 2.4: Schematic showing the components of an FESEM.

Interaction of the incident electron beam with the specimen in FESEM represents a rather complex process. Several types of emitted signals are generated, carrying different information about the sample. Fig. 2.5: The main types of emitted electrons and radiations including the secondary electrons, backscattered electrons, characteristic X-rays, and Auger electrons are produced by this interaction. Secondary electrons are produced when the incident primary electrons transfer enough energy to the outer-shell electrons of the atoms of the specimen to eject them. Because of their low energy and high surface sensitivity, secondary electrons play the major role in topographical imaging, giving high-resolution images with fine surface features and morphology.

Backscattered electrons result from the elastic collision between incident electrons and atomic nuclei in the specimen; the electrons are scattered backward toward the detector. The intensity of backscattered electrons is dependent on the atomic number (Z) of the elements in the sample; materials of a higher atomic number give a more intense BSE signal. This property enables compositional contrast imaging and is thus useful for

distinguishing phases in heterogeneous or multi-component materials. Characteristic X-rays are produced when primary electrons remove inner-shell electrons from the specimen atoms and electrons from higher energy levels drop down to fill those voids. Energy released as a result of this is in the form of X-ray photons with characteristic wavelengths for particular elements. These X-rays are detected and analyzed through Energy-Dispersive X-ray Spectroscopy, also known as EDX, allowing both qualitative and quantitative elemental analysis of the specimen to be performed. The emission of Auger electrons involves a similar process to that of characteristic X-ray emission, but instead, the energy is transferred during the electronic transition to another electron, which is then emitted from the atom. Auger electron emission provides valuable surface-sensitive compositional information and, when applied in conjunction with X-ray analysis, increases the accuracy of elemental characterization.
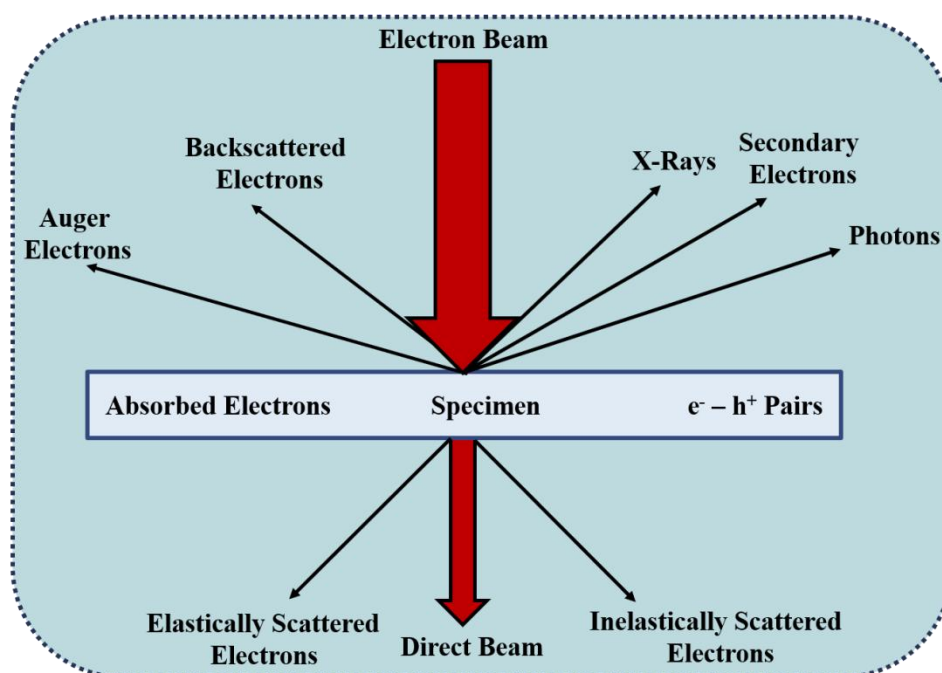
Fig. 2.5: Interaction of electrons with the specimen.

This technique offers exceptional information on both topography and elemental composition at extremely high magnifications, with a nearly unlimited depth of field. FESEM is notably more effective than conventional SEM, providing images with spatial resolutions as fine as 0.5 nanometers and significantly reduced electrostatic distortions [10]. FESEM is renowned for its ability to produce crisper, more accurate images with minimal electrostatic distortions. This capability makes it an invaluable

tool for a broad range of scientific disciplines. Physicists use it for detailed structural analysis of materials, chemists for studying surface reactions, biologists for cellular imaging, material scientists for examining the properties of advanced materials, and electronic engineers for inspecting microchip structures. Its versatility and high-resolution imaging make FESEM indispensable in both research and industry, where observing fine details and understanding complex structures are crucial. The model of the instrument used to study surface morphology of nanocomposites of 2D nanomaterials and metal oxides described in the research work discussed in upcoming chapters is Zeiss Gemini SEM 500 (Germany), available in the University Science Instrumentation Centre (USIC), Delhi University, Delhi, India.FESEM is a technique that provides great insight both into the surface topography and elemental composition at very high magnifications, offering an almost unlimited depth of field. Compared to the conventional scanning electron microscope, FESEM displays superior performance by yielding spatial resolutions down to about 0.5 nanometers and with minimal electrostatic distortions, according to [10]. Its ability to yield sharper and more precise images with enhanced contrast renders FESEM as a powerful tool across diverse scientific and engineering disciplines.

The versatility of FESEM has led to its wide application in various research fields: physicists use it for detailed structural studies, chemists study surface reactions, biologists perform high-resolution cellular imaging, material scientists characterize the microstructural properties of advanced materials, and electronic engineers apply FESEM in microchip inspection and failure analysis. Due to its high resolution, compositional sensitivity, and image precision, FESEM became indispensable in academic investigations and industrial practices when nanoscale structural characterization was necessary.

In the current study, surface morphology of synthesized nanocomposites containing 2D nanomaterials and metal oxides was studied by using a Zeiss Gemini SEM 500 (Germany) available at the University Science Instrumentation Centre (USIC), University of Delhi, Delhi, India.

2.2.3   High-resolution transmission electron microscopy (HRTEM)

Transmission electron microscopy (TEM) is a sophisticated imaging technique that uses an electron beam to pass through an ultrathin specimen, revealing detailed insights into the sample's structure. As the electron beam traverses the specimen, it provides valuable information about the material's morphology and crystallography. TEM operates with electron beams at the nanometer scale, which, due to their shorter wavelength compared to visible light, achieve much higher resolution imaging [11]. The interactions between the electron beam and the specimen contribute to the formation of images. Various imaging technologies are employed to capture these interactions, including fluorescent screens, photographic film, and charge-coupled devices (CCDs). TEM can operate in two primary modes: diffraction mode and image mode.

The typical TEM setup includes an electron gun that generates a high-energy electron beam, which travels through a vacuum tube within the microscope. The beam is focused by condenser lenses and directed onto a specimen mounted on a motorized stage, typically a copper grid coated with the sample. The core components of the TEM apparatus include the objective lens and the specimen chamber, where the transmitted electron beam interacts with the thin specimen [12].

For optimum imaging in TEM, the specimen thickness should be in the range of 100 to 200 nm, since electrons suffer severe attenuation while passing through specimens thicker than 200 nm. High-resolution images and diffraction patterns are produced by an imaging system that includes an objective lens and multiple intermediate and projector lenses. Once the electron beam has passed through the specimen, it is focused and projected onto a fluorescent screen or a CCD camera that records the intensity of electrons as digital pixels to produce high-quality images [13].
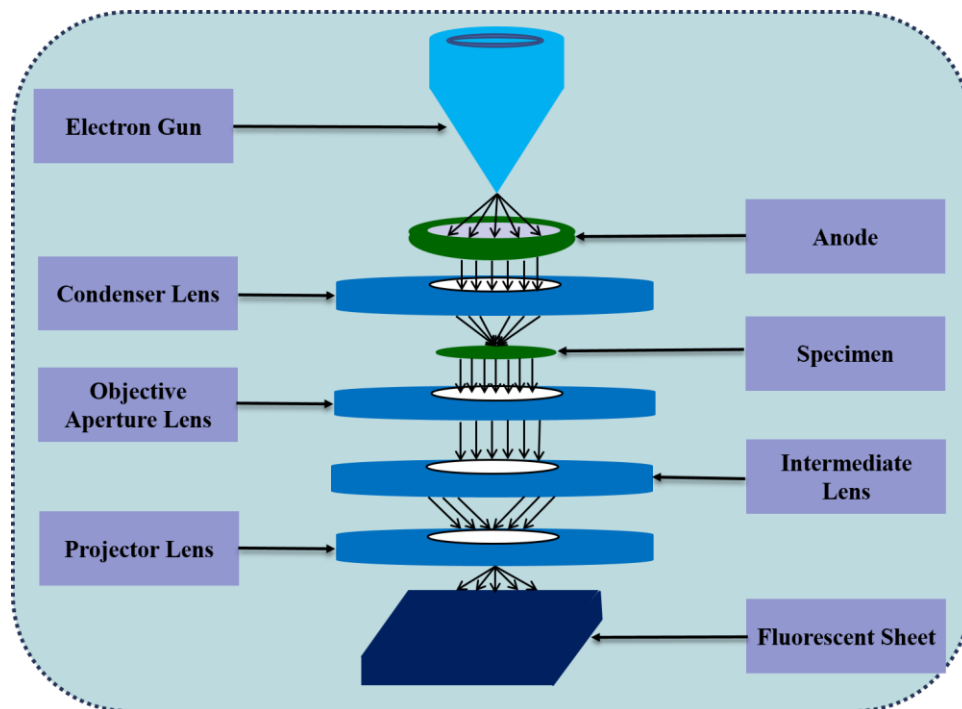
Fig. 2.6: Schematic showing the setup of HRTEM.

The transmission electron microscope (TEM) can be used in various modes, including High-Resolution TEM, Selected Area Electron Diffraction (SAED), and conventional TEM. Each of these modes provides different analytical capabilities. These modes enable the study of structural and microstructural features such as morphology of particles, crystallite size, lattice spacing, and crystal orientation. The general scheme for a typical TEM is presented in Fig. 2.6.

The TEM system works under high-vacuum conditions and is controlled for image acquisition and data processing through a GUI. In the interaction of the electron beam with the specimen, both elastic and inelastic scattering occur. Elastic scattering, where electrons are deflected without any loss of energy, is due mainly to the atomic configuration within the crystal lattice and leads to coherent diffraction patterns. In contrast, inelastic scattering involves energy transfer through absorption or emission and yields information about the chemical composition and electronic structure.

Image contrast in TEM is achieved through Bright-field and Dark-field imaging techniques. The directly transmitted electrons are used to form a bright-field image where the denser regions appear dark against a bright background, while dark-field

imaging enhances the contrast by capturing diffracted electrons through an objective aperture located in the back focal plane of the objective lens so as to provide bright features on a dark background [14].

Small electron wavelengths that allow superior spatial resolution can be obtained by using an increased accelerating voltage of up to 300 kV in the field emission source. The point resolution increases with higher accelerating voltages, allowing for HRTEM images of excellent atomic-scale resolution. The following instruments were used for advanced structural and morphological studies: JEOL JEM-2100F (Japan) at the Advanced Instrumentation Research Facility (AIRF), Jawaharlal Nehru University (JNU), and FEI Tecnai 200 (USA) available at the Sophisticated Analytical Instrument Facility (SAIF), All India Institute of Medical Sciences (AIIMS), New Delhi, India.

2.2.4 Raman spectroscopy

Raman spectroscopy is an analytical technique used for studying rotational, vibrational, and other low-frequency modes of a system. It gives information on the molecular bonding, crystal structure, and chemical composition and hence has a unique spectroscopic fingerprint that identifies the material. It is based on a phenomenon called the Raman effect, which results from the inelastic scattering of monochromatic light by molecular vibrations in a sample [15]. A monochromatic radiation source, usually a laser, is involved in an interaction with the sample, where part of the incident light is reflected, absorbed, or scattered. Most of the scattered light is due to elastic scattering, giving rise to Rayleigh scattering, in which the incident and scattered photons possess the same energy. A small fraction, roughly one in a million photons (10^{-6}), undergoes inelastic scattering, hence causing a shift in photon energy, which yields useful information concerning molecular structure [16].

This inelastic scattering is evidenced by the Stokes and anti-Stokes lines that give rise to the Raman spectrum. In Stokes scattering, the scattered photons have lower energy (longer wavelength) than the incident photons because of energy transferred to molecular vibrations. Conversely, the scattered photons in anti-Stokes scattering have higher energy (shorter wavelength) since energy is transferred from the excited molecules into the scattered photons. Meanwhile, Rayleigh scattering corresponds to

photons with no change in frequency relative to the incident light [17]. A simplified schematic of a Raman spectrometer setup can be seen in Fig. 2.7, which shows the basic components involved in detecting and analyzing Raman signals.
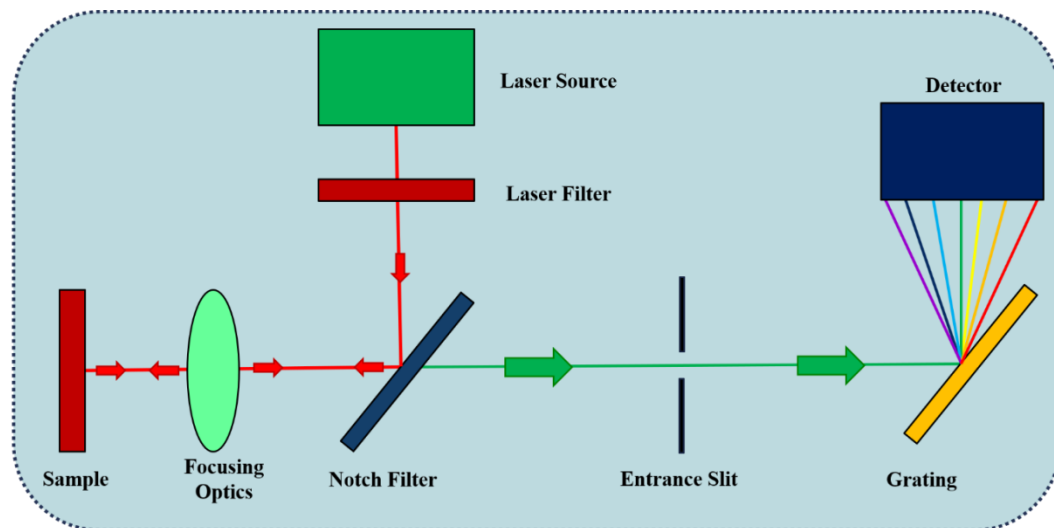
Fig. 2.7: Schematic representation of Raman spectrometer.

The Raman spectrum is usually plotted to show the relationship between scattered light intensity versus the energy shift, called the Raman shift, during photon-molecule interactions. An electric dipole moment is induced in the electric field of a molecule when incident photons interact with it. The induced dipole moment (P) can be expressed as:

$$P = \alpha.E \qquad (2.4)$$

where α is a proportionality constant. This phenomenon provides significant information on the distortion of the electron cloud surrounding the molecules [18]. The energy transitions originating from the variation of the molecular polarizability due to bond vibrations provide the Raman-active modes.

A modern Raman spectrometer typically consists of three key components: a laser source, an optical system for sample illumination, and a spectrometer for signal detection and analysis. Lasers are the preferred excitation sources due to their high monochromaticity and intense, focused beams which both act to enhance the S/N ratio in the recorded spectra. In general, most Raman spectrometers utilize detection systems that involve CCD or FTIR methods, often supplemented with cooled germanium

detectors for minimized noise and therefore increased sensitivity. Compared to infrared (IR) spectroscopy, Raman spectroscopy offers certain advantages in dealing, especially, with inorganic systems in aqueous environments due to its minimal interference from water molecules. It also finds wide applications in the fields of biology and chemistry since it requires minimal sample quantities and is very sensitive to changes in structure, environment, and conformation. In addition, Raman spectroscopy serves as a nondestructive analytical technique that allows qualitative and quantitative identifications of molecular impurities, additives, and compositional changes.

In the present study, Raman analysis of the nanocomposites of 2D nanomaterials and metal oxides was done with the help of the WITec alpha 300 RA (Germany) spectrometer available at the Advanced Instrumentation Research Facility (AIRF), Jawaharlal Nehru University (JNU), Delhi, India.

2.2.5 Brunauer-Emmett-Teller (BET) Analysis

The nitrogen adsorption-desorption isotherm technique remains one of the most widely used methods for characterizing the porous microstructure of materials. This technique offers quantitative information on two important parameters of specific surface area and pore volume, which are essential to understand and optimize materials for functional applications in various areas. Nitrogen gas is normally used as the adsorbate because of its chemical inertness, high availability of purity, a moderately high boiling point at 77 K, and lower cost compared to other inert gases like argon, krypton, and carbon dioxide [23].

Adsorption isotherms are commonly measured based on a theoretical model representing the multilayer gas adsorption on solid surfaces, known as the Brunauer-Emmett-Teller (BET) method [24]. Before the BET theory, the Langmuir model was mainly used, which dealt only with monolayer adsorption. The BET model extended this concept to the possibility of multilayer adsorption, where gas molecules form a monolayer on the surface and additional adsorbed layers accumulate above it. The model assumes that upper adsorbed layers exhibit liquid-like characteristics while being in equilibrium with the vapor phase of the lower layers. Capillary condensation, in turn, is a main phenomenon at subcritical pressures, where one can determine the effective

surface area and mesoporous structure of the material. Nitrogen adsorption measurements are commonly performed within a relative pressure range of 0.05-0.995 at a constant temperature of 77 K. Very valuable information on physisorption mechanisms and pore structure of the sample is obtained by the shape of the resulting isotherm and possibly emerging hysteresis loops. Following the classification suggested by the International Union of Pure and Applied Chemistry, there are six types of adsorption isotherms and four types of hysteresis loops connected with specific geometries of mesopores. In the region of low relative pressures (0.05-0.3), there is monolayer or multilayer adsorption on the walls of micro- or mesopores. The point of the isotherm curve deflection (the so-called "knee") corresponds, as a rule, to the completion of monolayer coverage and serves as a basis for calculations of specific surface area. The BET theory is applicable to non-porous, macroporous, and mesoporous samples but provides less accuracy in the case of microporous systems.

At higher relative pressures, capillary condensation occurs in the mesopores and a liquid-like adsorbed phase is formed. Because pores of different diameters condense vapor at different relative pressures, analysis of this behavior leads to information about pore volume and pore size distribution. The BJH method is commonly used for estimating pore size distribution, assuming cylindrical non-intersecting pores.

The porosity of a material, which is defined as the ratio of volume occupied by pores to the total volume of the solid, can be calculated using the relation:

$$\text{Porosity} = (1 - d_{bulk}/d_{exp}) \times 100 \qquad (2.5)$$

Where d_{bulk} is the X-ray density of the bulk crystallite, and d_{exp} is the experimental density measured using Archimedes' water displacement principle. The present research focuses on the measurement of specific surface area, using a Quantachrome NOVA 2200e (U.S.) instrument housed at the Department of Physics & Astrophysics, University of Delhi, Delhi, India, from the synthesized nanocomposites of 2D nanomaterials discussed in Chapter 3 and 4.

2.3   Gas sensor fabrication

The nanocomposite films comprising 2D nanomaterials and metal oxides were prepared using the electrophoretic deposition technique for sensor fabrication. Thereafter, metal electrodes were deposited onto the synthesized films using the thermal evaporation method.

2.3.1   Electrophoretic deposition (EPD) technique

Electrophoretic deposition (EPD) can be an efficient method for the fabrication of uniform and adherent films by applying an electric field to charged particles suspended in a liquid medium like deionized water, ethanol, acetonitrile, or isopropanol. The technique of EPD is cost-effective and relatively versatile to fabricate thin films. The basic setup of EPD consists of a two-electrode setup placed at a fixed distance inside a glass beaker. A platinum (Pt) rod acts as the RE, and the working electrode (WE), usually a copper (Cu) rod, carries the substrate where the deposition takes place. In order to develop uniform films, the particles have to be well dispersed into the solvent medium-often acetone, ethanol, isopropanol, acetonitrile, chloroform, or distilled water. The applied voltage and deposition time need to be optimized with the purpose of developing films of desired thickness and quality [25–28].
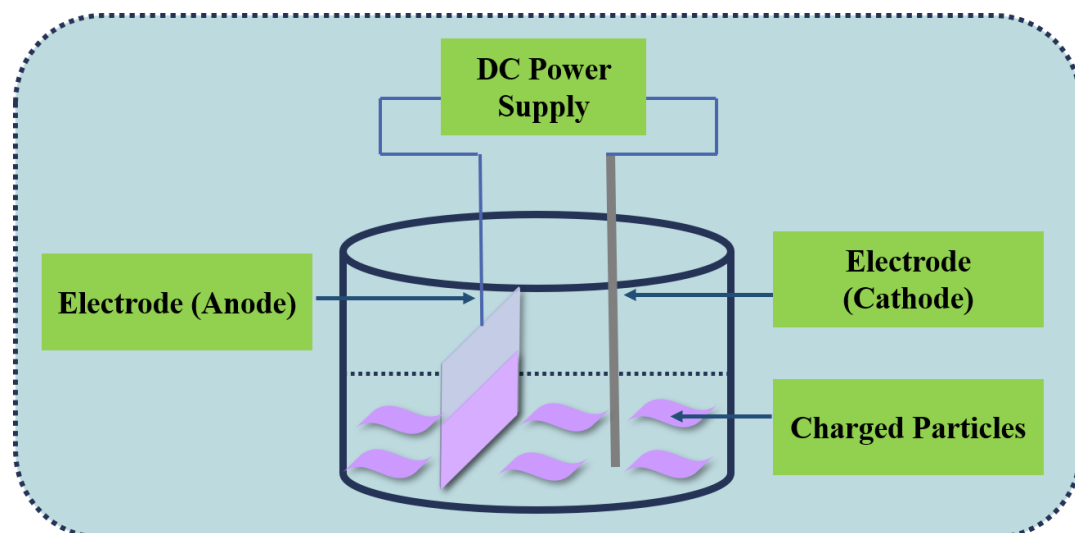
Fig. 2.10: Schematic showing the fabrication of film via EPD technique.

The use of dispersant must be carefully optimized in order to obtain contamination-free films since conductive substrates are essential for this process. Heat treatment after

deposition may be employed to improve film adhesion and stability. A basic schematic of a standard EPD setup is shown in Fig. 10, where charged particles migrate and deposit onto the surface of the substrate due to a DC electric field for an optimized duration.

2.3.2   Thermal evaporation technique for electrode deposition

The thermal evaporation technique is a widely applied process for fabricating electrodes due to its precision, versatility, and possibility of preparing uniform films. This process is implemented under high-vacuum conditions, whereby controlled heating of a solid material results in its evaporation or sublimation. Afterwards, the vaporized atoms or molecules travel in a vacuum and condense onto the surface of the substrate, forming a thin uniform film with properties similar to those of the source material [29,30]. Parameters such as temperature, deposition rate, and vacuum are optimized with the aim of making the deposited films uniform and well adherent. Thermal evaporation has been used extensively in device fabrications pertinent to electronics, optoelectronics, and energy applications due to its reliability and reproducibility.

Thermal evaporation fabrication typically involves the following sequential steps [31]:

1. **Preparation of vacuum chamber:** In this step, the vacuum chamber is prepared to hold both the substrate and the evaporation source. The vacuum environment inside the system provides a high-vacuum atmosphere for reduced contamination, inhibition of unwanted chemical reactions, and control of deposition with great precision.

2. **Heating the evaporation source:** The evaporation source material is presented in the forms of pellets, wires, or rods and is heated either by resistive heating or an electron beam. On attaining the adequate temperature, evaporation or sublimation results in the vapor-phase atoms or molecules eventually flowing toward the substrate, where film growth occurs.
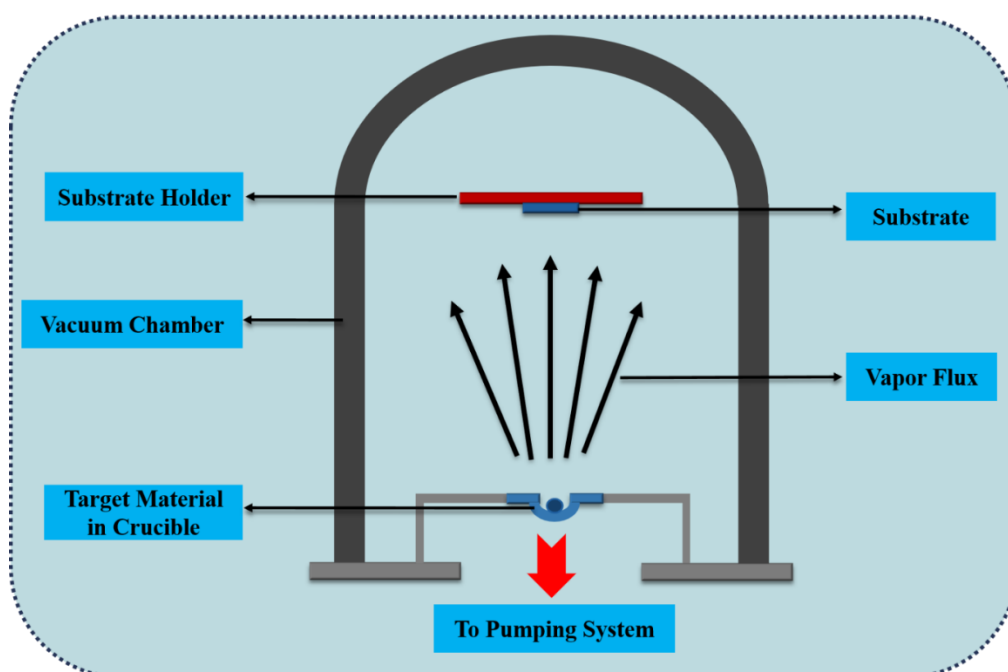
Fig. 2.11: Schematic representation of thermal evaporation system.

3. **Deposition process:** The vaporized atoms or molecules produced from the evaporation source move through the vacuum chamber and arrive at the substrate surface. On impact, the vapor species condense on and stick to the substrate, forming a thin and uniform film. The deposition rate is mostly determined by factors including the temperature of the evaporation source, the distance between source and substrate, and the chamber pressure.

4. **Film growth:** The quality and thickness of the film deposited are dependent on the deposition duration along with other parameters: substrate temperature, vacuum level, and deposition rate. These factors taken together affect the morphology, crystallinity, and uniformity of the film.

In the present work, metal electrodes were deposited on the films synthesized using the EPD technique by employing the thermal evaporation method for facilitating gas sensor fabrication, as presented in Fig. 2.11. The deposition of electrodes was carried out with the help of the Smart Coat 3.0 system (Hind High Vacuum) available at the Computational Functional Materials Research Laboratory (CFMRL), Department of Applied Physics, Delhi Technological University, Delhi, India. The electrical characterization of the fabricated sensors was carried out afterward using the Keithley

Source Measuring Unit (SMU) 2450, located in the Nanomaterials Research Laboratory (NRL), Department of Applied Physics, Delhi Technological University, Delhi, India.

2.4 Gas sensing measurements

The sensing characteristics of the fabricated device were measured using an indigenously developed chemiresistive gas sensing setup available at the Nanomaterials Research Laboratory (NRL), Department of Applied Physics, Delhi Technological University (DTU), as shown in Fig. 2.12. A stainless steel (SS) chamber with an inlet and outlet is used, along with two mass flow controllers (MFCs) for accurate control of gas flow. A source measuring unit (SMU) supplies a constant current to the sensing device during the measurement process.

A rough vacuum is created inside the SS chamber using a rotary pump to remove residual gases at the very beginning of the sensing experiment. Then, dry air is introduced, which establishes the base resistance of the sensor. After that, a controlled mixture of ethanol vapor and dry nitrogen gas is introduced into the chamber. The ethanol gas concentration in ppm was calculated by using equation (2.6):

$$C = \frac{22.4 \times \Psi \times \rho \times V_1}{M \times V_2} \times 1000 \qquad (2.6)$$

In the above formula (equation 2.6), C stands for ethanol concentration (in ppm), Ψ is the gas volume fraction, ρ is the density of ethanol in $kg \cdot m^{-3}$, V_1 is the volume of ethanol in L, M is the molecular weight of ethanol in $kg \cdot mol^{-1}$, and V_2 is the volume of the SS chamber in m^3 [32]. Inside the chamber, the relative humidity (RH) is measured using a digital hygrometer. The resistance change of the sensing films upon gas exposure can be recorded using the LabVIEW-based data acquisition software interfaced with the SMU or independently with a Keithley digital multimeter (DMM7510). All sensor experiments are performed at room temperature, 27 °C, in a controlled atmosphere.
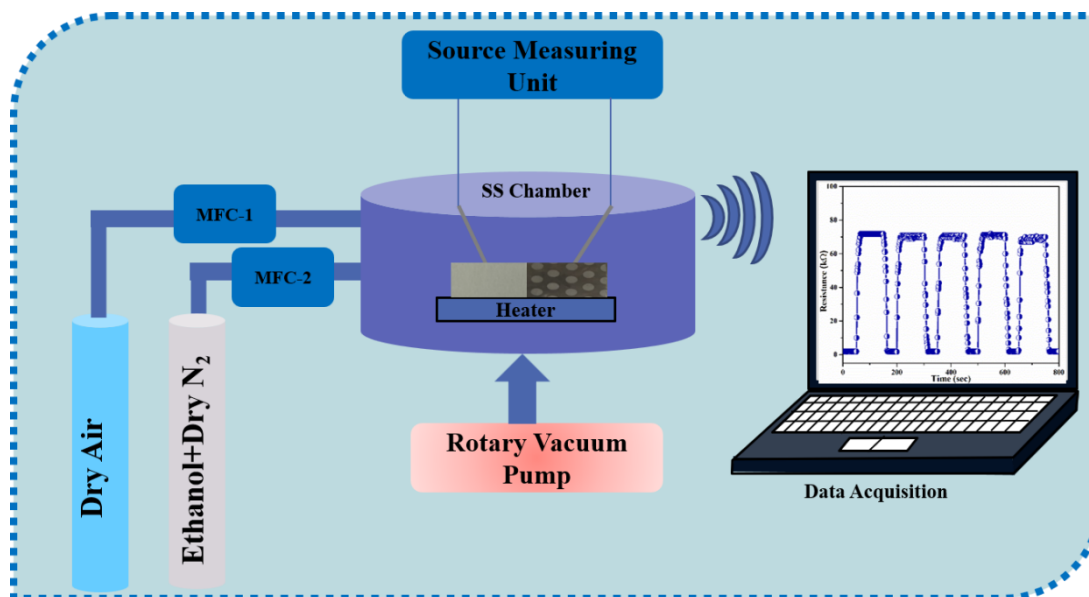
Fig. 2.12: Chemiresistive gas sensing setup.

CHAPTER 3

Highly Selective Sustainable Ethanol Gas Sensor based on p-p heterojunction of SnS/MoSe$_2$ nanocomposite at room temperature
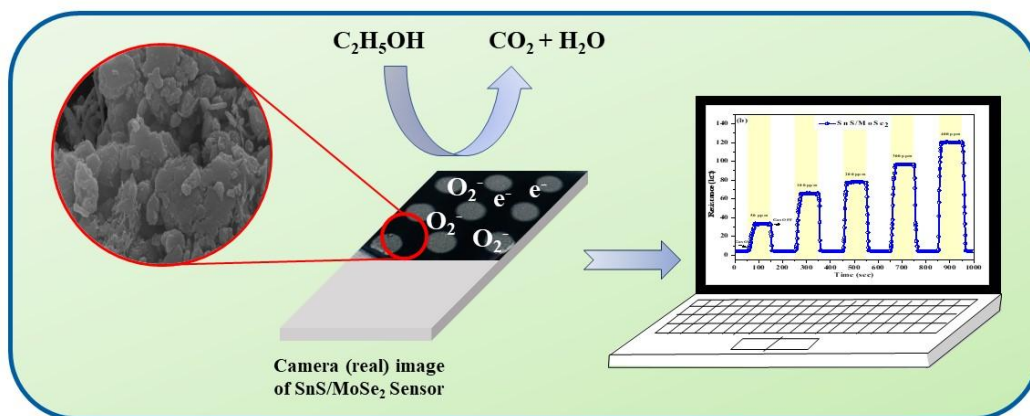
In this chapter, a high-performance chemiresistive ethanol gas sensor operating at room temperature (RT) is demonstrated based on SnS/MoSe$_2$ nanocomposite. The ethanol-sensing capabilities of the pristine-SnS and SnS/MoSe$_2$ nanocomposite sensor are examined by exposing it to various ethanol concentrations ranging from 50-400 ppm at room temperature (RT). The sensing device based on the nanocomposite exhibits a high gas sensing response (R_g/R_a) of 26.8 to 400 ppm for ethanol gas. This results in improved response and recovery times of 9.1 s and 15.7 s respectively, along with high stability, selectivity, and reproducibility. Employing heterojunction in gas-sensing is an effective method for boosting the gas-sensing capabilities of 2D semiconductors. However, selecting semiconductors with compatible energy bands is

equally crucial for optimizing gas sensing performance. The synergy arising from the p-p type heterojunction of SnS nanoplates and MoSe$_2$ nanosheets is observed to enhance the sensor's response to ethanol gas. The sensing mechanism of the SnS/MoSe$_2$ nanocomposite sensor is attributed to the formation of p-p heterojunction, modulation of the potential barrier, and charge carrier transfer. The findings suggest that the SnS/MoSe$_2$-based nanocomposite stands out as a potential candidate for fabricating high-performance ethanol gas sensors for electronic applications in environmental monitoring.

3.1 Introduction

Across the globe, a concerning situation has emerged as a result of environmental pollution originating from widespread industrial operations and the release of waste in various forms of liquids, solids, or smoke (gases)[1, 2]. Volatile organic compounds (VOCs) have been released into the environment due to the expansion of industrialization and socio-economic development. Exposure to most VOCs, not only poses a danger to ecosystems but also significantly harms the planet and human well-being[3, 4]. VOCs can lead to organ failure, and blindness, and also be used as indicators for tracking air quality and monitoring environmental health[5, 6]. Researchers are now paying close attention to the identification of VOCs as early noninvasive illness detection and pollution monitoring have become critical areas of study[7]. Generally, VOCs encompass a wide range of chemical compounds released from liquids and solids, posing health risks when absorbed in higher concentrations[6-10]. Among all VOCs 'ethanol' gas is a colorless, combustible, and volatile compound. This ubiquitous chemical substance has extensive uses in the fields of medicine, chemistry, sanitary and cosmetic manufacturing, automotive fuel, and the food sector[7]. Despite its numerous uses across various sectors, prolonged exposure to it can lead to several illnesses, including nausea, kidney failure, vomiting, headaches, and harm to the central nervous system[10, 11]. Massive research efforts are thus directed towards the creation of sensitive and selective gas detection instruments for the early detection of ethanol at ambient temperature[7]. Scientists have created a variety of sensors for the efficient detection of ethanol, but chemiresistive sensors have attracted the most attention because of their excellent chemical and thermal stability, ease of construction, low cost, and straight forward monitoring methods[12].

Tin sulfide (SnS), a two-dimensional (2D) metal chalcogenide, has garnered substantial attention recently for its multifunctional uses because of its important chemical and physical features[13], SnS is a commonly used p-type material used in solar cells[14], capacitors[15], and other devices, there are just a few reports of this material being employed in sensing applications[16-18]. Naturally occurring Sn vacancies in SnS cause the material to exhibit p-type semiconducting properties[19]. SnS is a better metal chalcogenide for gas sensing applications than PbS, CdS, PbSe, and CdSe because of

its low toxicity, low cost, good stability, and availability[16]. Thus far, there have been reports of some significant studies about sensors relying on SnS to detect gases such as acetone, ethanol, O_2, and NO_2, which opened the door to an in-depth study of this material. Y.T. Ma et al. investigated the ethanol gas sensing capabilities of SnS bound to PVDF at the ppm level. However, the sensor indicated that at a somewhat higher temperature of 240 °C, response and recovery durations were 1.8 seconds (s) and 90 s, respectively[18]. In other work, J.H. Bang et al. used SnS functionalized SnO_2 NWs for NO_2 sensing. The sensor's response time was 69 s to 2 ppm at 100 °C[13]. The sensing ability of SnS nanoplates toward acetone and alcohol gas was reported by M. F. Afsar et al. SnS nanoplates gas-sensing capabilities were investigated in the temperature range of 25-200 °C towards acetone gas. It was found that the sensor exhibits the highest response at 100 °C[17]. From the above reports, It is concluded that the utility of intrinsic SnS-based gas sensors is thus challenged by these investigations, this indicates that gas sensors based on pristine SnS- have slow response and recovery times. From the aforementioned research, it is evident that modifying SnS with different elements offers different approaches for the fabrication of practical gas sensors.

Gas sensors based on 2D-2D heterojunctions offer numerous advantages, leveraging their significant surface-to-volume, active edges with atomic level thickness, and the ability to fine-tune electrical properties. By this motivation, we have selected Molybdenum diselenide ($MoSe_2$), a member of the two-dimensional (2D) transition metal dichalcogenides (TMDs), which has recently garnered significant attention for its notable physical and chemical properties[20, 21]. $MoSe_2$ is an atomically thin material that features a Se-Mo-Se structure, with one atomic layer of molybdenum (Mo) atoms sandwiched between two atomic layers of selenium (Se) atoms, connected by vertical covalent bonds[22]. $MoSe_2$ demonstrated exceptional adsorption/desorption capabilities and features a direct energy band gap, resulting in enhanced electrical conductivity. Additionally, it exhibits a higher adsorption energy with chemical molecules[23, 24]. Zhang et al. also reported that Pd-decorated $MoSe_2$ nanoflowers (NFs) composites, synthesized via a two-step hydrothermal method, exhibit enhanced NH_3-sensing properties at room temperature compared to pristine $MoSe_2$[25]. For instance, Park et al. recently developed highly sensitive gas sensors by decorating

MoSe$_2$ with Pt nanoparticles (NPs). These sensors demonstrated impressive low limits of detection (LODs) at room temperature, with 5 ppm for H$_2$S and 130 ppb for NH$_3$[26]. To effectively enhance the response and recovery time of the current ethanol gas sensors based on 2D nanomaterials, motivates us to investigate the SnS/MoSe$_2$ nanocomposite for ethanol sensing applications.

As far as we know, there are currently no available reports on synthesizing SnS nanoplates with MoSe$_2$ nanosheet-based nanocomposite via the hydrothermal method for chemiresistive detection of ethanol gas at RT. The successful synthesis of as-synthesized nanocomposite is done using a variety of characterization techniques. A simple electrophoretic deposition (EPD) technique is used to fabricate the films of as-synthesized nanocomposite. The sensor, as-fabricated, is exposed to ethanol gas concentrations ranging from 50-400 ppm, and its response has been thoroughly analyzed and studied at RT. A detailed explanation of the synergistic impact of MoSe$_2$ with SnS is provided, and a sensing mechanism is proposed.

3.2   Experimental Procedure

3.2.1   Experimental materials:

The chemicals used in the synthesis were Thiourea (CH$_4$N$_2$S), Tin (II) chloride dihydrate (SnCl$_2$.2H$_2$O), Citric acid (C$_6$H$_8$O$_7$), Ethylene glycol, Sodium Molybdate Dihydrate (Na$_2$MoO$_4$.2H$_2$O), Hydrazine Hydrate-86% (N$_2$H$_4$.H$_2$O), Selenium (Se) powder and Ethanol (C$_2$H$_5$OH). These chemicals were purchased from Sigma Aldrich.

3.2.2   Synthesis of SnS/MoSe$_2$ nanocomposite:

The SnS/MoSe$_2$ nanocomposite was synthesized using a simple hydrothermal process. In the first step, SnS nanoplates synthesis was done by dissolving 1.49 mmol of CH$_4$N$_2$S and 1.01 mmol of SnCl$_2$.2H$_2$O in 30 ml of ethylene glycol under continuous magnetic stirring. Following this, 1.09 mmol of citric acid was added and stirred for another 30 min to ensure complete mixing. The prepared solution was then put into a 100 ml Teflon-lined stainless steel autoclave and kept at 180 °C for 24 h in a hot air oven. The reactor was then naturally cooled to RT. To obtain SnS powder, the black product was

finally centrifuged multiple times with deionized (DI) water and ethanol before being dried for 24 h at 80 °C.

In the second step, MoSe$_2$ nanosheets were prepared by adding 2 mmol of Na$_2$MoO$_4$.2H$_2$O in DI water and ethanol (1:1 by volume) with stirring for 45 min until a clear solution was obtained. In the meantime, a solution containing 4 mmol of selenium powder was dissolved in 10 mL of N$_2$H$_4$.H$_2$O under continuous stirring. Subsequently, selenium solution was added to sodium molybdate dehydrate solution dropwise while being continuously stirred for another 45 min. After that, the resulting mixture was transferred to a 50 mL hydrothermal autoclave and heated to 220 °C for 24 h in a hot air oven. The black powder was obtained after multiple washings with DI and ethanol and then dried overnight at 100 °C.

Finally, for the synthesis of SnS/MoSe$_2$ nanocomposite, a stoichiometric amount of as obtained SnS and MoSe$_2$ powder, was dispersed in ethanol and sonicated for 2 h. The resulting dispersion was transferred to a 100 ml Teflon-lined stainless-steel autoclave and kept at 160 °C for 24 h in a hot air oven. The black-colored powder was obtained through multiple washes of the final product with DI and ethanol, followed by drying in a hot air oven for 12 h.

3.2.3   Structural Design and Fabrication of Ethanol Gas Sensor

The following steps were employed for the fabrication of the SnS/MoSe$_2$ nanocomposite gas sensor: Initially, as-synthesized powder was dispersed in acetonitrile at a concentration of 1.25 mg/ml, followed by 2.5 h ultrasonication. In the meantime, the pre-hydrolyzed glass slides coated with ITO were cleaned using isopropyl alcohol (IPA) and DI water several times. Following the cleaning process, the slides were subjected to drying at 60° C in an oven for 30 min. Subsequently, the solution was transferred to a two-electrode EPD cell, comprising the counter electrode (CE) and the working electrode (WE) as depicted in Fig 3.1. To obtain a fine film of the SnS/MoSe$_2$ nanocomposite, an optimum constant potential was applied for 180 s after attaching the ITO to WE. Finally, the thermal evaporation technique was utilized to deposit silver electrodes onto the prepared film. A similar procedure was used to

fabricate pristine-SnS film. This fabricated film was employed to conduct different sensing measurements.
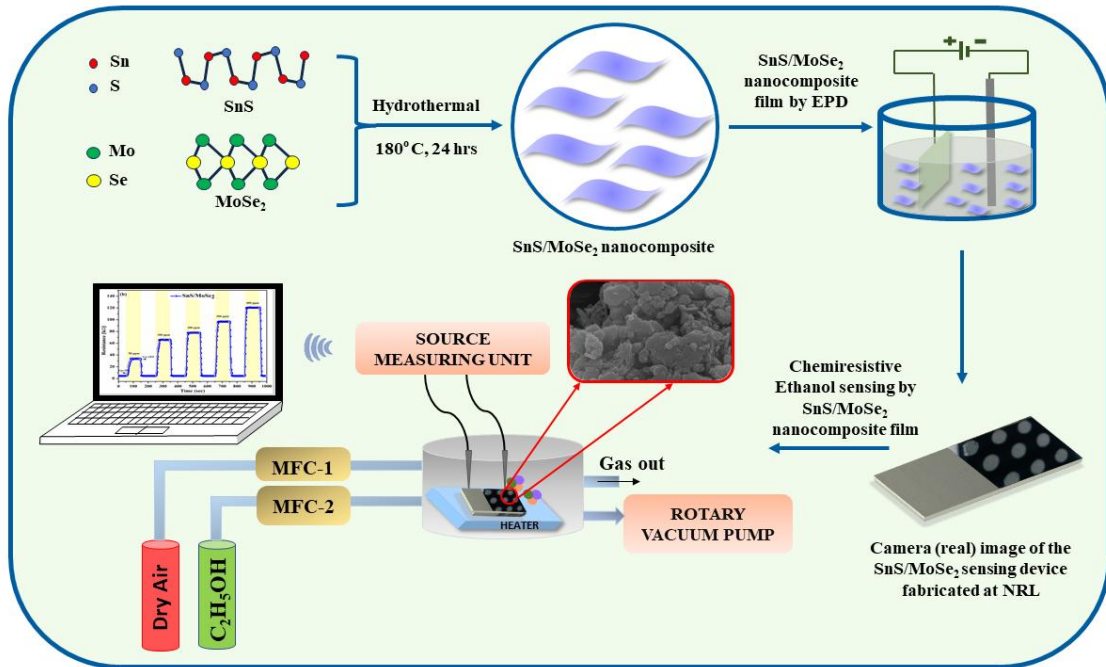
Fig. 3.1: Schematic illustration depicting the fabrication process of the SnS/MoSe$_2$ nanocomposite-based sensor for ethanol gas detection.

The gas sensing was carried out in a customized stainless steel (SS) chamber. A gas mixture containing 1% ethanol balanced with nitrogen (N$_2$) gas was used for the detection of ethanol gas. Two gas mass flow controllers (MFC) were attached to the chamber, one MFC regulated the flow of the target gas analyte (1% ethanol), and the second MFC was used to control the dry air inside the chamber. A rotary pump was used to create rough vacuum pressure in the SS chamber. A constant current supply to the SnS/MoSe$_2$ nanocomposite sensor was provided by SMU (source measuring unit). Next, in order to get the baseline resistance, dry air was introduced for 50 s. Thereafter, a mixture comprising 1% ethanol and N$_2$ was introduced into the SS chamber for a duration of 100 s, with varying concentrations ranging from 50-400 ppm at RT. The concentration of ethanol gas within the SS chamber was determined in parts per million (ppm) using the formula provided below (3.1):

$$C = \frac{22.4 \times \Psi \times \rho \times V_1}{M \times V_2} \times 1000 \tag{3.1}$$

In the aforementioned formula (eqn.1), the ethanol gas concentration is depicted by C (ppm), gas volume fraction is denoted by Ψ, the density of ethanol is represented by ρ ($kg.m^{-3}$), the molecular weight of ethanol is expressed as M ($kg.mol^{-1}$), the volume of ethanol gas is indicated as V_1 (L), and the volume of the SS chamber is denoted as V_2 (m^3)[27, 28]. A data acquisition software (Lab-View) attached to the SMU was used to record the change in resistance of the sensing films.

3.3   Results and Discussion

3.3.1   Structural analysis using XRD

X-ray diffraction (XRD) analysis was employed to investigate the crystallographic information of the as-prepared samples, namely pristine-SnS, pristine-$MoSe_2$, and the SnS/$MoSe_2$ nanocomposite (Fig. 3.2). The XRD analysis of pristine-SnS nanoplates revealed distinct peaks observed at 2θ values of 21.9°, 26.1°, 27.4°, 30.5°, 31.6°, 32.1°, 39.1°, 42.7°, 44.8°, 51.2°, 52.9°, 54.2°, 56.6°, 64.29°, and 66.48°. These peaks correspond well to the crystallographic planes (110), (120), (021), (101), (111), (040), (131), (102), (411), (020), (112), (511), (221), (601), (420), (512), and (711) of the orthorhombic phase of SnS (JCPDS 39-0354)[29]. The diffraction peaks of the pristine-$MoSe_2$ sample occur at 2θ angles of 13.5°, 31.6°, 37.6°, and 55.9°, corresponding to crystallographic planes (002), (100), (103), and (110) of the hexagonal phase of $MoSe_2$ (JCPDS 029-0914)[30].

The diffractogram of the SnS/$MoSe_2$ nanocomposite displays peaks attributed to planes (002), (103), and (110) indicative of $MoSe_2$ (represented by +), whereas other peaks are corresponding to planes of SnS (represented by *), signifying effective interaction between SnS nanoplates and $MoSe_2$ nanosheets. The (100) plane of $MoSe_2$ remains invisible due to the notably higher intensity of SnS diffraction peaks[31]. Furthermore, a reduction in the intensity of diffraction peaks is observed for both SnS and $MoSe_2$ within the SnS/$MoSe_2$ nanocomposite, providing additional evidence of composite formation[32].
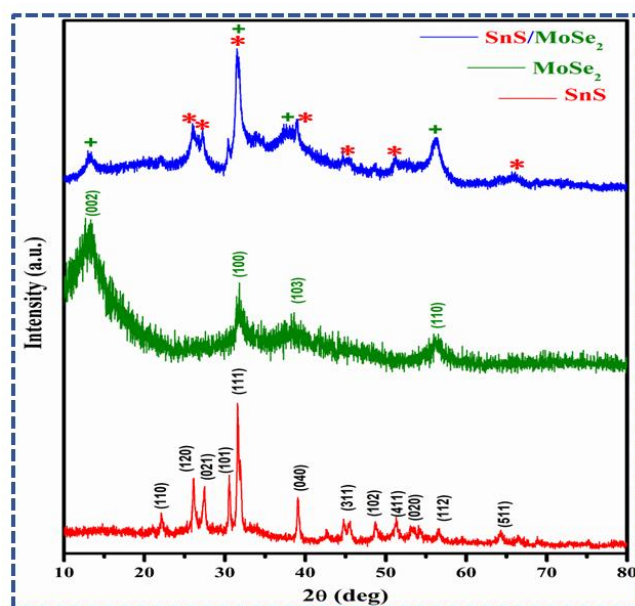
Fig. 3.2: XRD pattern of pristine-SnS, pristine-MoSe₂, and SnS/MoSe₂ nanocomposite.

3.3.2 Analyzing vibrational modes using Raman spectroscopy

Fig. 3.3 represents Raman spectra analysis of pristine-SnS, pristine-MoSe₂, and SnS/MoSe₂ nanocomposite, obtained using an excitation wavelength of 532 nm. The Raman spectra of as-synthesized SnS nanoplates reveal three distinct peaks located at 99 cm^{-1}, 224 cm^{-1}, and 307 cm^{-1}. The peaks at 99 cm^{-1} and 224 cm^{-1} correspond to the characteristic A_g mode of SnS, arising from the interatomic vibrations between the metal (Sn) and chalcogen (S)[33]. The peak observed at 307 cm^{-1} is attributed to the presence of a secondary phase, namely tin sulfide (Sn_2S_3), as an impurity. This peak is likely to originate from the intralayer vibration of the chalcogen-chalcogen atom[34]. Whereas, the Raman spectra of MoSe₂ show a prominent out-of-plane A_{1g} mode at 238 cm^{-1}, serving as its characteristic peak[35]. Additionally, the other two in-plane modes, E_{1g} and E^1_{2g}, are observed at 167 cm^{-1} and 283 cm^{-1}, respectively, aligning well with previous studies[36]. In the SnS/MoSe₂ nanocomposite, the distinct peaks associated with both SnS and MoSe₂ are evident, showing a slight alteration in intensities compared to their pristine counterparts. These intensity changes are indicative of synergistic effects resulting from interactions between SnS and MoSe₂ during the hydrothermal synthesis process[37]. Thus, as validated by XRD and HRTEM analyses, the Raman spectrum of SnS/MoSe₂ nanocomposite confirms the successful synthesis.
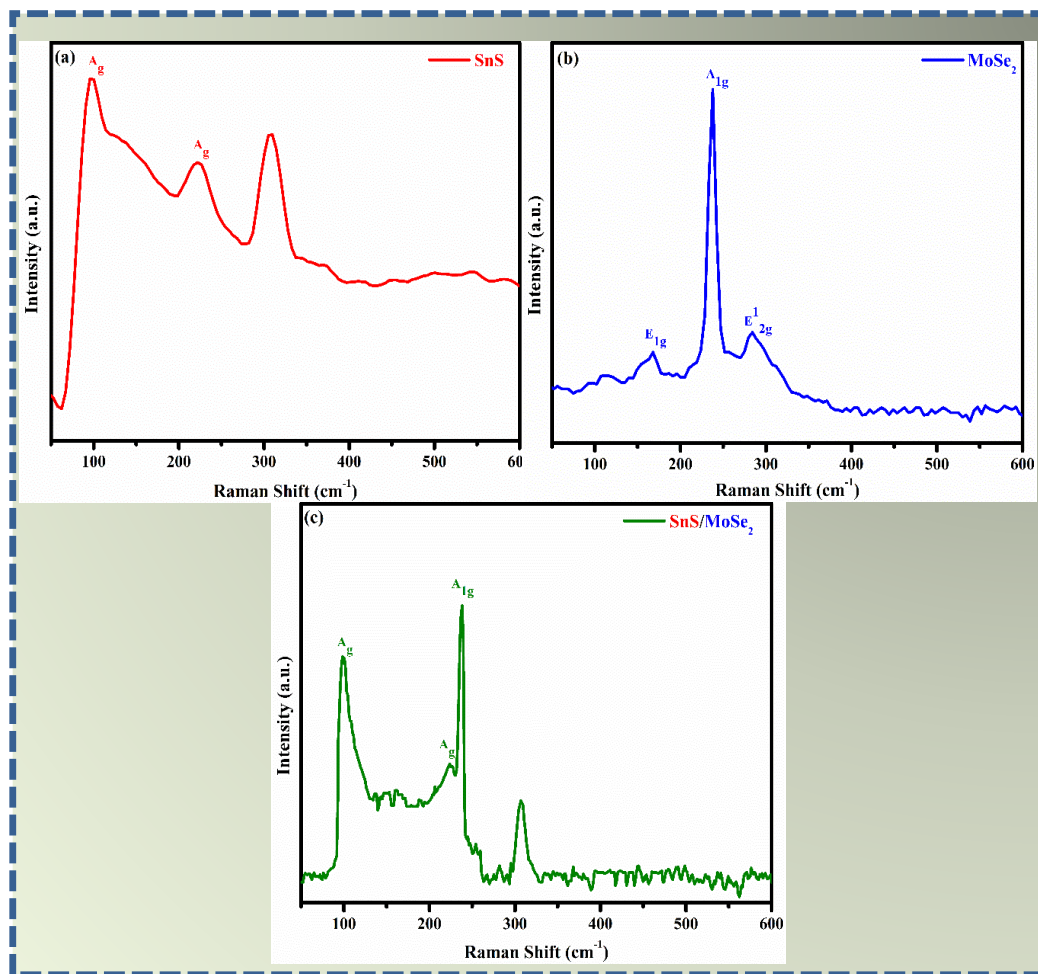
Fig. 3.3: Raman spectrum of (a) pristine-SnS (b) pristine-MoSe$_2$, and (c) SnS/MoSe$_2$ nanocomposite.

3.3.3   Morphological studies using HRTEM and FESEM

HRTEM measurements were utilized to analyze the morphology and microstructure of the as-fabricated samples. The images acquired for the three samples pristine-SnS, pristine-MoSe$_2$, and SnS/MoSe$_2$ nanocomposite are illustrated in Fig. 4. Fig. 3.4(a) illustrates a typical HRTEM image of pristine-SnS nanoplates, revealing a large surface area of SnS nanoplates[38]. Fig. 3.4(b) displays an HRTEM image of pristine-MoSe$_2$ nanosheets, whereas Fig. 3.4(c,d) provides evidence of the modification of the SnS nanoplates by MoSe$_2$ nanosheets, demonstrating the successful incorporation of MoSe$_2$ nanosheets with SnS nanoplates. The spacing between adjacent lattice fringes measures 0.28 nm, corresponding to the SnS (111) plane, and 0.21 nm corresponding to MoSe$_2$ (103) plane. The SnS/MoSe$_2$ nanocomposite exhibits a distinct heterogeneous interface

between SnS nanoplates and MoSe$_2$ nanosheets, clearly visible at scale bars of 5 nm. Therefore, based on the HRTEM analysis, it is evident that MoSe$_2$ nanosheets have been successfully incorporated with SnS nanoplates, which aligns with the findings from the XRD analysis[18, 28, 39, 40].
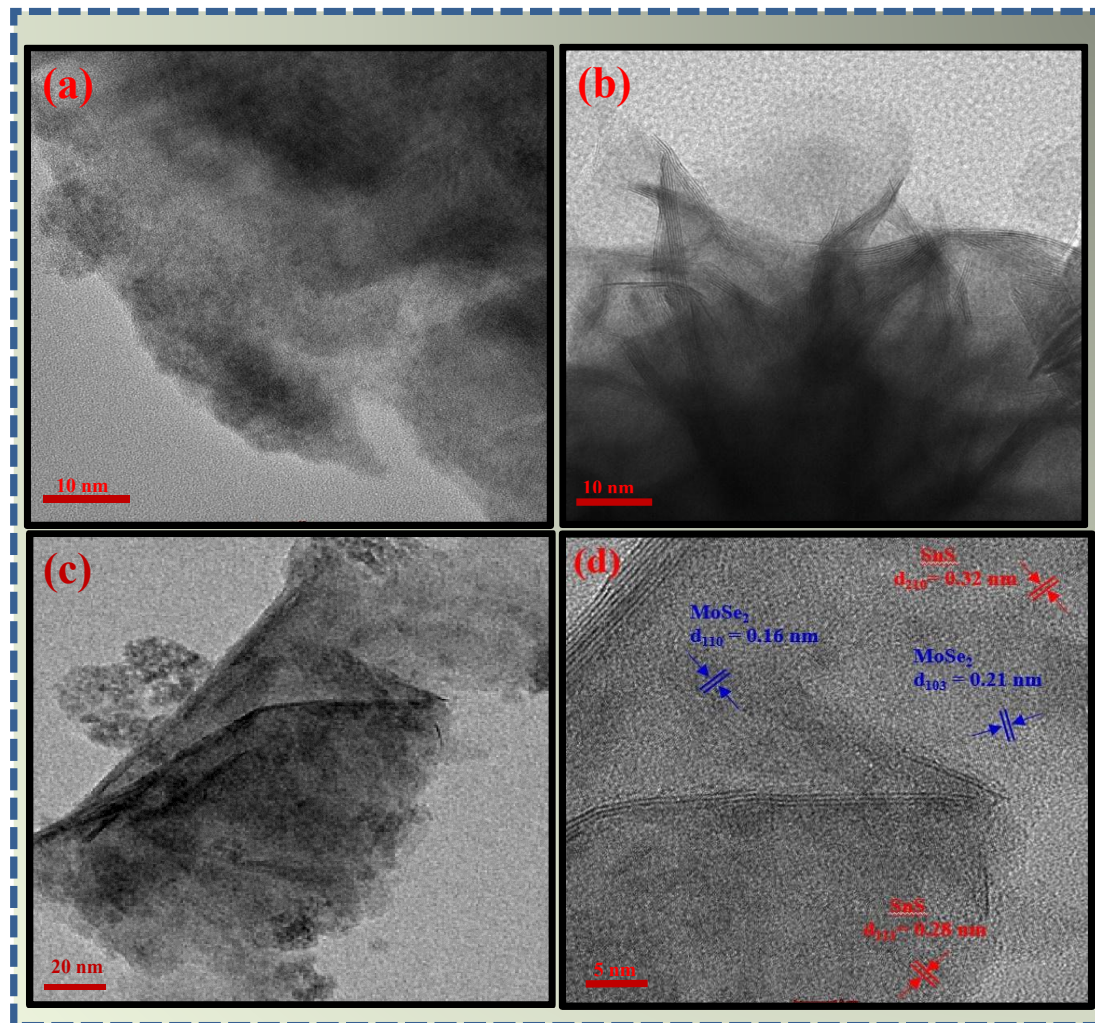
Fig. 3.4: HRTEM images of (a) pristine-SnS, (b) pristine-MoSe$_2$, (c) SnS/MoSe$_2$ nanocomposite, and (d) Lattice fringes of SnS nanoplates and MoSe$_2$ nanosheets with measured interplanar spacing.

The morphology and microstructure of the as-synthesized samples were further analyzed through FESEM measurements. In Fig. 3.5, the acquired images of the (a) pristine-SnS, (b) pristine MoSe$_2$, and (c,d) SnS/MoSe$_2$ nanocomposite are depicted. Pristine-SnS exhibits plate-like morphologies, with nanoplates randomly grown and demonstrating clean, smooth surfaces [41]. Whereas, in the case of pristine-MoSe$_2$, a

continuous sheet network is evident which potentially enhances the gas-sensing performance of the sensor[42]. The magnified view of SnS/MoSe$_2$ nanocomposite displays the interaction of MoSe$_2$ nanosheets with SnS nanoplates, as shown in Fig. 3.5 (c,d). These images suggest potential synergistic interactions between the constituent materials, also evident from HRTEM images.
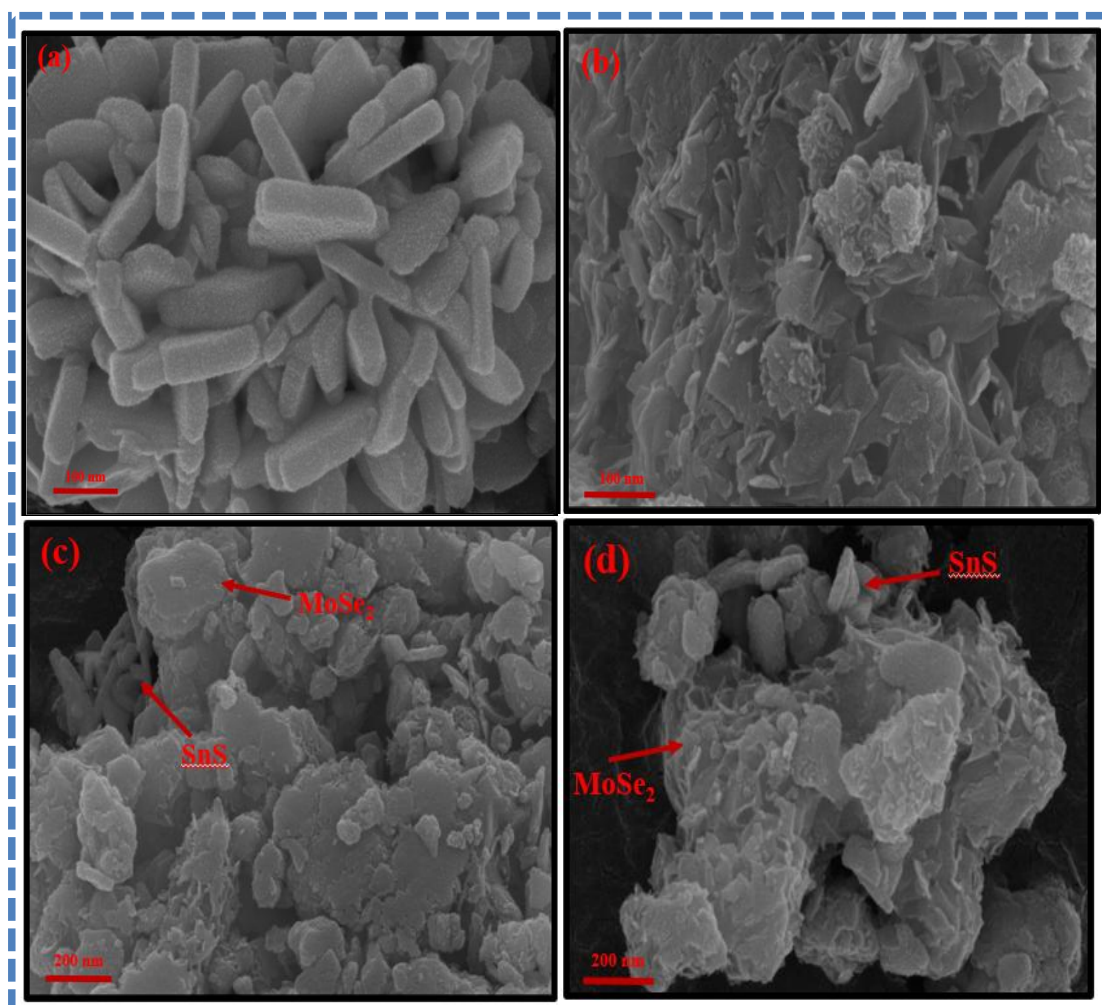
Fig. 3.5: FESEM images of (a) pristine-SnS nanoplates, (b) pristine-MoSe$_2$ nanosheets, and (c,d) SnS/MoSe$_2$ nanocomposite.

3.3.4 BET analysis of the synthesized samples

A BET analysis was performed to find the surface area of both SnS nanoplates and SnS/MoSe$_2$ nanocomposite. The N$_2$ absorption-desorption isotherm as depicted in Fig. 3.6 closely resembles a Type IV curve, featuring a noticeable hysteresis loop within the relative pressure range of 0.8-1.0, indicating the presence of a mesoporous

structure[43]. The BET-specific surface area, calculated from N_2 isotherms, was 8.23 m^2g^{-1} for the SnS nanoplates. For the SnS/MoSe$_2$ nanocomposite, the area measured was 12.32 m^2g^{-1}, demonstrating a 50 % increase in surface area compared to pristine-SnS.
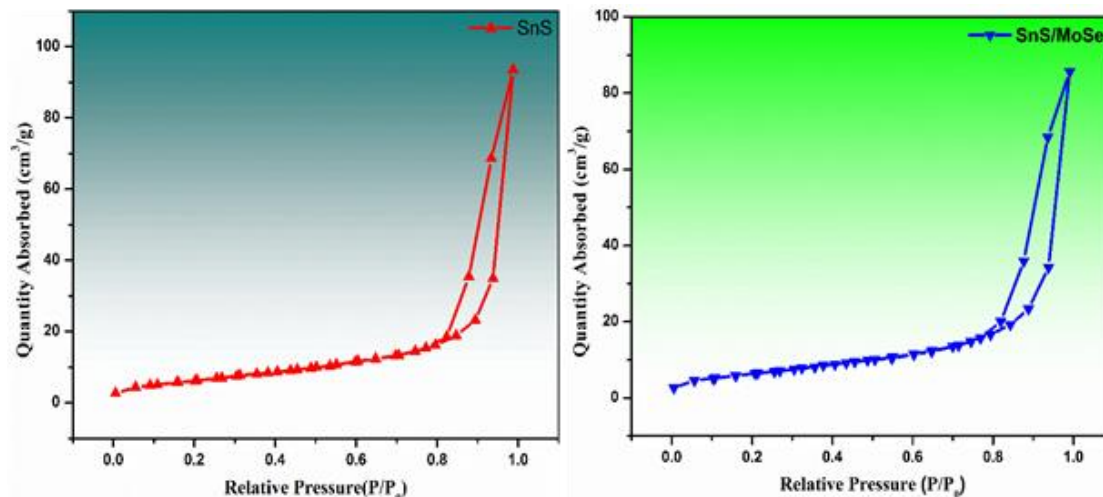
Fig. 3.6: The N_2 absorption–desorption isotherms of SnS nanoplates and SnS/MoSe$_2$ nanocomposite.

The higher specific surface area of the SnS/MoSe$_2$ nanocomposite could provide more efficient active sites compared to pristine-SnS, resulting in enhanced performance of the SnS/MoSe$_2$ nanocomposite sensor[44].

3.4   Sensing performance of the fabricated sensor

In order to compare the sensing capabilities, it is crucial to examine the sensing properties SnS/MoSe$_2$ nanocomposite gas sensor concurrently with that of the pristine-SnS gas sensor. The resistance curves of pristine SnS and SnS/MoSe$_2$ nanocomposite gas sensors to varied ethanol gas concentrations at RT in dry air are shown in Fig. 3.7 (a) and 3.7(b) respectively. From the RT curves, we deduce that the sensor exhibits p-type sensing behavior since ethanol is a reducing gas and when the sensor is exposed to it, the resistance increases. The resistance of pristine-SnS varies slightly when exposed to varying concentrations of ethanol gas, as shown in Fig. 3.7 (a). On the other hand in Fig. 3.7 (b), the SnS/MoSe$_2$ nanocomposite sensor responded to the same concentrations of ethanol gas significantly more. Here, it can be observed that by combining SnS nanoplates with MoSe$_2$ nanosheets, the sensor's sensitivity is raised,

enabling it to detect even low concentrations of ethanol (50 ppm). Furthermore, both sensors exhibited markedly increased resistance when exposed to higher concentrations of ethanol. Fig. 3.7 (a) and 3.7 (b) outline three parameters characterizing the sensor properties: sensing response (R_a/R_g), recovery time (t_{rec}), and response time (t_{resp}). First, we observe that when the SnS/MoSe$_2$ nanocomposite sensor is exposed to 400 ppm of ethanol, its resistance increases to $R_g = 120.1$ kΩ from its base resistance $R_a = 4.4$ kΩ in dry air. Where resistance values in the presence of ethanol gas mixture and dry air are denoted by R_g and R_a, respectively. The response value is calculated to be 26.8 at 400 ppm ethanol gas. Moreover, both the pristine-SnS and SnS/MoSe$_2$ nanocomposite sensor shows complete recovery to the same base resistance. This demonstrates the reversible interaction caused by the physisorption process between the ethanol gas and the as-fabricated sensors.
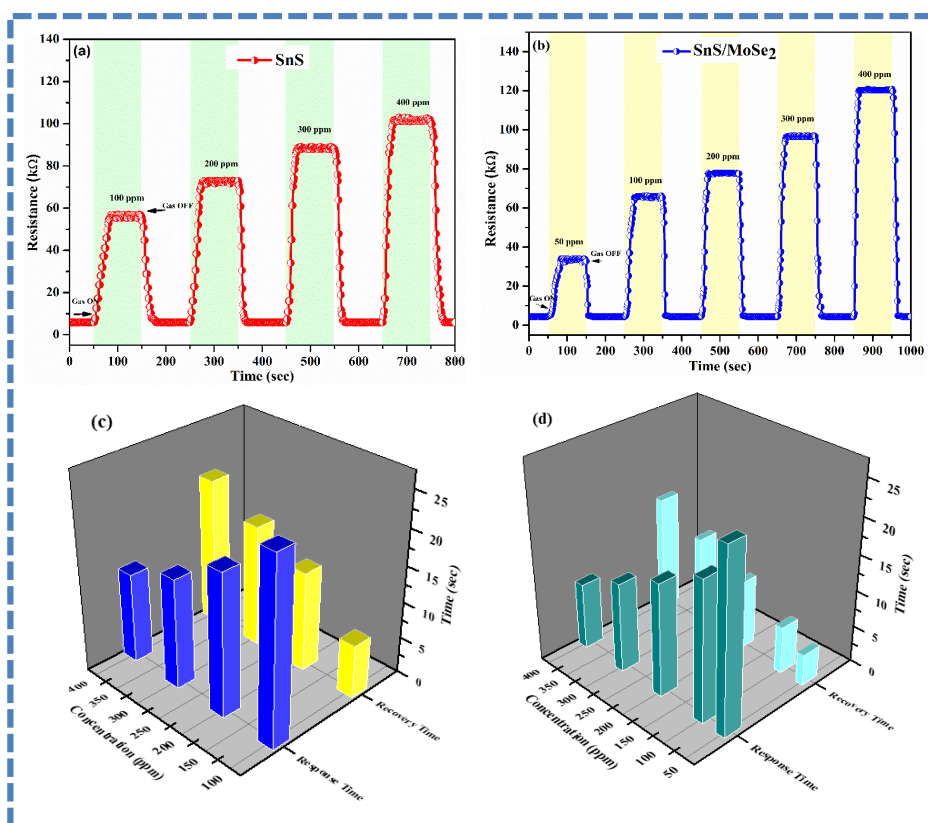
Fig. 3.7: (a) and (b) represent the response of the pristine-SnS and SnS/MoSe$_2$ nanocomposite sensor whereas (c) and (d) represent t_{resp} and t_{rec} characteristics of both the sensors respectively towards various concentrations of ethanol gas at RT.

The response times (t_{resp}) of pristine-SnS and SnS/MoSe$_2$ sensors to varying ethanol gas concentrations are shown in Fig 3.7 (c) and 3.7 (d) respectively. The response time of the

SnS/MoSe$_2$ sensor is less than that of the pristine-SnS sensor for all ethanol gas concentrations. The same pattern is noted for recovery time (t_{rec}), the SnS/MoSe$_2$ sensor recovers faster than the pristine-SnS sensor. The calculated values of response and recovery times are 12.4 s and 20.3 s for the pristine-SnS sensor whereas MoSe$_2$/SnS is found to be 9.1 s and 15.7 s respectively for 400 ppm ethanol gas. As the concentration of ethanol gas rises from 50 to 400 ppm, it is found that the t_{rec} increases and the t_{resp} decreases. Large sites for gas adsorption are present on the sensor's surface could be the reason for the drop in t_{resp}. The increase in t_{rec} could potentially be attributed to the physisorption of ethanol molecules and their reaction products on the sensor's surface, which required some time to desorb[35]. As a result, the SnS/MoSe$_2$ nanocomposite sensor responds more quickly than the pristine-SnS sensor.

As shown in Fig. 3.8(a) and 3.8(b), the SnS/MoSe$_2$ nanocomposite sensor underwent four consecutive cycles of exposure to ethanol gas at concentrations of 50 ppm and 400 ppm to demonstrate its repeatability. The results suggest that almost the same response was shown by the nanocomposite sensor in every cycle. This demonstrates the SnS/MoSe$_2$ nanocomposite sensor's good repeatability, which is crucial for practical applications.
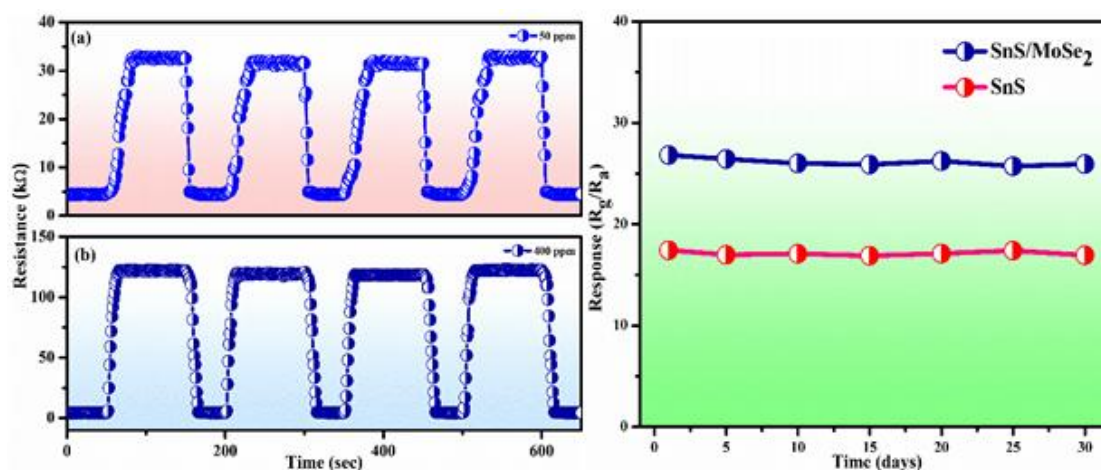
Fig. 3.8: (a) and (b) Repeatability towards 50 ppm and 400 ppm of the SnS/MoSe$_2$ gas sensor and (c) long-term stability (30 days) of the SnS/MoSe$_2$ nanocomposite and pristine-SnS sensor to 400 ppm ethanol at RT.

It is well-known that while considering the practical application of gas sensors, long-term response stability is an essential component. Therefore, the sensor is tested at RT with ethanol gas concentrations of 50 and 400 ppm, on a four-day cycle, and the results obtained are shown in Fig 3.8 (c). It is observed that the SnS/MoSe$_2$ nanocomposite sensor maintained nearly the same ethanol response over a 30-day period.
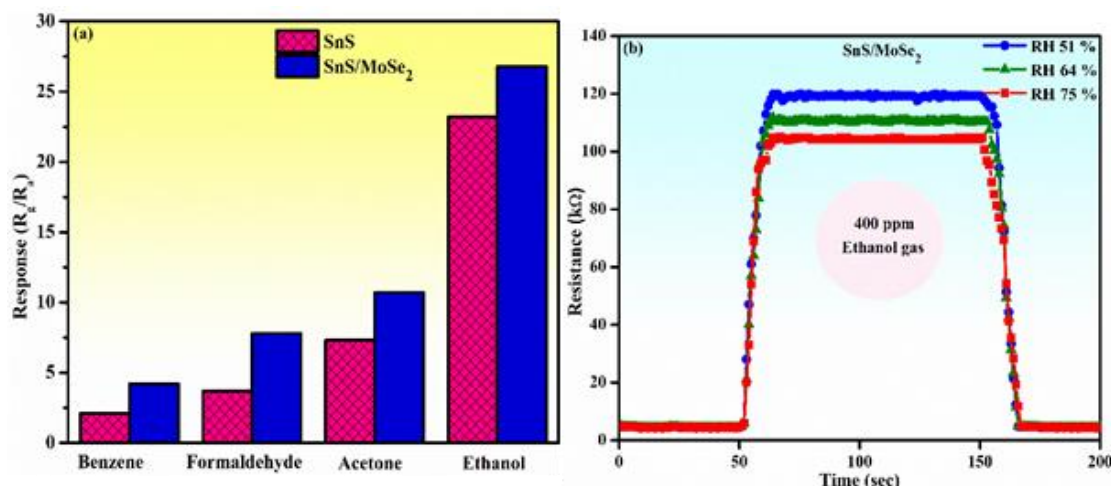
Fig. 3.9: (a) The histogram showing the selectivity of pristine-SnS and SnS/MoSe$_2$ nanocomposite sensor to a few VOCs at 400 ppm at RT and (b) Effect of RH on the response of the SnS/MoSe$_2$ sensor to 400 ppm of ethanol gas at RT.

To gain insight into the SnS/MoSe$_2$ sensor's selectivity, a change in the device's resistance at RT was observed when it was exposed to different VOCs. The sensor's response towards various VOCs such as benzene, formaldehyde, acetone, and ethanol were found to be 3.5, 7.8, 10.7, and 26.8 respectively (Fig. 3.9(a)). As compared to these tested VOCs, the gas response value toward ethanol was nearly 7.6, 3.4, and 2.5 times higher respectively, indicating that the as-fabricated sensors have an effective response and good selectivity to ethanol.

Fig 3.9 (b) illustrates the influence of humidity on the SnS/MoSe$_2$ sensor's performance. As anticipated, an increase in relative humidity (RH) leads to a decrease in the sensor's response. At relative humidity levels of 51%, 64%, and 75%, the corresponding responses were 26.5, 25.2, and 23.7, respectively. The decrease in sensor response due to higher humidity levels is attributed to a reduction in available adsorption sites, as

these sites become occupied by water vapor. Consequently, fewer target gas molecules are adsorbed onto the sensing layer, resulting in a reduced sensor response.

Table 3.1 compares our work with previous studies regarding ethanol-sensing properties, focussing on the working temperature, response time, and recovery time. The comparison findings show that the as-fabricated SnS/MoSe₂ nanocomposite sensor operates at RT and has superior response and recovery times. Consequently, compared to other nanocomposite sensors, the SnS/MoSe₂ sensor exhibits superior sensing properties, suggesting its potential as an excellent choice for detecting ethanol gas.

Table 3.1: Comparing the performance metrics of this study with those of prior research in the realm of ethanol gas sensing.

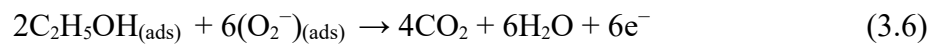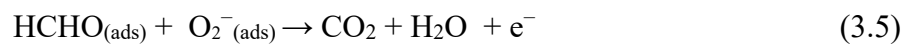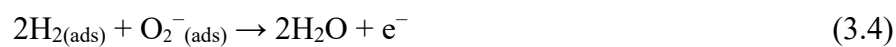| Sensor Materials	Concentration (ppm)	Sensor Response (S)	Operating Temperature (°C)	Response Time(sec)	Recovery Time(sec)	Refs.
MoS_2/TiO_2	300	500	100#	70 ± 10	90 ± 20	[5]
$MoSe_2$	500	RT	4.5*	11	18	[12]
SnS	200	10	130#	2	9	[16]
SnS	300	300	13#	29	21	[17]
SnS/PVDF	240	100	92.96#	1.8	90	[18]
Ag-doped $MoSe_2$	RT	1	1.34#	NA	NA	[21]
MoS_2/CeO_2	RT	50	7.78$	7	5	[45]
$In_2O_3/ZnO/Ti_3C_2T_X$	25	10	2.15$	85	112	[46]
PbS/SnS_2	RT	60	45.64#	104	84	[47]
$SnS/MoSe_2$	RT	400	26.8*	9.1	15.7	This work

* indicates that $S = R_g/R_a$; # indicates that $S = (R_g-R_a/R_a) \times 100$; $ indicates that $S = R_a/R_g$

3.5   Gas sensing mechanism

The analysis of the R-T response curves indicates that the pristine-SnS nanoplates and the SnS/MoSe₂ nanocomposite sensor exhibit a p-type character towards ethanol gas at RT (Fig. 3.7(a) and 3.7(b)). From the literature, it is well known that, the SnS nanoplates offered abundant surface sites, defects, and sulfur vacancies conducive to the adsorption of oxygen molecules on its surface. These oxygen molecules turn into oxygen ion species (O_2^-) by capturing electrons from the surface of the SnS nanoplates sensor as

shown in eqn. 3.2[17, 48]. These oxygen ion species create an accumulation layer near the surface of SnS nanoplates. This leads to the resistance of the SnS decreasing, reaching a constant value when saturation is achieved. Under exposure to ethanol gas, it not only reacts with oxygen ion species (O_2^-) present on the surface of SnS nanoplates but also donates electrons to SnS nanoplates. Therefore, the O_2^- species predominantly contributed to the sensing behavior as follows:

$$O_{2(gas)} + e^- \rightarrow (O_2^-)_{ads} \tag{3.2}$$

$$2CO_{(ads)} + O_2^-{}_{(ads)} \rightarrow 2CO_2 + e^- \tag{3.3}$$

$$2H_{2(ads)} + O_2^-{}_{(ads)} \rightarrow 2H_2O + e^- \tag{3.4}$$

$$HCHO_{(ads)} + O_2^-{}_{(ads)} \rightarrow CO_2 + H_2O + e^- \tag{3.5}$$

$$2C_2H_5OH_{(ads)} + 6(O_2^-)_{(ads)} \rightarrow 4CO_2 + 6H_2O + 6e^- \tag{3.6}$$

When reductive ethanol gas is introduced, it reacts with the adsorbed oxygen species on the sensing material, generating CO_2 and H_2O, and releasing electrons back into the sensing material[9, 46, 49]. The overall majority charge carrier concentration decreased thereby increasing the resistance of the SnS sensor. Fig. 3.10 displays the schematic of the gas sensing mechanism of the SnS/MoSe$_2$ nanocomposite sensor with the help of an energy band diagram. The enhanced sensing performance observed in SnS/MoSe$_2$ nanocomposite is likely due to two factors resulting from the formation of p-p heterojunction[48]. Firstly, the reported band gap of SnS and MoSe$_2$ p-type in literature are 1.68 eV and 1.3 eV respectively[30, 39]. The work function of p-type SnS and MoSe$_2$ are reported as 4.89 eV[50] and > 4.65 eV[47]. The disparity in the work function between SnS nanoplates and MoSe$_2$ nanosheets induces electron migration from MoSe$_2$ to SnS, while holes diffuse from SnS to MoSe$_2$ until an aligned fermi level is formed[50]. Fig. 3.10 illustrates the bending of the energy band at the SnS/MoSe$_2$ interface. This leads to the formation of an accumulation layer at the SnS/MoSe$_2$ interface, where electrons accumulate on the SnS side and holes accumulate on the MoSe$_2$ side. When exposed to ethanol gas, partial ethanol molecules were adsorbed on the surface of SnS/MoSe$_2$ nanocomposite while some of the molecules reacts with the oxygen ion species (O_2^-) adsorbed on the surface of the nanocomposite. The adsorbed ethanol molecules donate electrons to the SnS/MoSe$_2$ nanocomposite, which recombine

with the majority of charge carriers (holes) present there. The decrease in the majority charge carriers widens the height of the potential barrier, thereby decreasing the conductivity of the nanocomposite[51]. Finally, the resistance of the nanocomposite sensor increases as demonstrated in Fig. 3.7(b).
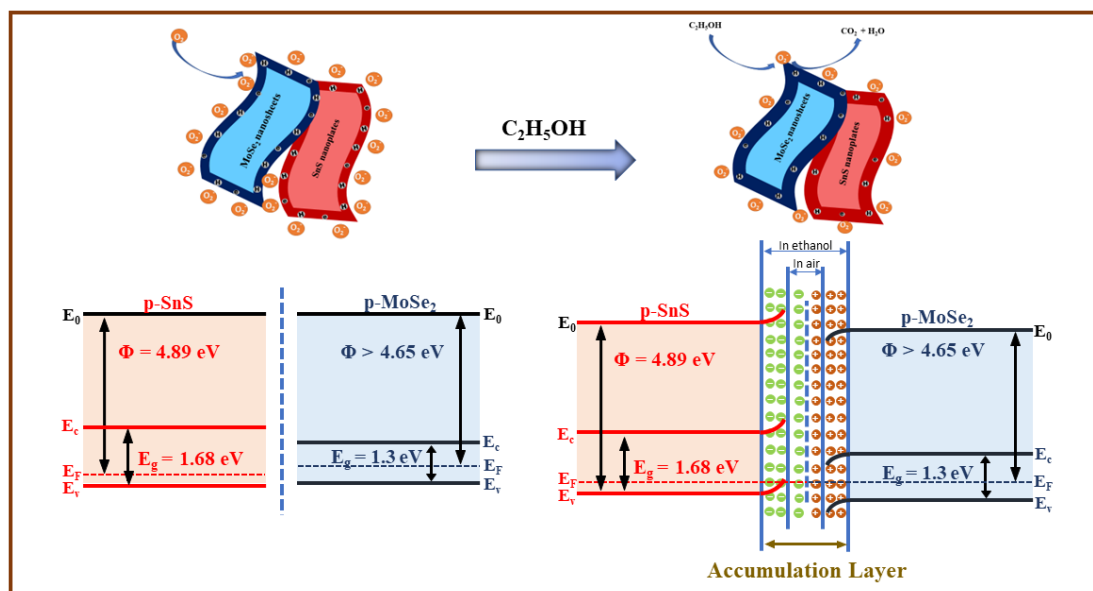
Fig. 3.10: Schematic representation of ethanol gas sensing mechanism of the SnS/MoSe$_2$ nanocomposite sensor before and after exposure to an ethanol atmosphere.

Secondly, the formation of multiple heterojunctions between the SnS/MoSe$_2$ nanocomposite sensor led to the adsorption of multiple ethanol molecules and affects charge transfer in the sensing process[18]. Under exposure to ethanol gas, they absorb preferentially at the SnS/MoSe$_2$ nanocomposite sensor's interface. This can be attributed to multiple heterojunctions, which serve as highly active sites (such as sulfur defects and vacancies), facilitating gas adsorption. The increase in adsorption sites on the SnS/MoSe$_2$ nanocomposite is supported by surface area analysis conducted through BET measurements. Specifically, the calculated surface area of pristine-SnS and SnS/MoSe$_2$ nanocomposite is 8.23 m^2g^{-1} and 12.32 m^2g^{-1} respectively. This indicates a significant increase in the surface area of the SnS/MoSe$_2$ nanocomposite compared to pristine-SnS which enhanced the sensing parameters of the nanocomposite sensor. Moreover, the gas-sensing process is greatly impacted by the value of the lowest unoccupied molecular orbital (LUMO). According to reports, benzene, formaldehyde, acetone, and ethanol have LUMO energy values of 0.42 eV, 0.22 eV, 0.21 eV, and 0.13

eV, respectively[52, 53]. Due to the lowest LUMO energy of ethanol gas, which facilitates the transmission of electrons between the nanocomposites and ethanol gas molecules, the sensor exhibits the best selectivity for detecting ethanol gas.

Hence, we deduce that the formation of p-p heterojunction at the interface of SnS and MoSe$_2$ enhanced the performance of the sensor[54]. The increased surface area of the nanocomposite sensor provided active sites for the adsorption of multiple ethanol molecules, thereby positively affecting sensitivity performance.

3.6   Conclusion

In summary, we demonstrated the fabrication of a nanocomposite sensor comprising SnS nanoplates and MoSe$_2$ nanosheets through a facile and cost-effective hydrothermal method. We have effectively employed this SnS/MoSe$_2$ nanocomposite as an ethanol gas sensor at RT. Comprehensive characterization of the surface morphology and nanostructure using HRTEM, FESEM, XRD, and Raman confirmed the successful synthesis of the as-prepared sample. The high BET-specific surface area of 8.23 m^{2}g^{-1} for pristine-SnS and 12.32 m^{2}g^{-1} for SnS/MoSe$_2$ nanocomposite offers numerous active sites, effectively enhancing their gas-sensing performances. The SnS/MoSe$_2$ sensor exhibited outstanding sensing properties, including a high response, short response-recovery time, excellent repeatability, and selectivity for ethanol detection. The as-fabricated nanocomposite sensor exhibited a noteworthy response value of 26.8 when exposed to 400 ppm ethanol gas. Operating with a p-type characteristics response, this sensor is particularly significant for its RT functionality, allowing the detection of ethanol concentrations as low as 50 ppm. The sensor also demonstrated an improved response time of 9.1 s and recovery time of 15.7 s when exposed to 400 ppm ethanol gas. The remarkable real-time ethanol sensing capability of the SnS/MoSe$_2$ nanocomposite sensor can be attributed to its increased adsorption sites, improved charge carrier transfer, and notable resistance modulation. Heterojunctions-based gas sensors may open the avenue for developing a sensing device for real-time detection of ethanol gas utilizing hybrid 2D materials.

CHAPTER 4

SnS/SnS₂ p-n heterojunctions: accumulation layer-driven rapid and highly sensitive ethanol detection at room temperature
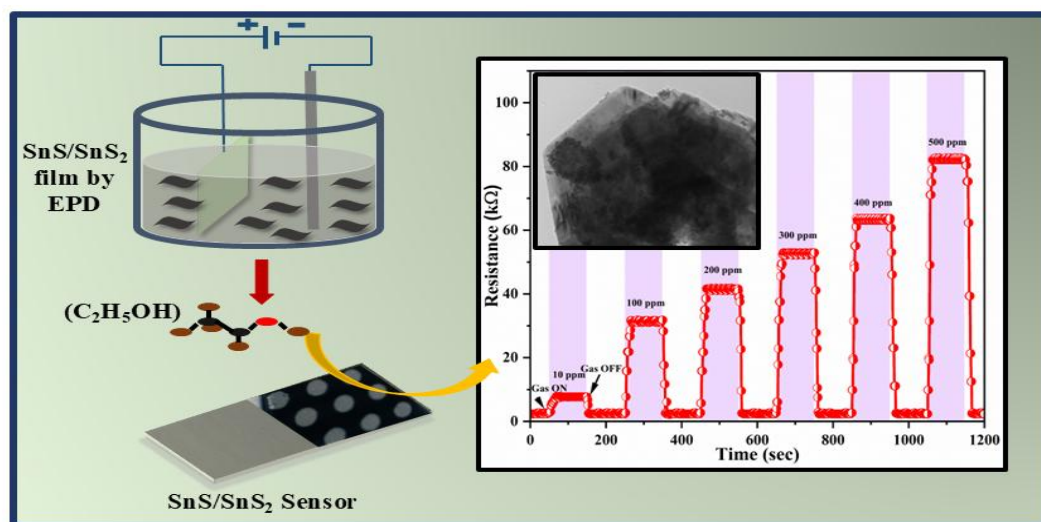
In the previous chapter, we explored SnS/MoSe₂ nanocomposite-based sensor for ethanol gas sensing at RT. The ethanol gas sensing results of the nanocomposite sensor exhibited higher response value, improved response time, and recovery time than the pristine- SnS sensor to 400 ppm ethanol gas. To further enhance the ethanol gas sensing properties of the sensing device at RT, we have explored another nanocomposite of SnS/SnS₂ based on p-n heterojunction for ethanol gas sensing at room temperature. The SnS/SnS₂ heterostructure is found to enhance the response (R_g/R_a) by a factor of 1.8 times that of pristine- SnS, having rapid response and recovery times of 6.1 sec (s) and 18.3 s to 500 ppm ethanol at RT. The SnS/SnS2 nanocomposite shows excellent stability of over 40 days, with superior reproducibility and selectivity, ensuring robust sensing performance with relatively minimal impact from relative humidity. The observed improvement can be primarily attributed to optimal electronic band alignment and specific synergistic properties of nanomaterials. The enhanced sensing performance results from improved electron transport, increased adsorption sites, and effective electron transfer from SnS to SnS2 in the p-n heterojunctions. The present work also proposes novel insights in terms of the strategic design of chemical sensing devices and exploits the synergies based on p-n heterostructures with an electron accumulation layer.

4.1   Introduction

There is a widespread recognition that volatile organic compounds (VOCs), the most prevalent air pollutants, are harmful to human health [1, 2]. VOCs are emitted from various sources commonly experienced in everyday life. These include industrial production, vehicle emissions, fuel combustion, coatings, and adhesives [3]. VOCs are organic compounds that vaporize easily due to their low boiling point at RT. Indoor VOC levels can be up to ten times higher than outdoor levels, with 50 to 300 different VOCs present in indoor air at any given time [4]. The World Health Organization reports that air pollution is the key determinant of premature death and contributes to a variety of diseases [5-7].

Ethanol, a prominent VOC, is widely utilized in traditional industries as both a solvent and a reactant in organic synthesis processes [8-10]. Ethanol becomes highly flammable at elevated temperatures or in the presence of open flames. Moreover, ethanol is reactive and can ignite when it comes into contact with oxidizing agents [11]. A significant amount of ethanol vapor in the air can have harmful effects on the human nervous and circulatory systems, potentially damaging vision and irritating the mucous membranes of the respiratory. Therefore, the rapid detection of ethanol gas has become essential, particularly when its concentration exceeds levels that could pose environmental or health risks [12, 13].

Recently, tin chalcogenides have garnered significant interest for their remarkable physical and chemical properties [14-16]. Among them, SnS is a prominent 2D material with extensive applications, including in lithium-ion batteries, photocatalysis, solar cells, gas sensors, and various other technologies [17-19]. To date, numerous significant studies have focused on SnS- based sensors designed to detect gases like acetone, ethanol, oxygen, and NO_2, leading to further exploration of this material. For instance, M. F. Afsar et al. investigated the gas-sensing properties of SnS nanoplates for acetone and alcohol detection. The study tested the sensor across a temperature span of 25–200 °C and found that it exhibited the highest sensitivity to acetone gas at 100 °C [20]. SnS-functionalized SnO_2 nanowires were employed by J.H. Bang et al. in a different study to detect NO_2. The sensor showed a response time of 69 s at a temperature of 100 °C

and a concentration of 2 ppm [21]. Earlier studies suggest that SnS- based sensors need to enhance their performance, especially when external aids such as temperature control or light exposure were not used during the desorption phase. This can be addressed by leveraging the electronic effect (creating a heterostructure) and the geometric effect (constructing a hierarchical structure) [22]. The limited gas-sensing abilities of pristine nanomaterials stem from their specific physical and chemical properties [23]. Consequently, semiconducting hybrids made from various pristine materials have gained considerable attention because their unique characteristics significantly differ from those of the individual materials [24, 25]. So far, various composites with enhanced gas-sensing properties, including high sensitivity, quick response times, low operating temperatures, and a range of compositions, morphologies, or dispersion states, have been documented [26, 27]. However, most composite research is predominantly empirical, relying on a trial-and-error approach to identify materials for specific gas-sensing applications due to a lack of comprehensive process investigation [28]. Therefore, in light of the exceptional gas-sensing performance of 2D SnS_2 [29-31], we have combined SnS and SnS_2 in an effort to develop a novel, potentially effective material for ethanol detection at RT. SnS_2's layered structure offers a high surface-to-volume ratio, enabling efficient gas adsorption and desorption for enhanced sensitivity and response time. Defects such as sulfur vacancies create additional active sites, improving selectivity and

sensitivity [32]. Its tunable bandgap allows modulation of electronic conductivity upon gas exposure, making it highly suitable for sensing applications [33]. The SnS_2 nano lotus structure (NLS) sensor demonstrates remarkable selectivity for ethanol over other VOCs like methanol and propanol, attributed to its unique structural characteristics and the role of Urbach energy states in modulating gas adsorption and charge transfer [34]. Selectivity can be further optimized through heterostructure engineering, as evidenced by PbS/SnS_2 nanocomposites, which exhibit outstanding ethanol selectivity among various gases [35].

Compared to conventional structures, 2D/2D heterostructures deliver stronger electron orbital interactions between adjacent 2D layered crystals and offer significantly better heterointerface quality. Consequently, the optimized coupling capabilities facilitate

charge transfer by minimizing lattice mismatch, laying the foundation for advancements in next-generation electronics [36]. In light of this, Sn can exist in multiple oxidation states, such as Sn^{2+} ($[Kr] - 4d^{10}5s^05p^0$) and Sn^{4+} ($[Kr] - 4d^{10}5s^25p^2$), when it interacts with sulfur (S), resulting in the formation of SnS and SnS_2, respectively, through hybridization. In this case, SnS is a p-type semiconductor with an orthorhombic structure, whereas SnS_2 is an n-type semiconductor that features a hexagonal unit cell structure [37, 38]. Akhtar et al. fabricated a p-type MoS_2– $NiCo_2O_4$ gas sensor exhibiting high selectivity and a response of 1.63 to 0.1 ppm ethanol at 170 °C, attributed to heterojunction effects and enhanced oxygen adsorption [39]. Kočí et al. developed a room-temperature ethanol vapor sensor based on SH-GO/H-NCD heterostructures, achieving ~ 630 % sensitivity with rapid response (272 s) and recovery (34 s) [40]. Wang et al. developed $MoO_3@SnO_2$ heterostructures, achieving a 48.64 response to 100 ppm ethanol at 200 °C, attributed to high oxygen vacancies and enhanced charge transfer [41]. Yong Zhang et al. fabricated $LaFeO_3$ nanotubes with fast ethanol sensing (2/4 s at 160 °C), highlighting their potential for gas sensors [42]. Consequently, the formation of a 2D SnS/SnS_2 heterostructure will facilitate efficient charge transfer thanks to its abundant active sites and

extensive heterointerface contact, presenting a promising pathway for the fabrication of high- performance, low-power ethanol gas sensors. However, scaling up SnS/SnS_2 heterostructure fabrication for ethanol sensing poses challenges in maintaining uniformity, ensuring reproducibility, and optimizing synthesis for large-scale production [43]. The SnS/SnS_2 nanocomposite sensor in real-world applications must withstand varying temperatures, humidity levels, and interference from other gases. To improve their performance under such conditions, researchers have investigated heterostructure modifications. For instance, the SnS_2/Si heterostructure has been engineered for ultra-selective and rapid NO_2 detection at room temperature, leveraging improved carrier mobility [44].

To the best of our knowledge, we are the first to use the SnS/SnS_2 nanocomposite as a sensing element in a chemiresistive sensor for ethanol detection at RT. While SnS nanoparticles demonstrate good response times, their sensitivity is affected by

stoichiometry, morphology, and environmental factors. The SnS/SnS$_2$ heterostructure mitigates these limitations by enhancing gas adsorption, charge separation, and electron transfer, resulting in superior sensitivity, selectivity, and stability for real-time monitoring applications. The gas sensing performance of the fabricated sensor is measured after exposure to 10–500 ppm of ethanol at RT. The contact interfaces between SnS and SnS$_2$ act as p-n heterojunctions, which improves the sensor's performance. The enhanced sensing performance of the fabricated sensor is attributed to a proposed sensing mechanism. The nanocomposite sensor, developed using nanomaterials and fabricated as a compact film, possesses inherent advantages in terms of portability and miniaturization. Its reduced form factor and low power consumption render it highly suitable for integration into handheld devices and IoT platforms, facilitating the development of compact, cost-effective, and energy-efficient solutions for applications such as environmental monitoring and the advancement of smart, healthy living environments. This work may bring new avenues in progress and applications within the field by focusing on the potential of p-n heterojunctions in terms of ethanol gas sensing.

4.2   Experimentation

4.2.1   Chemicals used

Citric acid (C$_6$H$_8$O$_7$, 99.5%), ethylene glycol (C$_2$H$_6$O$_2$, >99%), thiourea (CH$_4$N$_2$S, 99%), tin (II)   chloride dihydrate (SnCl$_2$·2H$_2$O, 98%), and tin tetrachloride pentahydrate (SnCl$_4$·5H$_2$O, 98%) were all acquired from Sigma Aldrich and utilized directly without further purification.

4.2.2   Preparation of SnS/SnS$_2$ nanocomposite

The SnS nanosheets were synthesized by the simple hydrothermal method as reported in our previous work [45]. Briefly, to synthesize SnS nanosheets, tin (II) chloride, thiourea, and citric acid were utilized in a hydrothermal reaction. 1.4 mmol of CH$_4$N$_2$S and 1.01 mmol of SnCl$_2$·2H$_2$O were dissolved in 30 mL of ethylene glycol with continuous magnetic stirring. Subsequently, 1.1 mmol of citric acid was introduced, and the mixture was stirred for an additional 30 minutes to ensure thorough mixing.

After being placed in a 100 ml stainless steel autoclave, the solution was heated in a hot air oven at 180 °C for 24 hours. After this, the reactor was allowed to cool down to RT on its own. The solution was then rinsed several times with ethanol and left to dry at 80 °C for 24 hours.

SnS_2 was synthesized using a simple hydrothermal process. In particular, 3 mmol of CH_4N_2S and 1.5 mmol of $SnCl_4 \cdot 5H_2O$ were dissolved in 30 mL of deionized water to prepare the solution, followed by magnetic stirring for 30 minutes to ensure complete homogeneity. The reaction mixture was then kept at 200 °C for 24 hours in a 100 mL Teflon-lined autoclave inside a hot air oven. After centrifuging and drying the resulting solution, a yellow powder was obtained. Now, to obtain the nanocomposite, a precise amount of SnS and SnS_2 (2:1 weight ratio), synthesized through the previously described process, was dispersed in a solution of ethanol and deionized water. The dispersion was stirred magnetically for 2 hours, then placed in a hydrothermal autoclave and heated at 160 °C for 24 hours in an oven. Once cooled to RT, the SnS/SnS2 nanocomposite precipitate was centrifuged and then subjected to drying in a vacuum oven to obtain the final powder.

4.2.3   Sensor fabrication and experimental set-up

A set of procedures were carried out to fabricate an ethanol gas sensor utilizing the SnS/SnS_2 nanocomposite. The hydrolyzed ITO slides were thoroughly cleaned with IPA and deionized water multiple times and subsequently dried in an oven at 60 °C for 30 minutes [46]. Next, the electrophoretic deposition (EPD) method was used to create a thin film of the SnS/SnS_2 nanocomposite. Acetonitrile was used to disperse the resulting powder to get a concentration of 1.5 mg/mL. As shown in Fig. 4.1, the solution was introduced into a two-electrode EPD cell containing a working electrode (WE) and a counter electrode (CE), with the ITO on the WE being exposed to an optimal potential for 180 s. The resulting film was then left to dry overnight. Ultimately, the produced film was coated with silver (Ag) electrodes using the thermal evaporation method (Smart Coat 3.0, Hind High Vacuum). A pressure of 4×10^{-6} mbar was sustained in the chamber during the evaporation. Five SnS/SnS_2 nanocomposite gas sensors were fabricated independently for reproducibility analysis. The nanocomposite sensor's

estimated power consumption, based on its operating conditions, was 2 mW. Ethanol sensing measurements were conducted using the as-fabricated sensing device.
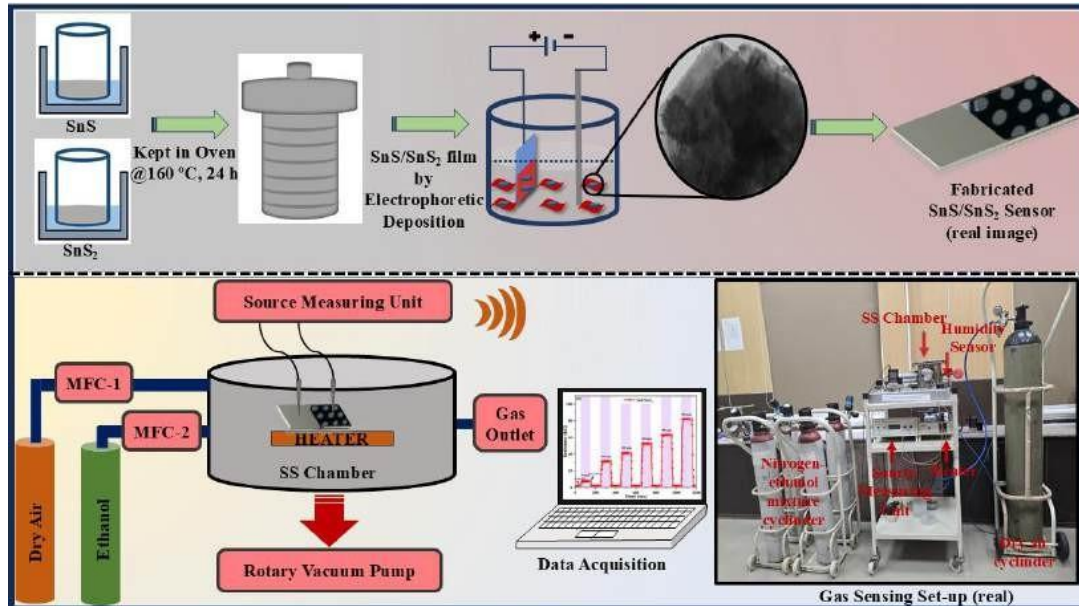
Fig. 4.1: The schematic illustration of the fabrication process and gas sensing setup for the SnS/SnS$_2$ nanocomposite ethanol sensor.

A custom-designed stainless steel (SS) chamber was utilized for performing the ethanol gas sensing tests. The source measuring unit (SMU) provided a stable current to the SnS/SnS$_2$ nanocomposite ethanol sensor. To start the process of detecting ethanol, a rotary pump is used to generate a rough vacuum inside the SS chamber. To establish a constant baseline resistance, dry air was introduced for 50 s. Since air contains oxygen, which can interfere with gas detection mechanisms, affect chromatographic separation, and introduce moisture variability, it is generally not used as a carrier gas for ethanol [47, 48]. Afterward, a gas mixture containing 1% ethanol and 99% dry nitrogen was introduced into the chamber. Response time (t_{resp}) denotes the duration for a sensor to attain 90 % of its stabilized signal upon gas exposure, while recovery time (t_{rec}) represents the period required to revert to 10 % of its baseline after gas removal. These parameters are critical for assessing sensor efficiency and real-time monitoring capability [49, 50]. The concentration of ethanol gas inside the SS chamber was measured in parts per million (ppm) using the following equation:

$$C = \frac{22.4 \times \Psi \times \rho \times V_1}{M \times V_2} \times 1000 \tag{4.1}$$

The above equation (4.1) represents the ethanol gas concentration, where C (ppm) denotes the concentration, φ is the gas volume fraction, ρ (kg·m⁻³) is the density of ethanol, V_1 (L) is the volume of ethanol gas, M (kg·mol⁻¹) is the molecular weight of ethanol, and V_2 (m³) is the volume of the SS chamber [51, 52]. To record the variations in the sensing film's resistance, data acquisition software (LabView), connected to the SMU, was used.

4.3   Results and discussion

XRD patterns characterize the composition and crystal structure of pristine-SnS, SnS_2, and SnS/SnS_2 nanocomposites. As illustrated in Fig. 4.2, the pristine-SnS, pristine-SnS_2, and SnS/SnS_2 nanocomposite distinctly display characteristic peaks attributed to SnS (JCPDS No. 39-0354) and SnS_2 (JCPDS No. 23-0677). The diffraction peaks at 38.27°, 31.96°, 31.53°,

30.48°, 27.47°, 25.99°, and 21.99° are distinctly attributed to the (131), (040), (111), (101), (021), (120), and (110) planes of the SnS orthorhombic phase [53]. Meanwhile, the peaks at 50.05°, 41.95°, 32.17°, 28.27°, and 15.04° correspond to the (110), (102), (101), (100), and (001) planes of the SnS_2 hexagonal phase [54], confirming their distinct crystalline structures.

The XRD patterns of the SnS/SnS_2 nanocomposite reveal prominent diffraction peaks of SnS_2 at 15.04°, 28.27°, and 41.95°, corresponding to the (001), (100), and (102) planes. Notably, two strong peaks at 25.99° and 31.53°, perfectly aligned with the (120) and (111) planes of SnS, further emphasize the crystalline integrity of the nanocomposite. The absence of the (110) plane in SnS is likely due to the predominant intensity of the characteristic peaks from both SnS and SnS_2. Thus, the XRD results unequivocally confirm the successful fabrication of SnS/SnS_2 nanocomposite [55]. The XRD patterns of other optimized SnS/SnS_2 weight ratios are provided in the Supporting Information.
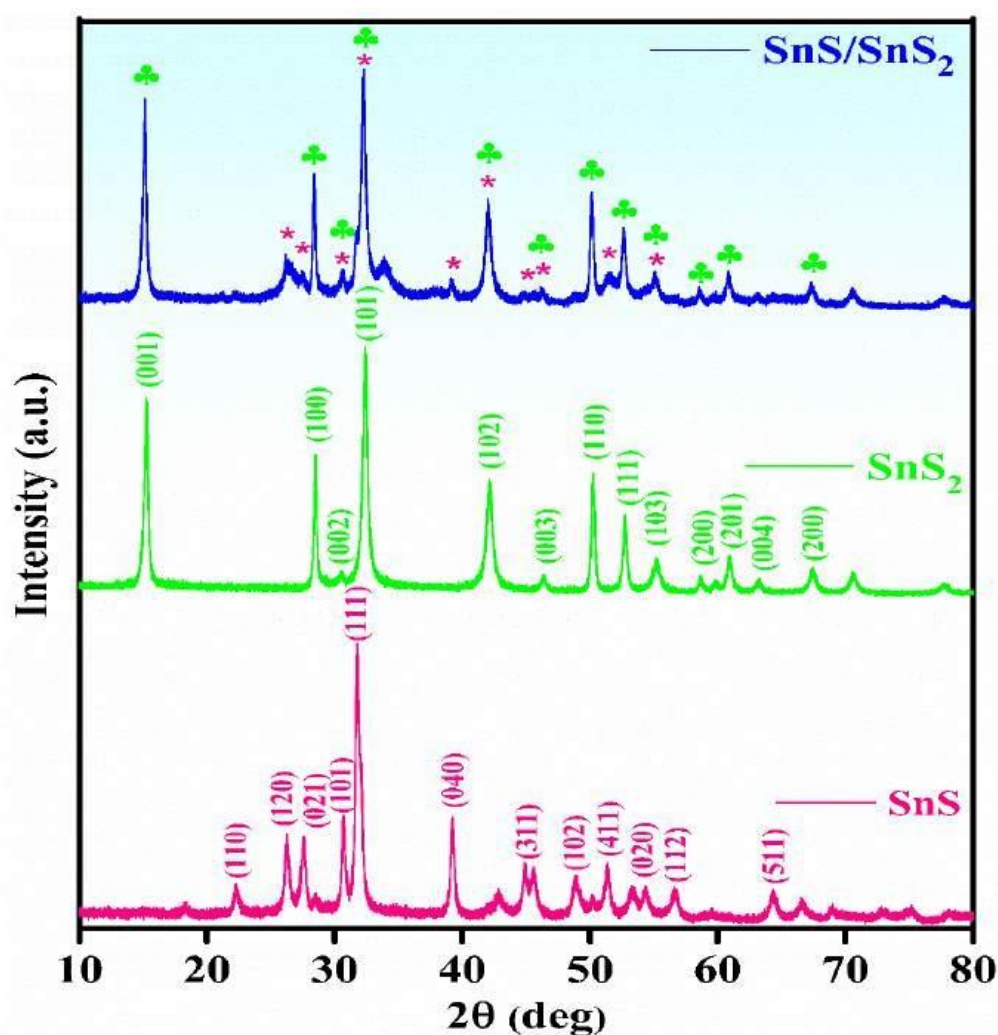
**Fig. 4.2: XRD patterns of pristine-SnS, pristine-SnS₂, and SnS/ₛₙₛ₂ nanocomposite.**

Raman spectroscopy was employed to elucidate the distinct phase formations of the as- synthesized samples, including pristine-SnS, pristine-SnS₂, and the SnS/SnS₂ nanocomposite, highlighting their unique structural characteristics. The Raman spectra of SnS showcased a number of well-defined peaks at 94 cm⁻¹, 146 cm⁻¹, 178 cm⁻¹, and 219 cm⁻¹, which are attributed to the A_g, B_{2u}, B_{1u}, and A_g vibrational modes of SnS, respectively [56] (Fig. 4.3(a)). Additionally, a sharp peak at 312 cm⁻¹, attributed to the A_{1g} mode of SnS₂, emphasized the distinct vibrational fingerprints of the phases [36] (Fig. 4.3(b)).
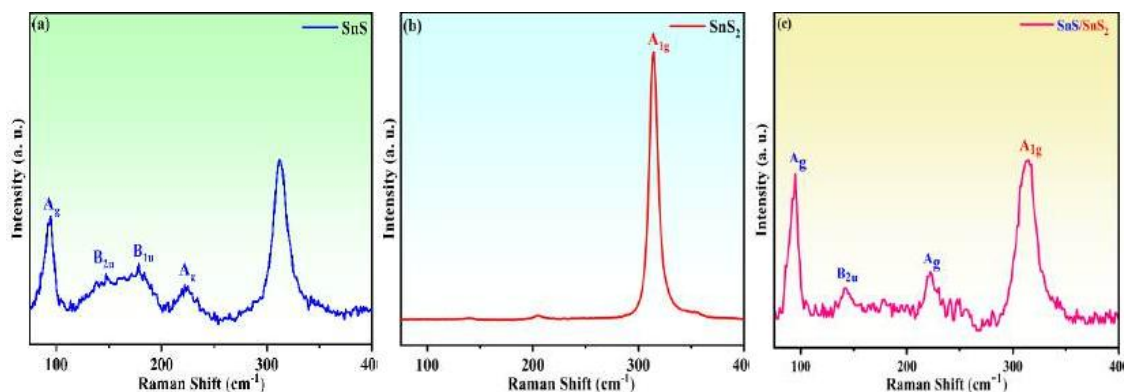
Fig. 4.3: Raman spectra of (a) pristine-SnS, (b) pristine-SnS$_2$, and (c) SnS/SnS$_2$ nanocomposite.

In Fig. 4.3(a), the peak at 312 cm^{-1} is associated with the secondary tin sulfide phase, Sn$_2$S$_3$. This peak is likely attributed to intralayer chalcogen-chalcogen vibrations, underscoring crucial atomic interactions within the material [57]. Fig. 4.3(c) shows the acquired spectra which reveal the characteristic peaks of both SnS and SnS$_2$ phases, reflecting strong electrical interactions within the layered material and supporting the generation of a 2D/2D SnS/SnS$_2$ nanocomposite. The SnS/SnS$_2$ nanocomposite exhibits distinct peaks with slight intensity changes, highlighting the synergistic interactions between SnS and SnS$_2$ during hydrothermal synthesis [58]. The Raman spectrum, along with XRD and TEM analysis, unequivocally confirms the successful synthesis of the SnS/SnS$_2$ nanocomposite.

BET analysis, using N$_2$ adsorption-desorption isotherms (Fig. 4.4(a)) for pristine-SnS and Fig. 4b for pristine-SnS$_2$, and 4.4(c) for SnS/SnS$_2$ nanocomposite), revealed the SnS/SnS$_2$ nanocomposite's surface area. The BET surface area of pristine-SnS, pristine-SnS$_2$, and SnS/SnS$_2$ nanocomposites is 5.30 m^2/g, 13.47 m^2/g, and 15.31 m^2/g, respectively, demonstrating a significant increase in the surface area, as revealed by the Brunauer-Emmett- Teller method. Obviously, the SnS/SnS$_2$ nanocomposite offers a larger surface area, enhancing the adsorption sites and transport pathways for ethanol molecules, which helps in boosting the gas-sensing performance, particularly for detecting low-concentrations [59]. The N$_2$ adsorption-desorption isotherm in Fig. 4.4 exhibits a Type IV curve with a prominent hysteresis loop between relative pressures of 0.1 and 1.0, confirming the mesoporous nature of the structure [60].
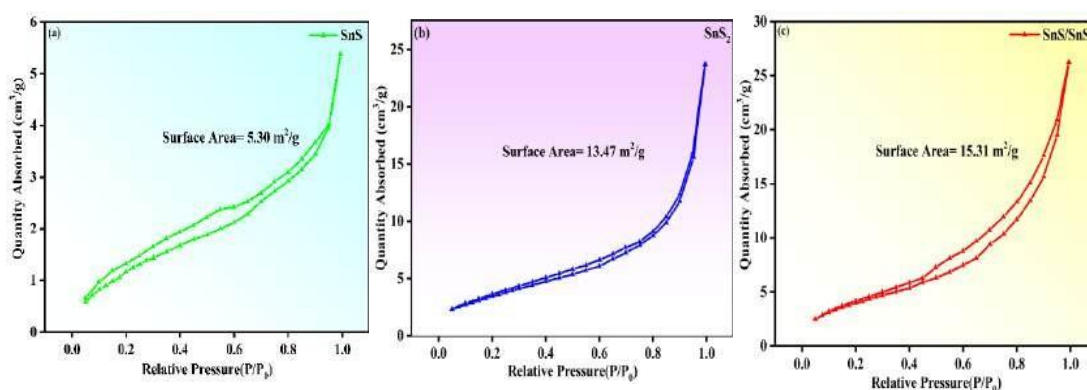
Fig. 4.4: Shows the N_2 adsorption-desorption isotherms for the pristine-SnS, pristine SnS_2, and SnS/SnS_2 nanocomposite.

Transmission electron microscopy (TEM) provides detailed insights into the microstructure of the prepared materials. Fig. 4.5(a) displays a wide area of pristine-SnS nanosheets in a stacked formation, along with TEM images of SnS_2 at low magnification (Fig. 4.5(b,c)), highlighting the successful synthesis of hexagonal nanosheet-like structures [61, 62]. Fig. 4.5(d, e) illustrates the successful modification of SnS nanosheets with SnS_2 hexagonal nanosheets, confirming the incorporation of SnS_2 into the SnS nanosheet structure. The selected area electron diffraction (SAED) pattern of the as-prepared SnS/SnS_2 nanocomposite, shown in Fig. 4.5(f), provides a clear depiction of its crystalline phase and structural integrity. The (111) and (120) planes are attributed to the orthorhombic SnS structure, while the (100) plane corresponds to the hexagonal SnS_2 structure. Fig. 4.5(g, h) presents the HRTEM analysis used to systematically evaluate the structural integrity of the SnS/SnS_2 heterointerface and the uniformity of the nanocomposite. The results reveal atomic-level alignment at the interface, with measured lattice spacings of 0.26 nm and 0.32 nm, corresponding to the hexagonal (101) plane of SnS_2 and the orthorhombic (210) plane of SnS, respectively. These findings confirm the crystallographic coherence of the heterostructure [63]. These observations are in perfect harmony with the XRD results, further validating the structural consistency of the nanocomposite [64, 65].

SEM measurements were conducted to further examine the morphology and microstructure of the as-synthesized samples. The obtained images of the (a) pristine-SnS, (b) pristine-SnS_2, and

(c) SnS/SnS$_2$ nanocomposite are shown in Fig. 4.6. The pristine-SnS exhibits a random distribution and asymmetric sheet-like structures. These SnS nanosheets have a sheet length of approximately 500–700 nm and are well interconnected, forming a multilayer structure (Fig.4.6(a)). The SnS$_2$ nanosheets have a hexagonal structure and are approximately 800 nm in size, as shown in Fig. 4.6(b) [62].
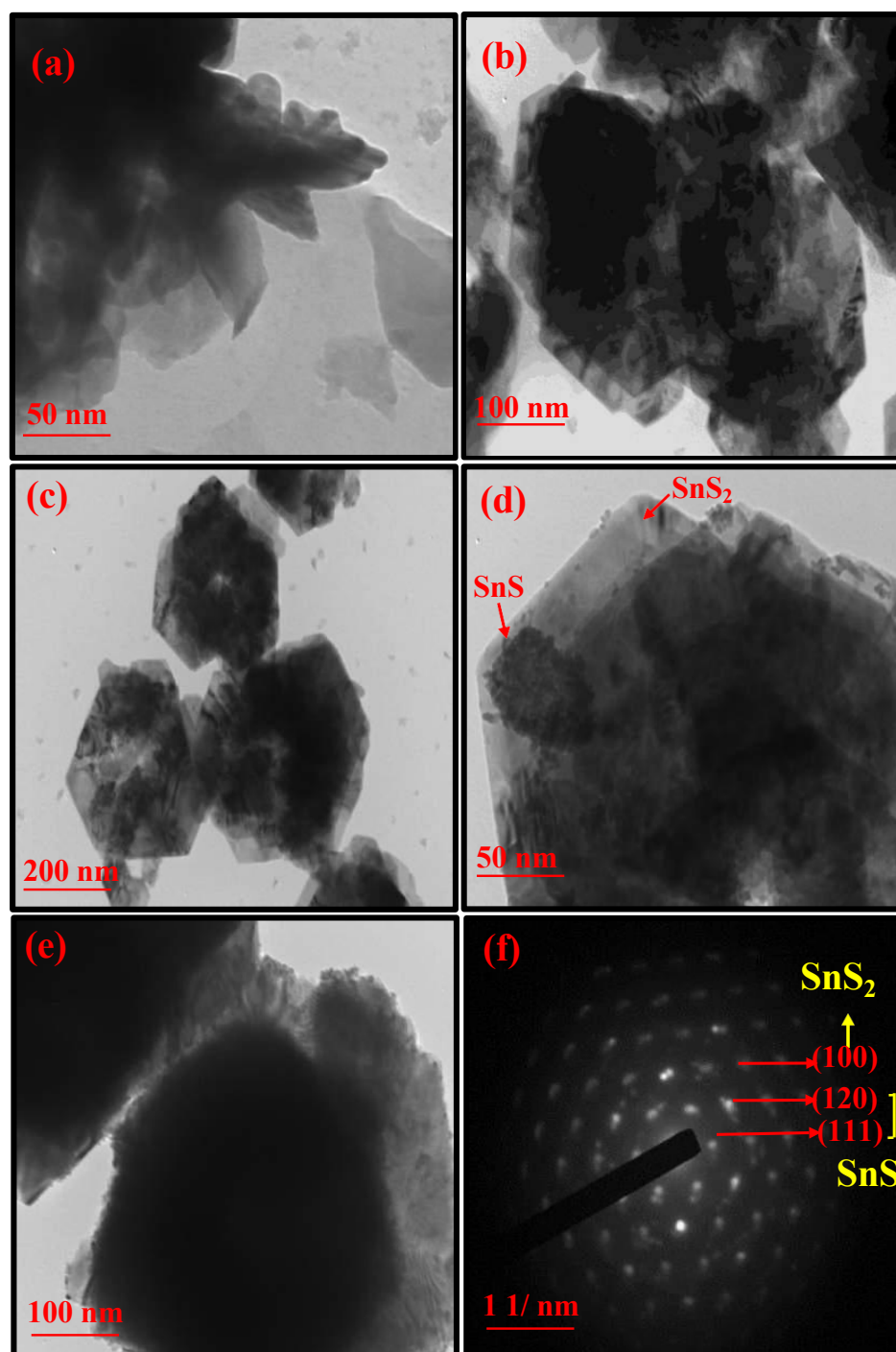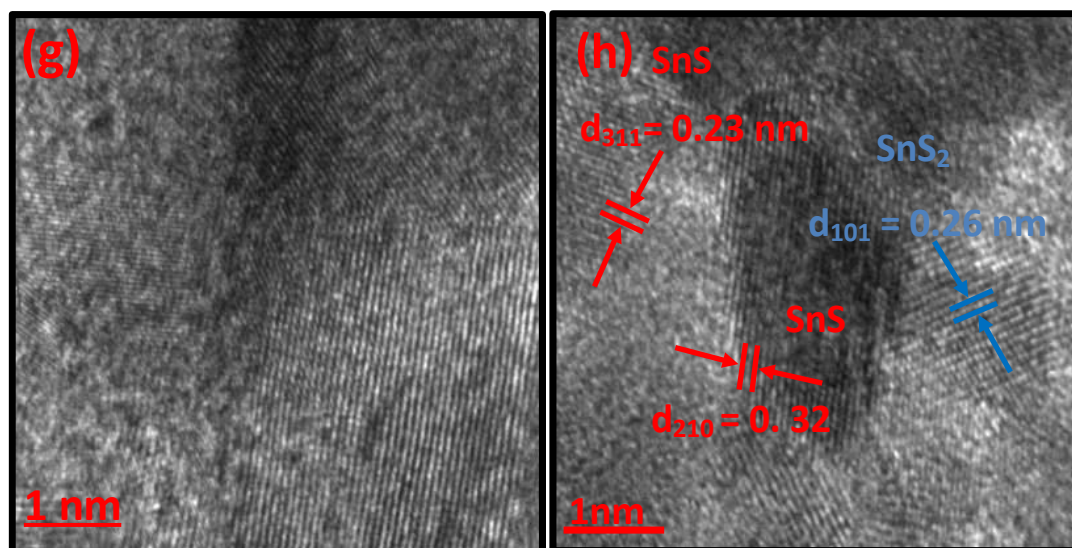
Fig. 4.5: TEM images of (a) pristine-SnS, (b, c) pristine-SnS$_2$, (d, e) SnS/SnS$_2$ nanocomposite at varying magnifications, (f) SAED pattern of the nanocomposite, and (g, h) Lattice fringes of SnS and SnS$_2$ nanosheets with measured interplanar spacing.

These nanosheets are uniformly distributed and feature numerous edges, as observed in the low-magnification SEM image, which enhances the availability of active sites. The interaction between SnS and SnS$_2$ nanosheets is illustrated in Fig. 6(c), which shows a clear image of the SnS/SnS$_2$ nanocomposite. These images, along with the TEM images, suggest potential synergistic interactions between the constituent materials. These nanosheets are highly dispersible and loosely layered, creating numerous pathways that facilitate test gas adsorption and enhance the sensing capabilities of the gas sensor [66].
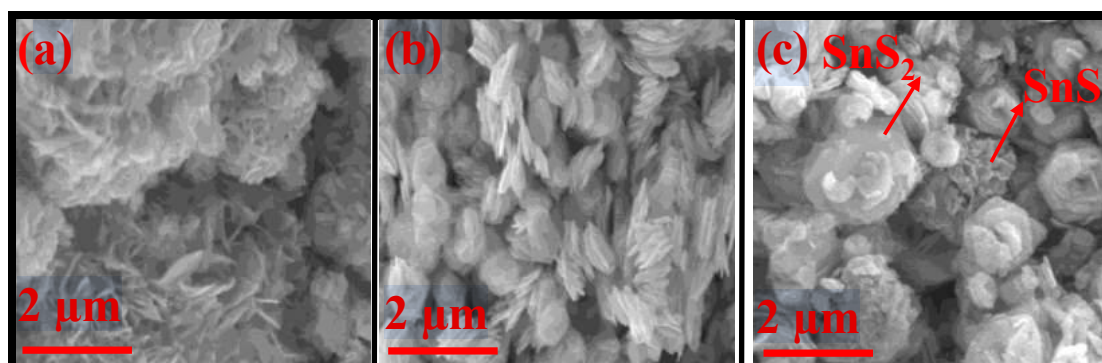

Fig. 4.6: SEM images illustrating the morphology of (a) pristine-SnS, (b) pristine-SnS$_2$, and (c) the SnS/SnS$_2$ nanocomposite.

4.4   Gas Sensing Performance

The gas-sensing capabilities of pristine-SnS and SnS/SnS$_2$ p-n heterostructures were assessed at RT by monitoring the resistance variations in the sensors under exposure to different ethanol concentrations. Fig. 4.7(a) and (b) depict the sensing performance of the pristine-SnS and the p- n heterostructured SnS/SnS$_2$ sensor at different concentrations of ethanol gas. This suggests that the SnS/SnS$_2$ p-n heterostructures exhibit the same typical p-type characteristics as pristine-SnS. The resistance change of the sensor increases with the ethanol concentration, as observed in Figs. 4.7(a) and (b). Consequently, the response value (R_g/R_a) increases, where the sensor's resistance in ethanol gas is represented by R_g, and in air by R_a, respectively. As depicted in the insets of Fig. 4.7(b), the sensor's response demonstrates a favorable linearity, following the equation y = 0.0645x + 4.095. A high correlation coefficient ($R^2 = 0.994$) is obtained within the concentration range of 10–500 ppm, indicating strong linear dependence. This linear relationship enables the determination of unknown ethanol gas concentrations by comparing the sensor's response with the reference curve. Notably, the formation of the p-n heterostructure in SnS/SnS$_2$ significantly improves the sensor's response performance. In particular, the SnS/SnS$_2$ p-n heterostructured sensor exhibits a 1.8-fold improvement in gas response to 500 ppm ethanol, outperforming the pristine SnS sensor.
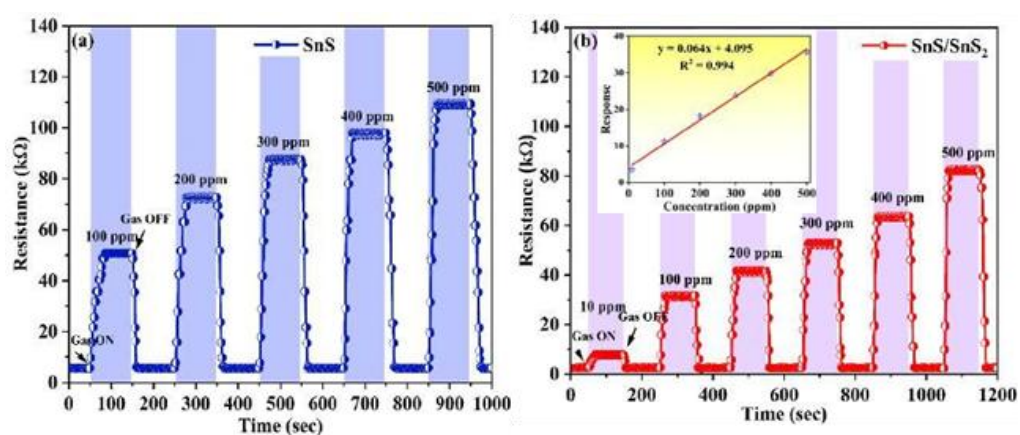
Fig. 4.7: (a) and (b) Ethanol concentration-dependent resistance variation curves for pristine-SnS and SnS/SnS$_2$ nanocomposite sensors at RT; insets illustrate the corresponding variations in response as a function of ethanol gas concentration.

The response time (t_{resp}) and recovery time (t_{rec}) of the pristine-SnS and SnS/SnS$_2$ sensors, measured at RT, are presented in Fig. 4.8(a). It is evident that the pristine-SnS sensor demonstrates a response time (t_{resp}) of 11.3 s and a slow recovery time (t_{rec}) of 22.3 s at 500 ppm. However, for the SnS/SnS$_2$ sensor, both the response and recovery times are significantly improved, with t_{resp} reduced to 6.1 s and t_{rec} decreased to 18.3 s at 500 ppm, respectively. The significant reduction in t_{resp} and t_{rec} in our SnS/SnS$_2$ nanocomposite sensor is highly beneficial for RT ethanol gas detection. In the case of the SnS sensor, the high number of active sites on the sensor's surface promotes the adsorption of ethanol gas molecules but causes slower and more prolonged recovery. On the other hand, the p-n heterostructure of SnS/SnS$_2$ enhances the diffusion of gas molecules, which makes the response and recovery time faster. The SnS (p- type)/SnS$_2$ (n-type) heterostructure enhances gas sensing by facilitating efficient electron transport, improving conductivity through charge transfer driven by Fermi level alignment. It creates additional adsorption sites at the interface, increasing gas interaction and sensitivity [67]. Furthermore, it minimizes charge accumulation by promoting electron-hole separation, ensuring rapid response and recovery. The heterostructure also optimizes surface properties, enhancing gas diffusion to active sites, further improving sensing efficiency [67, 68]. This may also be the reason for the decrease in both response time (t_{resp}) and recovery time (t_{rec}) [69]. Moreover, the SnS/SnS$_2$ sensor exhibits a large specific surface area, offering more active sites [70]. These active sites facilitate faster response and recovery processes.
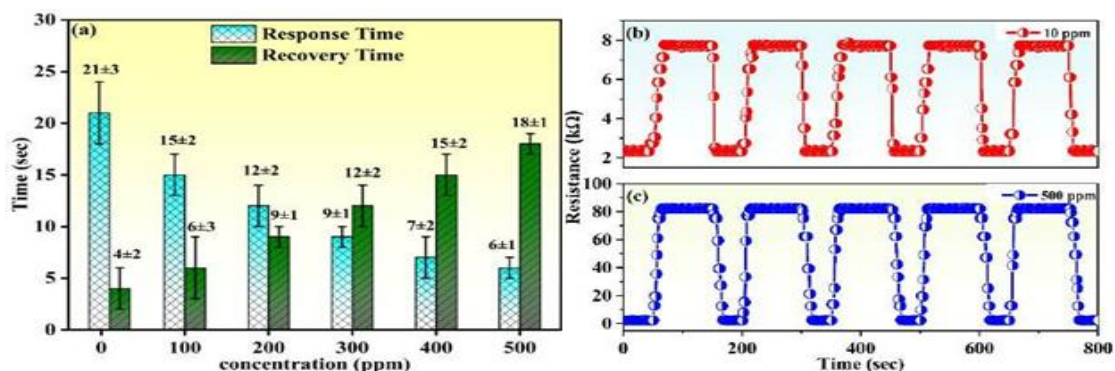
Fig. 4.8: (a) t_{resp} and t_{rec} as a function of ethanol concentration, and (b, c) repeatability analysis of the SnS/SnS$_2$ nanocomposite sensor at 10 ppm and 500 ppm ethanol gas.

A practical gas sensor must exhibit excellent repeatability, ensuring consistent performance when repeatedly expose to identical concentrations of the target gas. The repeatability of the SnS/SnS$_2$ sensor was assessed by subjecting it to 10 ppm and 500 ppm of the target gas across five consecutive response-recovery cycles at RT, as outlined in Fig. 4.8(b) and (c). When exposed to 10 ppm of ethanol gas, the sensor exhibits response values of 3.4, 3.2, 3.5, 3.4, and 3.3, yielding a relative standard deviation (RSD) of 3.39%. At 500 ppm, the response values are 35.8, 35.3, 34.7, 35.2, and 35.7, with a corresponding RSD of 1.24%. The low RSD values confirm the sensor's high repeatability and reliability for ethanol detection. Throughout repeated cycles of ethanol gas adsorption and desorption, the sensor maintained a consistent initial resistance, with nearly identical responses observed in each cycle.

Selectivity is another crucial aspect of a practical gas sensor. Fig. 4.9 presents a radar plot illustrating the sensing device's response to a variety of VOCs, including ethanol, benzene, acetone, isopropyl alcohol (IPA), formaldehyde, and methanol at a concentration of 500 ppm, measured at RT.
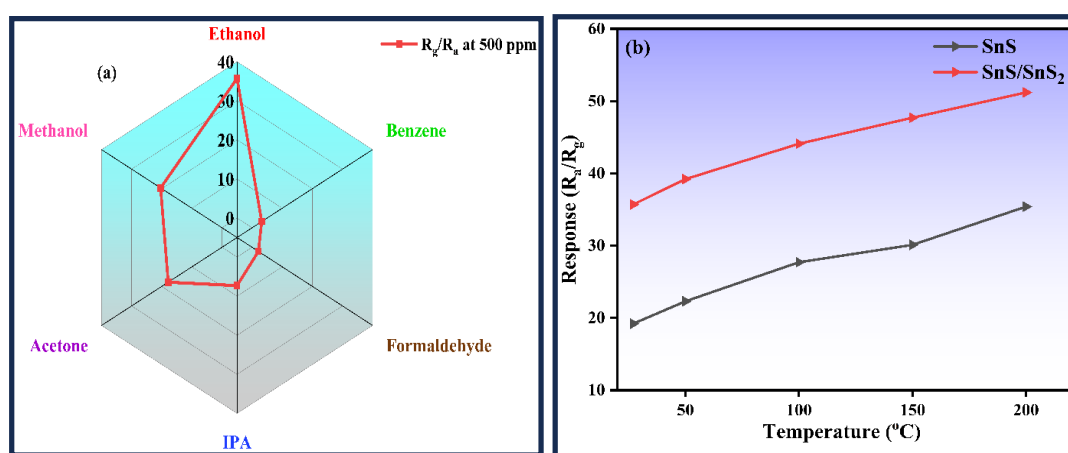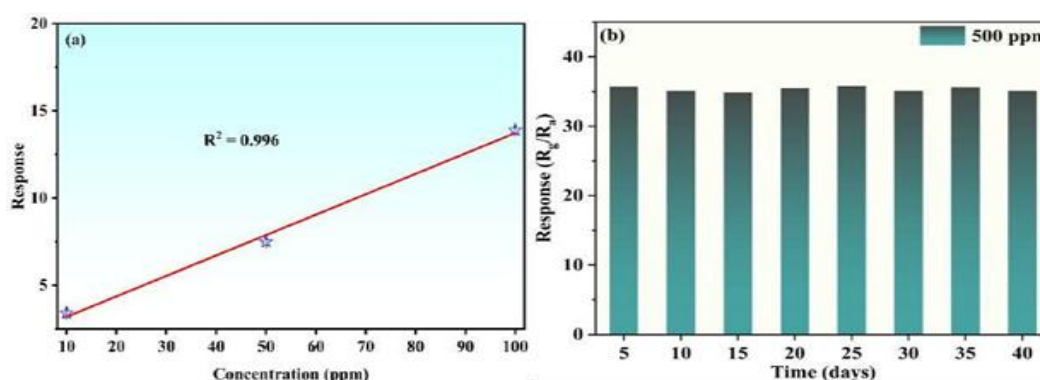

Fig. 4.9: (a) Selectivity of the SnS/SnS$_2$ nanocomposite sensor to various VOCs at 500 ppm and RT, (b) Temperature-dependent ethanol gas response of pristine-SnS and SnS/SnS$_2$ nanocomposite sensor.

The selectivity of the sensor was assessed using the Selectivity Factor (SF) to quantify its ability to differentiate ethanol from other VOCs. The calculated SF values reveal that the sensor's response to ethanol is 1.9 times higher than acetone (SF = 1.9), 11.1 times higher than benzene (SF = 11.1), 4.8 times higher than iso-propyl alcohol (IPA) (SF = 4.8), 17.1 times higher than formaldehyde (SF = 17.1), and 1.7 times higher than

methanol (SF = 1.7). These results indicate that the SnS/SnS$_2$ nanocomposite sensor exhibits significantly higher selectivity toward ethanol compared to other VOCs. Additionally, the sensor demonstrates a rapid response and recovery, making it a promising candidate for efficient ethanol gas detection.

Operating temperature plays a vital role in the adsorption–desorption dynamics of chemiresistive sensors, as it directly influences the surface states of the sensing material and thereby impacts overall gas sensing performance. Fig. 4.9(b) illustrates the response of pristine SnS and SnS/SnS$_2$ nanocomposite sensors at 27 °C (RT), 50 °C, 100 °C, 150 °C, and 200 °C. The sensor response increases consistently with rising temperature, which is attributed to the enhanced chemisorption of oxygen species, leading to improved surface reactivity and sensing efficiency.

The limit of detection (LOD) is a critical parameter that defines the minimum concentration at which the sensor's response can be reliably distinguished from baseline noise, providing a key measure of its sensing performance. The LOD is determined using the formula LOD = 3 × RMS$_{noise}$/Slope, where RMS$_{noise}$ represents the standard deviation of the baseline response. The sensor response to ethanol (1–100 ppm) exhibits a linear fit with a slope of 0.118 and a correlation coefficient (R^2 = 0.996), enabling the estimation of the theoretical LOD, as shown in Fig. 4.10(a). Based on this calculation, the LOD for ethanol gas in the 1–100 ppm range is estimated to be 3 × 0.156/0.118 = 3.9 ppm. The sensitivity of the gas sensor, measured as the slope of the calibration curve, is determined to be 0.11 kΩ/ppm, demonstrating its effectiveness in ethanol detection within the tested range.

Fig. 4.10: (a) Calibration curve with linear fit for the SnS/SnS$_2$ nanocomposite sensor's response to ethanol (1–100 ppm), (b) long-term stability of the response over 40 days to 500 ppm ethanol gas for the SnS/SnS$_2$ nanocomposite sensor at RT.

To assess the prolonged stability of the SnS/SnS$_2$ nanocomposite sensor, its response to 500 ppm ethanol gas at RT is monitored over a 40-day period. Regular measurements are taken every 5 days to track any changes in the sensor's performance, providing insight into its durability and consistency over time. As depicted in Fig. 4.10 (b), there is no prominent change in the sensor's response over 40 days, indicating the sensor's strong potential for long-term ethanol gas detection at RT. Additionally, stability measurements were taken at 4-day intervals in the presence of interfering gases such as isopropanol, benzene, and formaldehyde. The sensor showed a consistent response to ethanol with only a 7–8% variation, demonstrating excellent selectivity (Fig. 4.11 (b)). Stability at elevated temperature (150 °C) was also evaluated over the same intervals, with a slight 6% variation in response, confirming the sensor's robustness under high-temperature conditions (Fig. 4.11(a)). High humidity can influence adsorption dynamics, temperature variations may impact sensitivity, and interfering gases can affect selectivity. However, SnS$_2$-based sensors have demonstrated stability over weeks under controlled conditions, with mitigation strategies such as encapsulation, surface modification, and protective layers [67, 71].
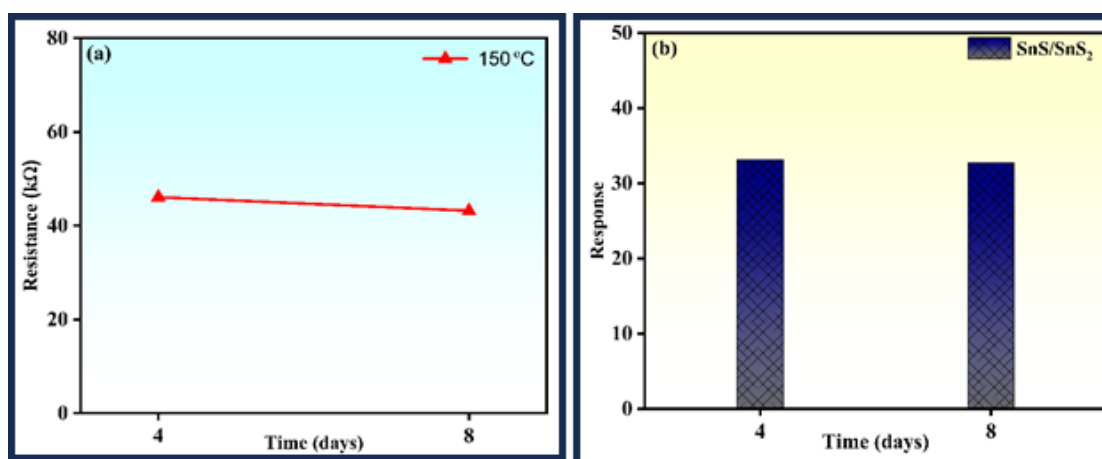
Fig. 4.11. (a) Stability of the SnS/SnS$_2$ sensor toward 500 ppm ethanol at high temp. 150 °C and (b) response to interfering gases at room temperature.

Fig. 4.12 (a) presents the response values of five SnS/SnS$_2$ nanocomposite gas sensors upon exposure to 500 ppm of ethanol gas at room temperature. The recorded response values are 35.9, 33.2, 36.3, 34.1, and 34.5, exhibiting minimal variation with a relative standard deviation of just 3.69%. This low deviation highlights the high reproducibility

and consistent sensing performance of the SnS/SnS$_2$ nanocomposite sensors, underscoring their reliability for ethanol gas detection under identical testing conditions.
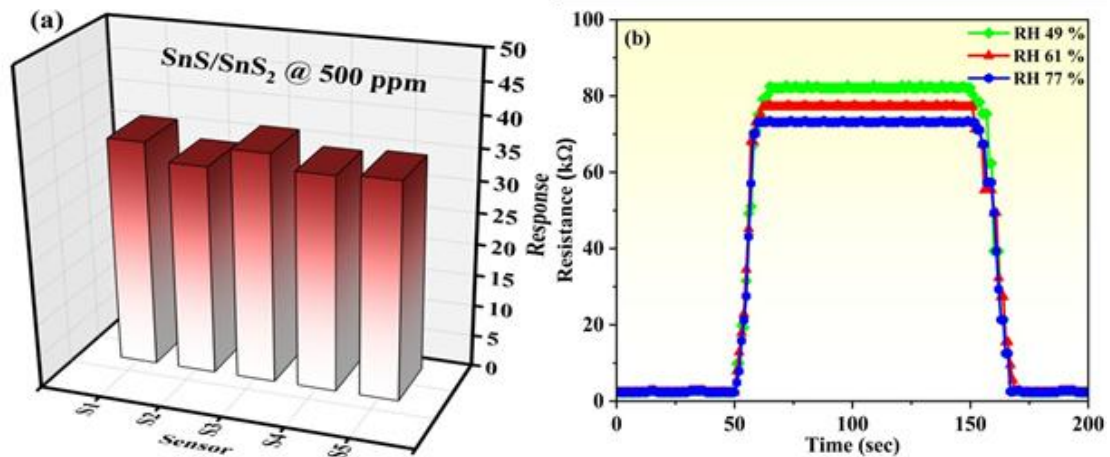
Fig. 4.12: (a) Reproducibility analysis of five different SnS/SnS$_2$ nanocomposite sensors, and (b) the influence of relative humidity (RH) on their response to 500 ppm ethanol at RT.

As expected, an increase in relative humidity (RH) causes a reduction in the sensor's response. Under varying environmental conditions, the SnS/SnS$_2$ nanocomposite sensor exhibits responses of 35.7, 33.5, and 31.7 at relative humidity levels of 49%, 61%, and 77%, respectively. As illustrated in Fig. 4.12(b), these results highlight the significant impact of humidity on the sensor's performance, with increased humidity leading to a decrease in its response. The reduced sensor response at higher humidity levels is attributed to the occupation of adsorption sites by water vapor, limiting their availability for target gas interactions. As a result, the adsorption of target gas molecules onto the sensing layer is hindered, leading to a reduction in the sensor's response.

To comprehensively evaluate the ethanol gas sensing performance of our sensor, Table 4.1 presents a detailed comparison of the nanocomposite explored in this study with those reported in the existing literature. The comparison findings indicate that the SnS/SnS$_2$ nanocomposite- based ethanol sensor outperforms previously reported ethanol gas sensors with its higher response value (R_g/R_a), rapid response and recovery times, excellent long-term stability, and operation at RT.

Table 4.1: Comparison of the ethanol gas sensing performance of SnS/SnS₂ nanocomposites with previously reported works.

| Sensor Materials	Operating Temperature (°C)	Concentration (ppm)	Sensor Response (S)	Response/ Recovery Time (sec)	Stability (days)	Refs.
CuO-ZnO/g-C3N4	260	500	16[b]	87 / 169	30	[72]
MoO2/MoO3/MXene	RT	100	10.8[b]	-	15	[73]
WO3/g-C3N4	RT	500	62.5[c]	30 / 25	60	[74]
Pd decorated ZnO	260	500	81[d]	6 / 95	22	[75]
MoS2/TiO2	300	500	100[c]	70 ± 10 / 90 ± 20	56	[76]
In2O3/ZnO/Ti3C2TX	RT	100	6.5[b]	-	30	[77]
SnS	300	300	13[c]	29 / 21	28	[20]
PbS/SnS2	RT	60	45.64[c]	104 / 84	-	[35]
SnS/SnS2	**27 (RT)**	**500**	**35.7[a]**	**6.1 / 18.3**	**40**	**[This Work]**

[a] indicates that $S = R_g/R_a$; [b] indicates that $S = R_a/R_g$; [c] indicates that $S = (R_g-R_a/R_a) \times 100$; [d] indicates that $S = (R_a-R_g/R_a) \times 100$

4.5 Sensing Mechanism

The superior sensing performance of the SnS/SnS₂ nanocomposite sensor is elucidated through its energy band structure. SnS and SnS₂ form a p-n heterostructure that enhances the sensing capability, facilitated by the alignment of their Fermi levels, with p-type SnS positioned near the valence band and n-type SnS₂ near the conduction band. SnS/SnS₂ heterostructures exhibit typical p-type gas sensing behavior, with holes primarily influencing the sensing sensitivity. As depicted in Fig. 4.13, SnS possesses a work function of 4.8 eV, while SnS₂ exhibits a work function of 5.08 eV. According to the literature, the energy band gap of SnS is 1.6 eV, while that of SnS₂ is 2.3 eV [55, 67]. SnS₂ has a higher work function compared to SnS, leading to

"Fermi level-mediated charge transfer" between SnS and SnS₂ during the formation of the SnS/SnS₂ p-n heterostructure [55]. When SnS and SnS₂ establish contact, electrons transfer from SnS to SnS₂ until their Fermi levels align, establishing a common Fermi level as a result of initial disparity in their Fermi energies. The SnS/SnS₂ heterostructure formation triggers the movement of charge carriers through diffusion

and drift, leading to a charge accumulation region   and   band   bending

at   the   junction   interface   [78]. Oxygen molecules from the ambient

environment adsorb onto the surface of the SnS/SnS$_2$ nanocomposite sensor. These

adsorbed molecules partially ionize into O^-, O_2^-, and O_2^{2-} species, depending on the
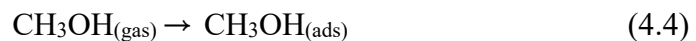
operating temperature [55].
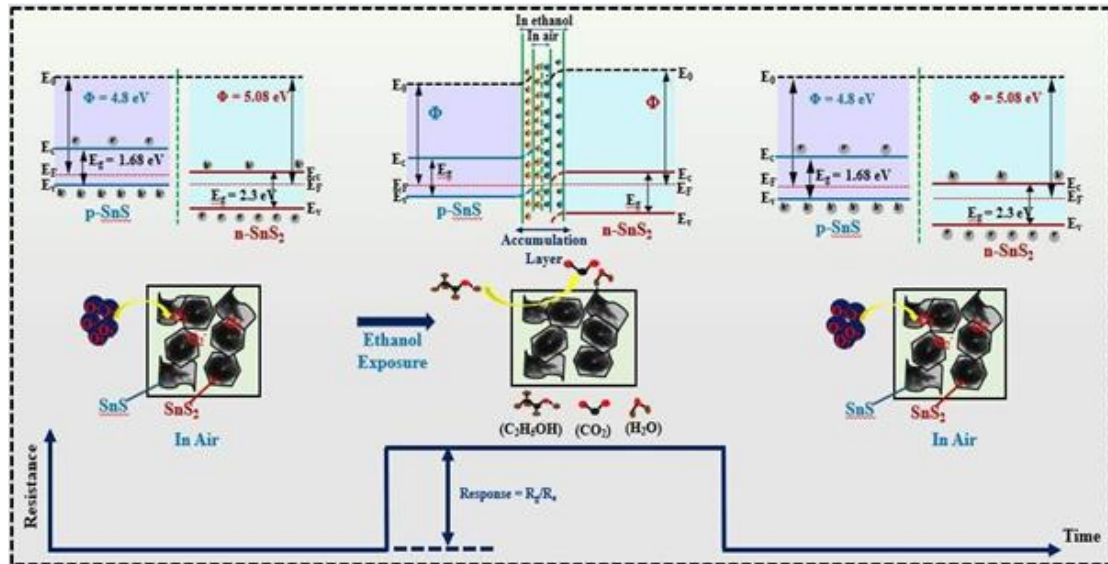
Fig. 4.13: Diagram showing the behavior of the SnS/SnS2 nanocomposite sensor's ethanol gas detection mechanism both before and after exposure to ethanol.

Because of this process, a layer of charge accumulation is created, with the adsorption

kinetics described by eqs. 4.2 and 4.3. At operating temperatures below 100°C, O_2^-

species adsorb onto the sensor surface, creating a space-charge layer. This layer

significantly influences the steady- state baseline resistance, affecting the sensor's

response to the ambient air [79].

$$(O_2)_{gas} \rightarrow (O_2)_{ads} \tag{4.2}$$

$$(O_2)_{ads} + e- \leftrightarrow (O^-{}_2)_{ads} \tag{4.3}$$

When exposed to reducing ethanol, a redox reaction occurs between the ethanol

molecules and the adsorbed O_2^-, resulting in the release of trapped electrons. The

equations are given as follows:

$$CH_3OH_{(gas)} \rightarrow CH_3OH_{(ads)} \tag{4.4}$$

$$2CH_3OH_{(ads)} + 3O_2^-{}_{(ads)} \rightarrow 2CO_2 + 4H_2O + 3e^- \qquad (4.5)$$

This results in the creation of an accumulation layer forms at the SnS/SnS$_2$ interface, with holes accumulating on the SnS side and electrons on the SnS$_2$ side. Upon exposure to ethanol gas, the molecules preferentially adsorb at the interface of the SnS/SnS$_2$ nanocomposite sensor. This is due to the presence of multiple heterojunctions, which provide abundant active sites, including sulfur defects and vacancies, that facilitate enhanced gas adsorption. The surface area analysis using BET measurements confirms the enhanced number of adsorption sites on the SnS/SnS$_2$ nanocomposite. SEM and TEM analyses of the SnS/SnS$_2$ heterostructure reveal a defect-rich morphology with abundant active sites, enhancing gas adsorption and sensor sensitivity. Sulfur vacancies in SnS$_2$ further contribute to improved sensing performance by facilitating adsorption, while Raman spectroscopy provides indirect confirmation of these defects through shifts in peak intensity. The Sn$_2$S$_3$ phase in the nanocomposite enhances charge transfer, modulates electrical resistance, and provides additional gas adsorption sites, improving sensitivity and stability. Its intermediate bandgap facilitates heterojunction formation, optimizing sensor response and recovery [80, 81]. Thus, the overall concentration of majority charge carriers (holes) decreases, which widens the charge accumulation region and upsurges the sensor's resistance, thereby enhancing the performance. The accumulation region at the interface is a critical factor for high sensitivity. This overall improvement in sensing performance is attributed to charge transfer mediated by the Fermi level, which results from the variation in work function values. Because of the improved charge transport at the interfaces, there are more free electrons accessible, thereby providing better sensor performance. This, in turn, can significantly boost the adsorption of oxygen species [82]. Furthermore, heterostructure that contains materials which would allow a better adsorption rate of gasmolecules ethanol contributes to enhancing the performance of sensing. In summary, the two major factors enhancing the SnS/SnS$_2$ sensor's RT ethanol detection response are the elevated Fermi energy in the heterostructures, which favors efficient electron

transfer during the sensing process, and the larger surface area of the nanocomposite

sensor. This increased surface area provides abundant active sites for ethanol molecule adsorption, significantly boosting sensitivity.

4.6   Conclusions

To conclude, RT operating highly sensitive ethanol gas sensor was designed using SnS/SnS_2 p- n heterostructures with an accumulation layer. A comprehensive analysis of the surface morphology and nanostructure of the synthesized sample was conducted using TEM, SEM, XRD, and Raman spectroscopy, offering strong evidence for the successful synthesis. The pristine-SnS possesses a significant BET-specific surface area of 5.30 m²/g. In contrast, the SnS/SnS_2 nanocomposite features a particular surface area of 15.31 m²/g, providing more active sites and highly enhancing gas-sensing performance. The sensing response of the nanocomposite sensor toward 500 ppm ethanol gas is remarkable at 35.7, and also the improvements in the response time are 6.1 s and recovery time is 18.3 s. Not only do these artificial sensors demonstrate unprecedented stability with stable performance over an operating period of 40 days, but the excellent mechanism of performance is examined with adsorption/desorption isotherm analysis where impressive advances have been reported in reaction kinetics. RT sensing performances for ethanol are extremely superior, which is controlled by synergistic effects consisting of enhanced adsorption sites, increased electron transfer efficiency, and pronounced resistance modulated effects by SnS/SnS_2-based p-n heterostructures. We hope that this 2D heterointerface will lay the foundation for advancing the 2D nanostructure into a superior precision and efficient ethanol gas detector.

CHAPTER 5

Conclusions, Future Scope, and Social Impact
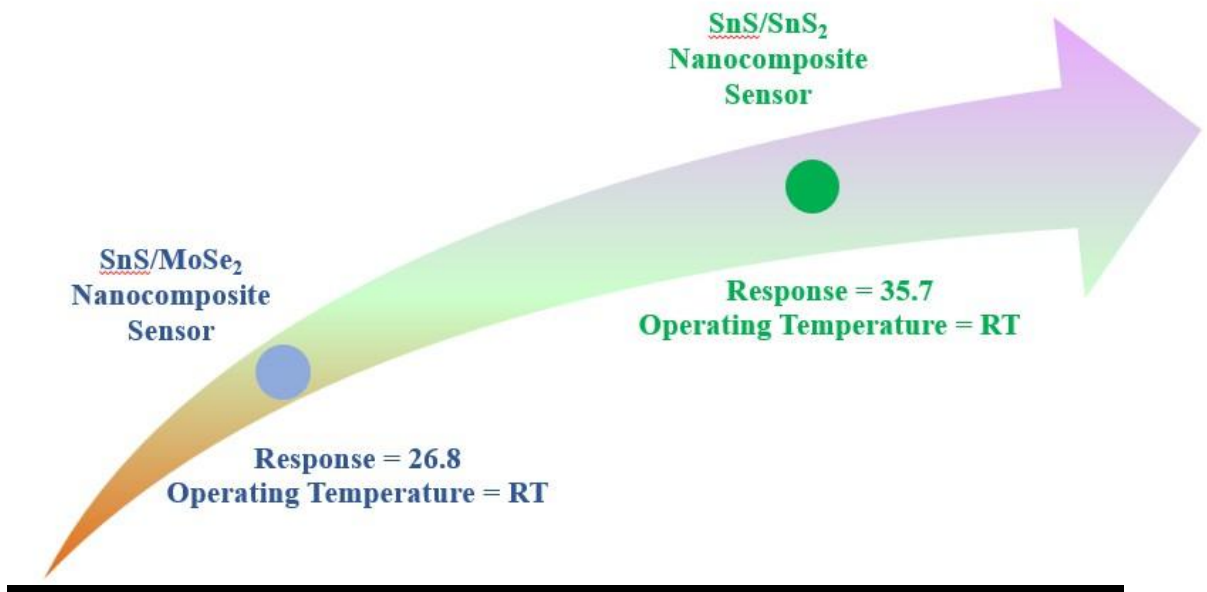
The main goal of this chapter is to summarize the major observations, experimental results, and conclusions derived from the current research study. It gives a short but inclusive overview of the results presented in every chapter, thus sketching the overall development and consistency of the study. In addition, this chapter points out future directions and potential research paths and prospects flowing from the present study, which provides the basis for further developments in the context of gas sensing and sensor design based on nanomaterials.

5.1   Summary of research work

In short, the current thesis leverages the distinctive physicochemical properties of 2D nanomaterials and their nanocomposites, utilizing them for the sensing of environmentally significant gases, focusing on ethanol sensing in particular. The general goal of the work was the design and fabrication of room-temperature (RT) gas sensors that are low-power-consuming, highly sensitive, and operatively stable. The scientific reason, synthesis techniques, and experimental approaches employed to realize these goals are examined in a systematic fashion in Chapters 1 to 4. This chapter constitutes a brief synopsis of the principal findings and research results that encapsulate the underlying reasoning, the methodological setup, and the principal experimental investigations undertaken over the duration of this work, as follows:

Chapter 1 gives an overall introduction to the escalating international interest in the development of ethanol gas sensors that can function effectively at room temperature (RT) with low power consumption. It starts by pointing out that there is an urgent need for sensors with high sensitivity, selectivity, and stability, especially under ambient conditions, to allow for reliable detection over a wide concentration range of ethanol. The chapter subsequently provides an overview of the current technologies for ethanol sensing with particular emphasis on chemiresistive sensors due to their versatility, scalability, and integration compatibility with electronic systems. In addition, it highlights the contribution of nanotechnology and materials engineering towards optimizing sensor performance parameters through structural, compositional, and morphological tailoring. Particular emphasis is placed on 2D nanomaterials and their nanocomposites, which provide synergistic benefits for the future generation of ethanol sensing. Based on this discussion, the chapter outlines principal research gaps and develops the aims of the current work, thus setting the solid conceptual and technical basis for the rest of the chapters.

Chapter 2 provides a detailed description of the experimental techniques followed for the synthesis, fabrication, and characterization of 2D nanomaterials and their nanocomposites. It discusses in detail the electrophoretic deposition (EPD) method used for the fabrication of uniform sensing films with controlled thickness and good adhesion to the substrate. A comprehensive overview of the techniques of

characterization is presented, such as X-ray diffraction (XRD) for structural and phase identification, field emission scanning electron microscopy (FESEM) and high-resolution transmission electron microscopy (HRTEM) for extensive morphological and microstructural exploration, and Raman spectroscopy for studying vibrational modes and crystallinity. In addition, the chapter explains the fabrication of chemiresistive gas sensors, where metal electrodes are deposited onto the sensing films synthesized through thermal evaporation. The gas sensing functionality of the fabricated devices is then tested using a specially designed chemiresistive gas sensing apparatus, allowing for accurate evaluation of their response behavior under well-defined environmental conditions.

Chapter 3 reports the synthesis and performance of an RT chemiresistive ethanol gas sensor using hydrothermally synthesized SnS-decorated $MoSe_2$ nanocomposites. The gas-sensing properties of the sensor were examined comprehensively by testing it in air-dry conditions for different concentrations of ethanol varying between 50 and 400 ppm. The synergistic coupling of SnS nanoplates and $MoSe_2$ nanosheets was discovered to have a large effect on the sensor's response toward ethanol, providing fast response and recovery times of 9.1 s and 15.7 s, respectively, as well as high selectivity, stability, and reproducibility. In addition, the device performed well for ethanol detection at concentrations as low as 50 ppm, with excellent operational reliability and long-term stability. In general, the $SnS/MoSe_2$ nanocomposite sensor performed better than a number of previously described systems, identifying it as a viable candidate for low-power, efficient room-temperature ethanol gas sensing.

Chapter 4 aims at further enhancing the RT ethanol gas sensing behavior by constructing a binary SnS/SnS_2 nanocomposite based on p-n heterojunctions. The chemiresistive sensor prepared was rigorously tested against ethanol concentrations between 10 and 500 ppm to determine its sensitivity, selectivity, as well as dynamic response behavior. The gas sensing performance showed that at 500 ppm ethanol, the sensor obtained a remarkably increased response value (R_g/R_a) of 35.7 with fast response and recovery times of 6.1 s and 18.3 s, respectively. In addition, the device showed high sensitivity to low concentrations of ethanol (down to 10 ppm) and showed very good operating stability for 40 days under dry air. These results highlight the

crucial role of a series of p-n heterojunctions and effective charge transfer channels in improving the gas sensing performance, thus making the SnS/SnS$_2$ nanocomposite sensor a strongly promising candidate for real-time, reliable, and room-temperature ethanol gas detection.

5.2   Salient outcomes of the thesis

Main findings and contributions of this thesis are as follows:

➢ A p-p heterojunction-based sensor was successfully prepared by employing hydrothermally synthesized SnS nanoplates dispersed with MoSe$_2$ nanosheets. Synergistic interaction between the two p-type materials provided improved sensitivity, fast response/recovery behavior, and good stability at ambient conditions.

➢ A p-n heterojunction-based SnS/SnS$_2$ nanocomposite was synthesized, which showed excellent ethanol sensing properties in terms of high response values, ultra-fast response/recovery times, and good long-term stability. The creation of multiple p-n junctions and effective charge transfer pathways played an important role in the enhanced sensing properties.

5.3   Future prospective

The current thesis delves into the novel physicochemical properties and functional merits of 2D nanomaterials and their heterostructure-based nanocomposites for detecting environmental hazards, focusing especially on chemiresistive gas sensing. By methodically examining their synthesis, structural features, and sensing properties, this research lays a solid cornerstone for future sensing technologies. The findings obtained from this work unlock numerous promising prospects for further investigation and technological advancement, such as:

1. **Scaling up monolayer synthesis:** Monolayers of 2D nanomaterials have unique physicochemical, electronic, and optical characteristics that are quite different from those of their bulk counterparts. Achieving device-scale miniaturization and large-scale integration of monolayer-based sensors requires the reproducible and

controlled synthesis of these materials on an industrial scale. The creation of high-yield, defect-reduced, and thickness-uniform synthesis methods—like chemical vapor deposition (CVD), atomic layer deposition (ALD), or liquid-phase exfoliation—is thus essential to unlocking the complete potential of 2D nanomaterials in commercial and scalable gas sensing. Ongoing improvements in scalable synthesis technologies will be instrumental in overcoming the divide between laboratory-scale work and real-world application of these materials.

2. **Improving Metal Chalcogenides Using Material Engineering:** Metal chalcogenide performance can be significantly enhanced with strategic modification and hybridization strategies, including the inclusion of metal oxides, conductive polymers, or other functional nanomaterials. Synergistically enhancing charge transport, surface reactivity, and interfacial stability is facilitated in these hybrid architectures, which are key to optimizing sensor response properties. Optimization of the electronic structure, defect concentration, and surface chemistry of metal chalcogenides via tunable compositional design can further enhance their sensitivity, selectivity, and operating stability. These improvements are especially promising for enabling self-powered and low-power gas sensors, which can sustainably operate under ambient conditions.

3. **Investigating Emerging 2D Nanomaterials:** Exploring novel 2D nanomaterials on the horizon, including MXenes (e.g., Ti_3C_2Tx), borophene, and other new layered systems, offers great promise for the development of self-powered gas sensing technologies. These materials have superior electrical conductivity, surface terminations that are adjustable, and high chemical reactivity, which can be leveraged to optimize gas adsorption dynamics, charge transfer efficiency, and overall sensing performance. Combining such materials with hybrid and heterostructured sensor architectures may produce devices that are more sensitive, selective, and capable of multi-gas detection. Further investigation into stabilization techniques and interface engineering will be needed to tap into their full potential for high-performance, energy-efficient, and next-generation gas sensing.

4. **Developing Flexible and Wearable Sensors:** The evolution of flexible gas sensors is a milestone towards real-time, wearable, and portable electronic devices. These sensors can be very easily integrated into textiles, accessories, or flexible substrates for continuous, non-invasive measurement of environmental and physiological parameters. Use of mechanically resilient, bendable, and conformable nanocomposite materials ensures the durability of the device without sacrificing sensing performance. Further developments in this direction may translate into next-generation wearable devices that can offer real-time health diagnosis, fitness tracking, and personal safety notifications. Additionally, embedding these flexible platforms with wireless communication modules and energy-harvesting systems will further increase their autonomy and usefulness in smart healthcare and environmental monitoring.

5. **Advancing Lab-on-Chip Devices:** The development of Lab-on-Chip (LoC) technologies is a key direction to integrate gas sensing, diagnostics, and analytical functions onto small-scale, multifunctional platforms. Innovation in micro/nanofabrication methods, materials integration, and scalable manufacturing processes will be critical to improve the efficiency, reproducibility, and cost competitiveness of these systems. The large-scale deployment and commercialization of LoC devices with success can transform applications in environmental monitoring, personalized medicine, and point-of-care diagnostics into rapid, real-time, and accurate analytical capabilities. Further advancement in device miniaturization, microfluidic design, and sensor-signal coupling will continue to increase the scope and availability of LoC-based sensing technologies to research and industry applications.

The suggested research is focused on the synthesis of an ultrahighly sensitive, selective, and stable nanostructured sensing component for ethanol gas detection at room temperature (RT). With the help of advanced nanomaterials, heterostructure engineering, and novel fabrication techniques, this research seeks to substantially improve the efficiency, reliability, and reproducibility of chemiresistive gas sensors. The results of this work are anticipated to be of significant value to environmental monitoring, industrial safety systems, and process control, where accurate and sensitive

ethanol detection is imperative. In addition, the achievements made through this research form a solid basis for future low-power, miniature, and autonomous sensing platform development compatible with next-generation smart sensor networks and IoT-based technologies.

The fabricated ethanol gas sensors at room temperature contribute to meaningful social benefits, offering ways for safer and healthier environments. Their high sensitivity and real-time detection capability could prevent industrial accidents and exposure to injurious vapors, supporting air quality monitoring in public and residential areas. With low power consumption and cost-effective fabrication, the sensors are perfectly positioned for wide deployment and sustainable technologies that will enhance community health, workplace safety, and overall environmental well-being.